Università degli Studi di Milano

Facoltà di Scienze e Tecnologie

Dipartimento di Chimica

Scuola di Dottorato in Chimica

XXX Ciclo

Quantum and Semiclassical Methods for Rate Constant Calculations

Advisor:
Prof. Michele Ceotto

Ph.D. Candidate:

Chiara Donatella Aieta

Id. N. R10875

Academic year 2016/2017

Referees:

Prof. Gunnar Nyman, Department of Chemistry & Molecular Biology, Göteborgs Universitet, Göteborg, Sweden.

Prof. Fabio Finocchi, INSP, Université Pierre et Marie Curie - Paris 6, Paris, France.

Examination Board:

Prof. Elena Selli, Dipartimento di Chimica, Università degli Studi di Milano, Milano, Italy.

Dr. Habil. Frank Grossman, Institut für Theoretische Physik, Technische Universität Dresden, Dresden, Germany.

Prof. Guido Raos, Dipartimento di Chimica, Materiali e Ingengeria Chimica "Giulio Natta", Politecnico di Milano, Italy.

Final exam:

Date: February, 2nd 2018.

Università degli Studi di Milano, Dipartimento di Chimica, Milano, Italy.

Contents

[1]This chapter is the reproduction with some minor changes of the paper **Chiara Aieta**, Fabio Gabas, and Michele Ceotto, "An Efficient Computational Approach for the Calculation of the Vibrational Density of States" *J. Phys. Chem. A* **120**, 4853 (2016).

[2]This chapter is the reproduction with some minor changes of the paper **Chiara Aieta**, and Michele Ceotto, "A Quantum Method for Thermal Rate Constant Calculations From Stationary Phase Approximation of the Thermal Flux-flux Correlation Function Integral" *J. Chem. Phys.* **146**, 21411 (2017).

1 Introduction

The most astonishing property of chemical species is their ability to react. From a macroscopic point of view, a chemical reaction is the change of the properties of the system in time.[1]

To characterize this phenomenon, a first observable that can be investigated is the velocity with which this change takes place. Taking into account a general reaction

$$\mathrm{aA+bB\rightarrow cC+dD} \tag{1.1}$$

the velocity of the process that changes reactants into products can be macroscopically described as the ratio R of the instantaneous concentration of one of the species with the infinitesimal amount of time in which this change takes place.

$$R = -\frac{1}{a}\frac{d\left[A\right]}{dt} = -\frac{1}{b}\frac{d\left[B\right]}{dt} = \frac{1}{c}\frac{d\left[C\right]}{dt} = \frac{1}{d}\frac{d\left[D\right]}{dt} \tag{1.2}$$

Another important observation is that the velocity of the process depends on the concentration of the reactants, because it is assumed that only the reactants are present when the reaction starts. This means that the rate R can be expressed as a function of the concentration of the reactants. The most usual functional dependence is a product of algebraic powers of the concentration of the reactants

$$R = k\left[A\right]^{m}\left[B\right]^{n} \tag{1.3}$$

where m and n have to be determined experimentally and do not necessarily correspond to the stoichiometric coefficients.[1] k is the thermal rate constant (or rate coefficient) of the reaction. It is a function of the temperature.

However, Eyring pointed out in his 1936 review about the state of the art of rate theory, that "since the first measurement of reaction rates by Wilhelmy in 1850, chemists have been struggling with the question of mechanism".[2] In fact, the macroscopic approach to the quantitative understanding of reaction kinetics does not provide any information about the molecular mechanism. This is evident from textbook examples about the oxidation reaction of NO.[3] Its

stoichiometric equation is

$$NO + O_2 \xrightarrow{k} 2NO_2 \tag{1.4}$$

The expression of the rate based on the stoichiometry of reaction 1.4 should be written as R = k [NO] [O_2] which is known not to agree with experimental data. For this reason, a more complex underlying reaction mechanism must be proposed. A possible two-step mechanism for this reaction consists in a preliminary equilibrium reaction followed by a fast reaction with oxygen, as represented in the following scheme

$$\begin{aligned} 2NO &\overset{K_{eq}}{\rightleftarrows} N_2O_2 \\ N_2O_2 + O_2 &\xrightarrow{k_1} 2NO_2 \end{aligned} \tag{1.5}$$

where K_{eq} is the thermodynamics equilibrium constant. The reaction rate is determined by the slowest step, also called the rate determining step. In this case, R = k_1 [N_2O_2] [O_2] = k_1 K_{eq}[NO]^2[O_2] = k_{tot}[NO]^2[O_2]. Surprisingly, the same kinetic law can be obtained if the following, completely different reaction scheme, is assumed

$$\begin{aligned} NO + O_2 &\overset{K'_{eq}}{\rightleftarrows} NO_3 \\ NO_3 + NO &\xrightarrow{k_2} 2NO_2 \end{aligned} \tag{1.6}$$

In fact, even in this case, taking into account that the second equation in scheme 1.6 is the fast process, the rate is R = k_2 [NO_3] [NO] = k_2 K'_{eq}[NO]^2[O_2] = k_{tot}[NO]^2[O_2]. This makes clear that a macroscopic kinetic picture based on the stoichiometry of a reaction can be misleading and, in general, does not provide any certain information about the reaction mechanism.

In conclusion, this level of understanding is somehow unsatisfactory. It would be much more interesting to explain and understand chemical reactions at a molecular level or, in other words, by taking explicitly into account the microscopic structure of molecules as composed by nuclei and electrons that interact with each others. This is the subject of reaction dynamics which is the broad research field of this thesis.

Chemical reactions are intrinsically dynamical processes. This can be appreciated in the framework of the Born Oppenheimer (BO) approximation. When a potential energy surface (PES) is associated to a reaction, two regions can be identified on it. The first one corresponds to the reactants, and it can be separated by means of a dividing surface (DS, a function of the coordinates of the system) from another region corresponding to the products of the reaction.

In the BO framework, a chemical reaction can be thought as a three-step process that involves the motion of the nuclei. First the reactants approach each other, then a rearrangement occurs, and finally the products separate. This nuclear rearrangement is governed by forces that are proportional to the slope of the PES. The vague concept of reaction mechanism is therefore reduced to the precise concept of dynamics of the nuclei on the BO potential energy surface. Rate constant estimates are very dependent on the PES accuracy, so a major computational effort for kinetics simulations is represented by the need to employ a high level of electronic theory for the PES.

The dynamical reaction process can be precisely described from a quantum mechanical point of view. A well-defined internal state of the reactants can be described by means of a wavepacket that can also be quantum mechanically evolved forward in time. At some point, the wavepacket enters the interaction region of the potential and splits into two parts. A first part bounces back and returns to reactants, while the other one proceeds to the products. Projection of the product wavepacket onto the asymptotic eigenstates of products gives the transition probabilities from the initial state to all final states. If this is repeated for different initial states, the probabilities of all possible transitions from all initial states to all final state are known. By averaging out the sum of these probabilities over the Boltzmann distribution at the chosen temperature, the reaction rate constant is finally obtained.[4] From this picture it is evident that reaction rate constants, and thus the understanding of chemical kinetics, can be in principle obtained at a very detailed level if one is able to compute the real time quantum dynamics for the reactive system. Unfortunately, the numerical implementation of real time quantum dynamics is very hard to perform, especially for high dimensional systems, because the computational effort scales exponentially with the number of degrees of freedom.

One possibility to overcome this limitation is to approximate the quantum mechanical dynamics with its classical counterpart which has the advantage to scale linearly with the number of degrees of freedom of the system. In classical mechanics, it is possible to start a group of trajectories by selecting nuclear configurations in the reactant region of the potential and associating initial momenta to the nuclei through a fixed-temperature Maxwell-Boltzman distribution of atomic velocities. The trajectories are evolved in time by solving the classical equations of motion. After a suitable (hypothetically infinite) evolution time, some of these trajectories will be found in the product region of the potential, while others remain in the reactant region. Then, the reaction rate constant at the chosen temperature can be intuitively defined as the average flux of trajectories that cross the DS and that end up in the product region.[5] In this way, all quantum

effects are not accounted for. However, some quantum effects play a key role and should not be overlooked. A visual representation of the classical mechanics as well as the quantum mechanics approach to reaction dynamics is depicted in figure 1.1, for the F + DBr reaction. A more sophisticated approach, called quasi-classical trajectory (QCT) dynamics,[8, 9] even if still based on a fully classical dynamics, allows to quantize the initial distribution of reactants and can be employed to study the effects of mode-specific excitation on the reaction. An even more refined approximation to quantum dynamics is represented by semiclassical methods, which are still based on classically-evolved trajectories but employ a mathematical formalism (derived from Feynman's representation of quantum mechanics) able to regain quantum effects like energy level quantization, coherences, tunneling and over-barrier reflection.[10, 11, 12, 13, 14, 15, 16, 17, 18, 19, 20, 21, 22, 23, 24, 25, 26, 27, 28, 29, 30, 31, 32]

An alternative way to avoid the issues connected with the quantum dynamics lies on the drastic approximation to get rid of the real time evolution to develop an approximate rate theory based only on thermodynamics (imaginary time) information. This is the founding of Transition State Theory (TST), that was first developed during the thirties mainly by Arrhenius, Eyring, Polanyi and Wigner.[33, 34, 35, 2] This theory has the advantage that the rate constant is computed only from the local geometrical features of the PES. The needed parameters are in fact the curvature of the potential energy surface at the saddle point (which corresponds to the transition state) and in the reactant well, plus the height of the barrier separating reactants and products. Thus, construction of the full PES is not necessary. The disadvantages of a TST approach are first that, by neglecting all dynamical information, TST does not take into account the possibility of recrossing, which is a purely dynamical phenomenon. Secondly, some quantum effects like tunneling are ignored. Furthermore, there are instances where it is not realistic to consider that reactivity is governed only by the narrow passage about the saddle point. This happens for example in the case of significant corner cutting effects, barrier-less reactions or, as recently discovered, roaming dynamics.[36, 37] Anyway, a key advantage of neglecting real time dynamics is that the typical sign problem of Feynman path integration is avoided and path integration techniques become computationally affordable.

In this thesis two open problems in reaction rate theory have been addressed. The first one is to extend to high dimensional systems the inclusion of quantum effects in rate constant computations. The second issue faced concerns the inclusion of real time dynamics into very accurate rate constants calculations.

The thesis is organized as follows. The second chapter is an overview of the state of the art in reaction rate theory. Then, in chapter 3, the derivation of

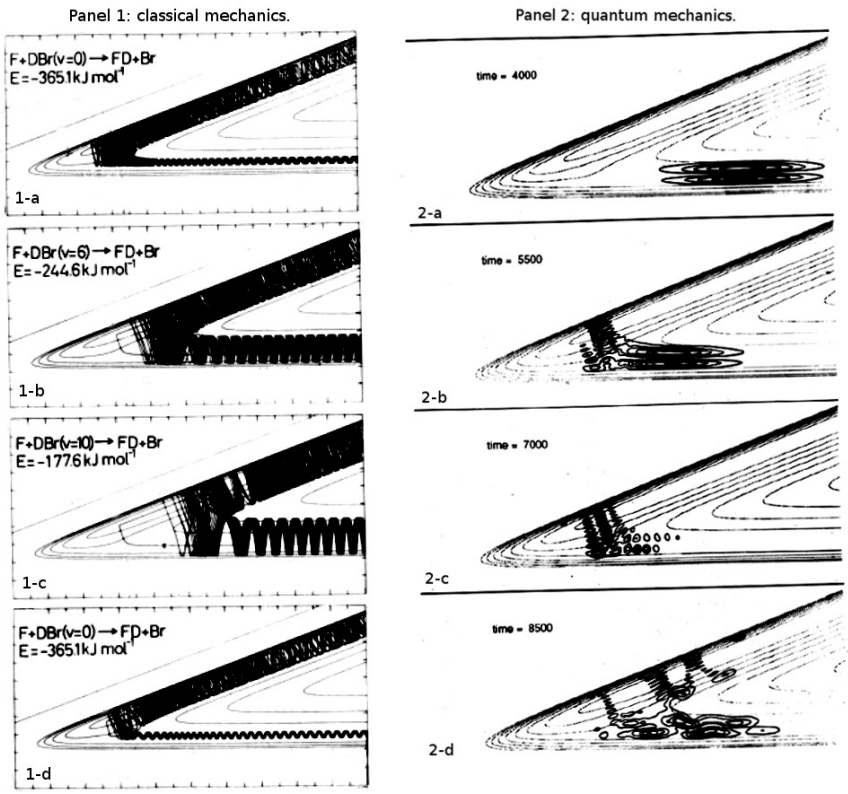

Figure 1.1: F + DBr reaction dynamics calculations from the point of view of classical mechanics (panel 1, adapted from reference [6]), and quantum mechanics (panel 2, adapted from reference [7]). The two panels should not be compared frame by frame. In panel 1, classical trajectory computations are presented for several different energies and reactant angular momenta. They show for this reaction a significant corner cutting (1-a, 1-b, 1-c, and 1-d). Panel 2, instead, shows the more complex phenomenology of quantum mechanics at a fixed energy. The initial wavepacket (2-a) is prepared with an energy higher than the barrier and propagated forward in time. When it hits the barrier, quantum mechanical reflection is observed (2-b). Then, while products are starting to appear, the reflected part of the wavefunction interferes with its counterpart that tries to overcome the barrier (2-c). Finally the reactive and nonreactive branches appear and the wavefunction cuts the corner (2-d).

Miller's Semiclassical Transition State Theory (SCTST)[38, 39] is recalled. SCTST is the method employed to obtain accurate and quantum-corrected rate constants for high dimensional reactions. In chapter 4, a novel parallel implementation of this theory that has also been released as an open source code in the MultiWell program suite of J. R. Barker et al.[40, 41] is described together with its ongoing application to high dimensional systems. In the following chapters, a new quantum rate approach able to include real time dynamics effect is presented. Derivation and applications of the latter are thoroughly described in chapter 6. The thesis ends with some perspectives about possible future developments.

2 Reaction Rate Theory

To explain the foundations of microscopic reaction rate theory of chemical processes, it is better to discuss it first in the context of classical mechanics and then use the derivation as a guide to find its quantum mechanical analogue. A computationally-efficient classical strategy would consist in starting the trajectories from the interaction region of the PES and then follow the dynamics forward and backward just for the amount of time that is necessary for understanding if the trajectory is a reactive one. This requires just a short time dynamics that is much cheaper than evolving trajectories for a long time starting from the reactant region.[42] The idea is exploited in the flux correlation function formalism which permits to obtain the rate from a short time dynamics, and, eventually, the approach can also be extended to a quantum-mechanical framework.

2.1 Rate Constants in Classical Mechanics

A chemical reaction is a transition between two stable states, represented by two minima on the PES, as illustrated in figure 2.1. The reactant state is called A, while B is the product state and they are separated by a barrier in potential energy. To describe the progress of the reaction, a reaction coordinate q, a dynamical variable able to distinguish if the system is in the reactant state A or the product state B, is defined as a suitable function of the coordinates of the system. For instance, q can be chosen such that it is null at the barrier top ($q^* = 0$). In this way, it changes sign when passing from the reactant to the product state. The barrier height is the activation energy V*, which is the difference between the potential at the barrier top and the potential of the reactants. The barrier is considered to be "high" when $V^* \gg k_B T$, where k_B is the Boltzmann constant and T is the temperature. This means that the average thermal energy of the system is very small compared to the height of the barrier. As a consequence, it is very unlikely that the system is able to overcome the barrier. In fact, to cross it the total energy should be distributed among all the degrees of freedom in a way that the amount of energy in the reaction coordinate is very large compared to $k_B T$. Therefore, the barrier acts as a dynamical bottleneck, and the occurrence of the reaction is a rare event.

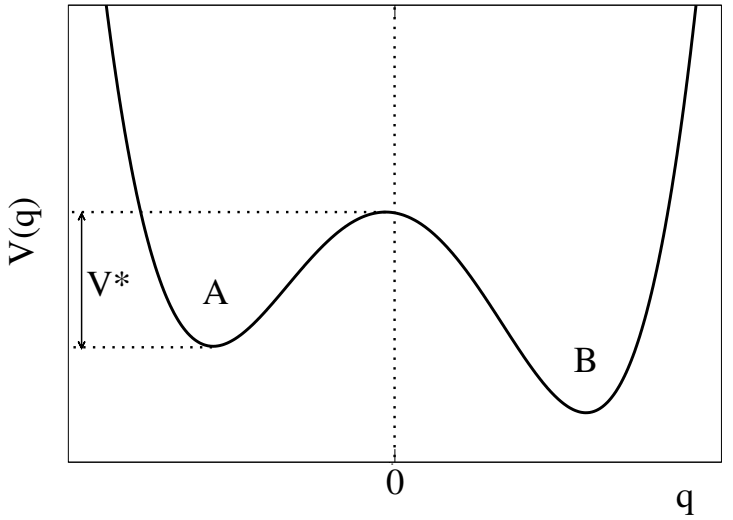

Figure 2.1: One dimensional cut of the PES associated to the generic reaction A⇄B. q is a generic reaction coordinate, V* is the activation energy for the forward reaction.

A direct way to study the reaction process is to set a trajectory that starts from the reactant well and to evolve it for a total time τ. To keep track of the reaction coordinate values a histogram can be recorded. This histogram defines the probability distribution for the reaction coordinate and it is formally defined as

$$P(q) = \frac{1}{\tau}\int_0^\tau dt\delta\left[q(t) - q\right] \tag{2.1}$$

Since the passage over the barrier is a rare event, the histogram has very high peaks around the values of the reaction coordinate that characterize the stable states A and B, while the probability associated to the value q = q* = 0 will be negligible. This fact points out that to collect a significant statistics of the reactive event, an extremely long evolution time τ is needed. In fact, if n is the number of reaction events that has to be observed, t_{cross} the time that it takes to pass over the barrier, and $e^{-\beta V^*}$ is the probability to visit the barrier at a certain temperature, the time scale $\widetilde{\tau}$ of the dynamics for a typical chemical reaction at room temperature can be estimated (β=1052 at 300K; barrier height 0.03809 a.u.) as

$$\widetilde{\tau} = nt_{cross}e^{\beta V*} = n \times 10^{-13}s \times 10^{17} = n \times 10^4 s \tag{2.2}$$

that is a huge duration for an atomistic simulation. As a result, it is impractical to obtain quantitative information about the reaction processes via a brute force

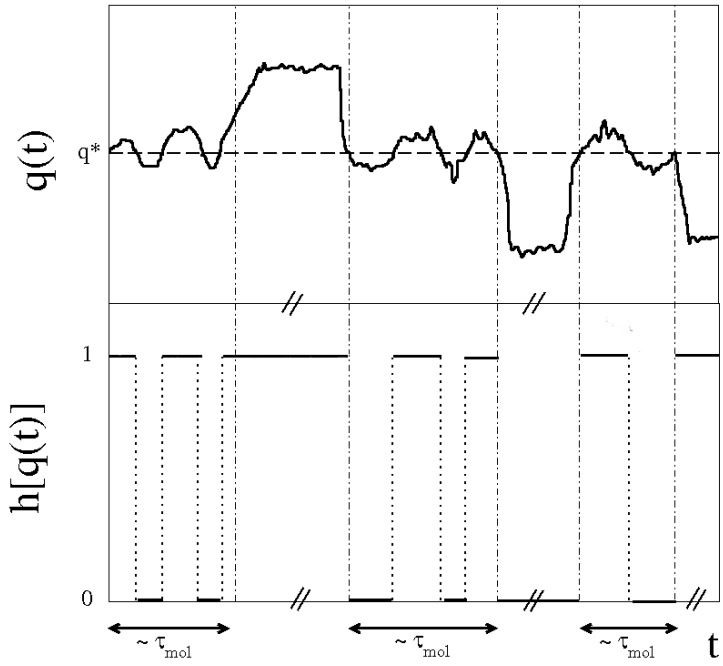

Figure 2.2: In the upper panel the value of the reaction coordinate along the trajectory is depicted, while, in the lower panel, the correspondent product population function is reported. The double slash represents the interruption of the time axes.

trajectory simulation. However, this dynamical point of view is still useful to get to a definition of rate constant from microscopic information.

For this purpose, the dynamics of a trajectory initiated at the barrier top can provide some important insights. To start off, the product population function is defined as

$$h\left[q\left(t\right)\right] = \begin{cases} 0 & q\left(t\right) < 0 \\ 1 & q\left(t\right) > 0 \end{cases} \tag{2.3}$$

If it were possible to perform a simulation with a total time longer than $\tilde{\tau}$, the graph of this function would appear as represented in figure 2.2. In the upper panel it is shown that the system remains for a certain time in the vicinity of the barrier top. During this period, which is about the time scale of molecular rearrangements τ_{mol}, the trajectory generally crosses the transition state more than once. This phenomenon is called recrossing. For t > τ_{mol} the trajectory instead is trapped in one of the two stable states until enough energy is accumulated again

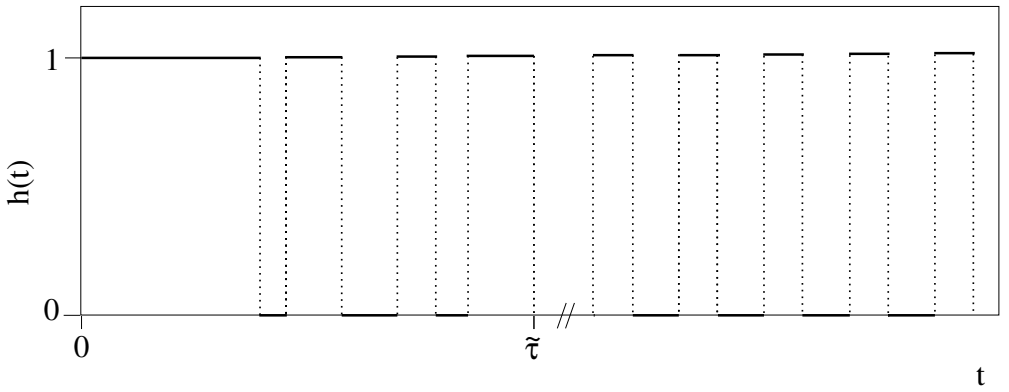

Figure 2.3: The product population function.

in the reaction coordinate and a new barrier crossing is observed. As already discussed, this time is very long. Therefore, in reporting the graph of the product population function on a much larger time scale, its behavior on the τ_{mol} interval is no longer distinguishable, as represented in figure 2.3. On this longer time scale, two regimes are observed. First the system is in one of the two stable states, for example A and in a time $\tilde{\tau}$ it undergoes irregular rare jumps from one state to the other. Then, after a very long time, the reaction reaches thermodynamical equilibrium and remains there forever. At equilibrium the shape of the $\mathrm{h}[q(t)]$ function becomes periodic. The average time spent in the state B is defined as

$$\langle h \rangle = \frac{1}{\tau} \int_0^{\tau} h\left[q\left(t\right)\right] dt \tag{2.4}$$

this average is independent of time and it is dominated by the behavior of the system at equilibrium. Moreover, the distance from the equilibrium can be quantified at any instant with the instantaneous fluctuation of the population

$$\delta h\left[q\left(t\right)\right] = h\left[q\left(t\right)\right] - \langle h \rangle \tag{2.5}$$

The correlation of the instantaneous fluctuation of the population with the population at an earlier time is

$$\langle h \delta h\left[q\left(t\right)\right] \rangle = \frac{1}{\tau} \int_0^{\tau} dt' h\left[q\left(t'\right)\right] \delta h\left[q\left(t'+t\right)\right] \tag{2.6}$$

This integral can be solved by considering that the only fractions of time x which give a non zero contribution to it are those in which the system is found in state

B, that is

$$\langle h\delta h\left[q\left(t\right)\right]\rangle = x\overline{\delta h}\left[q\left(t\right)\right] \tag{2.7}$$

The limit of $\overline{\delta h}\left[q\left(t\right)\right]$ as time goes to infinite is null, since the system relaxes to equilibrium. This average therefore measures the relaxation of the system toward equilibrium, i.e it quantifies the probability of observing a reactive event in a period of time t after a first reactive event was observed a t = 0.

On the longer time scale, the transitions from the state A to the state B are very infrequent, then it is reasonable to consider the reactive events as uncorrelated. The probability of observing N transitions over a time period t is described by a Poisson distribution, with ν as the average frequency of barrier crossing

$$P\left(N\right) = \frac{1}{N!}\left(\nu t\right)^{N} e^{-\nu t} \tag{2.8}$$

Therefore, the probability to observe a reactive event between t and t + dt decreases exponentially with the time of observation t, that can be expressed as

$$\overline{\delta h}\left[q\left(t\right)\right] \sim \overline{\delta h}\left[q\left(0\right)\right] e^{-kt} \tag{2.9}$$

Another way to derive the same result of equation 2.9, is to start from macroscopic rate equations that describe the equilibrium reaction A⇆B and apply the fluctuation dissipation theorem expressed in the form of Onsager regression hypothesis to link the macroscopic rate constant to microscopic mechanical behavior of the system.[43] This approach is described in Appendix 2.7.

At this stage it is defined the time dependent quantity k(t) as

$$k\left(t\right) \equiv -\frac{d}{dt}\frac{\overline{\delta h}\left[q\left(t\right)\right]}{\overline{\delta h}\left[q\left(0\right)\right]} = -\frac{d}{dt}C\left(t\right) \sim ke^{-kt} \tag{2.10}$$

where the long time limit is deduced from equation 2.9.

The function k(t) is schematically represented in picture 2.4. After a transient time of the order of τ_{mol} in which the function undergoes an irregular decay due to the recrossing events from the starting value k(0^{+}), a time range in which the exponential decay is observed begins. On the very short time scale of the molecular rearrangements the beginning of the exponential decay appears as a constant (ke^{-kt} ∼k+O(t)). Therefore, the function k(t) apparently reaches a plateau value k*, which is defined as the reaction rate constant. However, if there was no recrossing dynamics, k(t) would assume the constant value k(0^{+}) over the first τ_{mol} period, and therefore k* = k(0^{+}). This value for the rate constant is the one predicted by the Transition State Theory approximation (TST), that is

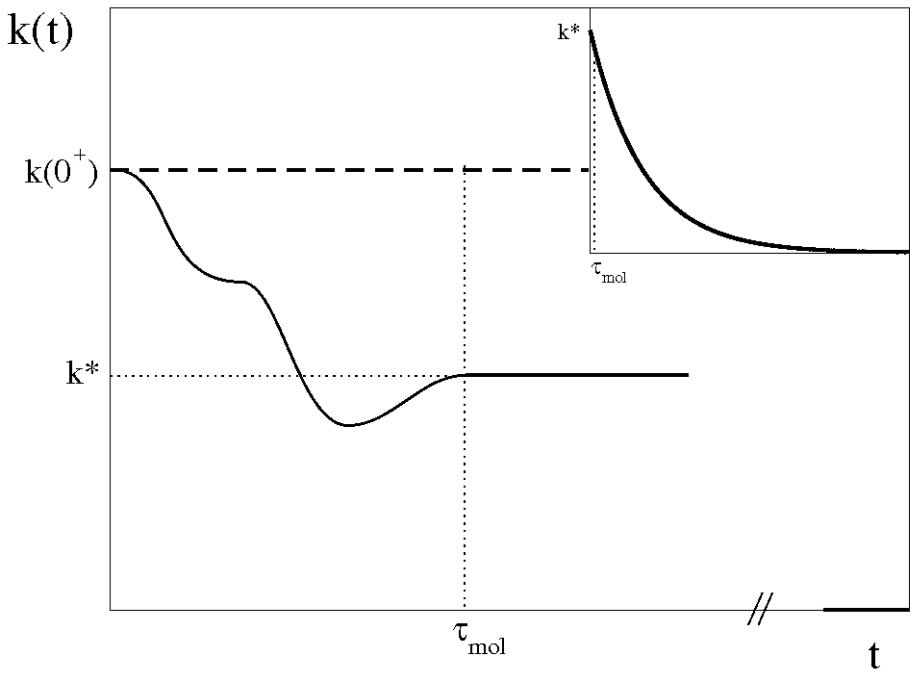

Figure 2.4: The inset shows the graph of the function k(t) over a large timescale. The exponential decay is observed. The function tends to zero when the system arrives at equilibrium. The bigger graph is an enlargement of the very first portion of the inset. At this shorter timescale ($\sim\tau_{mol}$) the irregular decay due to recrossing dynamics is observed, followed by a plateau that is the beginning of the exponential decay which appears as a constant on this time scale.

based on the assumption of no recrossing phenomena, in other words the direct dynamics approximation. k(0^+) is only an upper bound to the value of the rate constant, because the grater the recrossing, the lower the value of k*. The ratio Γ = k* / k(0^+) expresses how much the trajectory is stabilized to the state to which it points initially, and it is defined as the transmission coefficient. k(0^+), that is also the TST rate constant, is a statistical quantity that can be computed from thermodynamics information alone and it is independent of dynamics. On the contrary, Γ can be computed only by explicitly taking into account the dynamics on the fast time scale τ_{mol}.

By evaluating the derivative in the definition 2.10

$$k(t) = \frac{\langle \dot{q}\delta(q - q*)\, h[q(t)]\rangle}{\langle h\delta h[q(0)]\rangle} \tag{2.11}$$

it is revealed that $k(t)$ is the reactive flux correlation function.[44, 45, 46]

2.2 The Classical Flux-flux Correlation Function

From now on all the time averages that were introduced in the previous paragraph are considered as ensemble averages. The classical dynamics behavior of a molecular system composed by N atoms is described by the classical Hamiltonian $\mathcal{H}(\boldsymbol{p}, \boldsymbol{q})$. The generalized coordinates vector **p** and the generalized momentum vector **q** are n-dimensional, where n = 3N - 6 (or n = 3N - 5 in case of a linear molecule). Since the system is treated under the BO approximation, the potential part in the classical Hamiltonian is the PES associated to the molecular system.

To begin with, it is necessary to define a dividing surface, a function of the coordinates **q** of the system, as

$$f(\boldsymbol{q}) = 0 \tag{2.12}$$

This equation divides the coordinate space into two regions, one corresponds to the products and the other to the reactants. The reactant side is defined as $f(\boldsymbol{q}) < 0$, while $f(\boldsymbol{q}) > 0$ indicates the product side.

The rate constant 2.11 is rewritten as the ratio of two quantities

$$k_{CL}(T) = \frac{(2\pi\hbar)^{-n} \int d\boldsymbol{p_1} \int d\boldsymbol{q_1} e^{-\beta\mathcal{H}(p_1,q_1)} F(\boldsymbol{p_1}, \boldsymbol{q_1})\, P_r(\boldsymbol{p_1}, \boldsymbol{q_1})}{Q_r(T)} \tag{2.13}$$

The denominator of definition 2.13 is the total number of trajectories that are started with initial conditions compatible with the temperature of the system,

which is simply the partition function of the reactants

$$Q_r(T) = \int d\boldsymbol{p_1} d\boldsymbol{q_1} e^{-\beta \mathcal{H}(p_1, q_1)} \tag{2.14}$$

The numerator of expression 2.13 is the number of trajectories that cross the dividing surface and end in the product part of the PES in the infinite future. Here, $\mathbf{p}_1$ and $\mathbf{q_1}$ are the initial conditions for the trajectories.

Two key quantities appear, the flux factor $F(\boldsymbol{p_1}, \boldsymbol{q_1})$ and the projector term $P_r(\boldsymbol{p_1}, \boldsymbol{q_1})$. The former is defined as the rate of trajectories that cross the dividing surface and it is expressed as

$$F(\boldsymbol{p}, \boldsymbol{q}) = \frac{d}{dt} h(f(\boldsymbol{q})) = \delta(f(\boldsymbol{q})) \frac{\partial f}{\partial q} \dot{\boldsymbol{q}}(t) = \delta(f(\boldsymbol{q})) \frac{\partial f}{\partial \boldsymbol{q}} \frac{\boldsymbol{p}}{m} \tag{2.15}$$

Since the Heaviside function in the previous equation can assume only two values

$$h(\xi) = \begin{cases} 1 & \xi > 0 \\ 0 & \xi < 0 \end{cases} \tag{2.16}$$

the physical interpretation of $h(f(\boldsymbol{q}))$ is the probability that the $\mathbf{q}$ coordinate is in the product side with respect to the dividing surface. The projector term $P_r(\boldsymbol{p_1}, \boldsymbol{q_1})$, instead, is equal to one if the trajectory with initial conditions $\mathbf{p}_1$ and $\mathbf{q}_1$ goes to the product side in the infinite future, while it is zero in the opposite case. The projector term contains all the dynamics information. Following its definition it can be written as

$$P_r(\boldsymbol{p_1}, \boldsymbol{q_1}) = \lim_{t \to \infty} h\{f[\boldsymbol{q}(t; \boldsymbol{p_1}, \boldsymbol{q_1})]\} \tag{2.17}$$

where the notation underlines that in this classical mechanics approach the evolution of the coordinate in time is deterministic, i.e. it depends parametrically on the initial conditions of the trajectories. The physical meaning of $P_r(\boldsymbol{p_1}, \boldsymbol{q_1})$ is the probability that a trajectory initiated with certain initial conditions ends in the product region in the infinite future.

To compute the classical rate constant with equation 2.13 it is necessary to evolve the trajectories for a very long time, because the projector operator involves an infinite time limit.

The rate expression can be revised so that it is possible to stop the dynamics at a finite time. Using equation 2.15, it is readily shown that the projector term 2.17 is given by the time integral of the flux function evolved along the selected

trajectory

$$\begin{aligned} P_r &= \int_0^\infty dt \frac{d}{dt} h\left[f\left(\boldsymbol{q}\left(t\right)\right)\right] \\ &= \int_0^\infty dt \delta\left(f\left(\boldsymbol{q}\right)\right) \frac{\partial f}{\partial \boldsymbol{q}} \dot{\boldsymbol{q}}\left(t\right) \\ &= \int_0^\infty dt F\left(\boldsymbol{p}\left(t\right), \boldsymbol{q}\left(t\right)\right) \end{aligned} \tag{2.18}$$

Substituting this equation 2.18 in the expression 2.13 a new form of the classical rate constant

$$k_{CL}\left(T\right) = Q_r\left(T\right)^{-1} \int_0^\infty dt C_f\left(t\right)$$

where the flux-flux correlation function appears[5]

$$C_f\left(t\right) = \left(2\pi\hbar\right)^{-n} \int d\boldsymbol{p_1} \int d\boldsymbol{q_1} e^{-\beta \mathcal{H}(p_1, q_1)} F\left(\boldsymbol{p_1}, \boldsymbol{q_1}\right) F\left(\boldsymbol{p}\left(t\right), \boldsymbol{q}\left(t\right)\right) \tag{2.19}$$

2.3 Classical Transition State Theory

A well known approximate approach for the rate constant evaluation is the Transition State Theory (TST). As explained at the end of section 2.1, TST is a zero-time classical approximation that relies on the direct dynamics approximation,[35, 47] where any re-crossings across the DS is neglected. Thus TST provides an upper bound to the exact classical rate constant,[48] and ignores any quantum effects, such as tunneling and corner cutting.

The TST limit of the rate constant expressed as 2.13 is easily derived. To start off, it is convenient to make a coordinate change. The reaction coordinate s is chosen such that it varies along the minimum energy path (MEP) and it passes through the saddle point of the potential. p_s is the momentum conjugated to s. The other n - 1 coordinates **Q** represent the vibrations orthogonal to the MEP, therefore are orthogonal to the reaction coordinate and **p** are their corresponding momenta. The dividing surface is set at the saddle point, perpendicularly to the reaction coordinate. Under these assumptions the classical equation for the rate constant 2.13 reads

$$k\left(T\right) = \int \frac{ds dp_s}{2\pi\hbar} \int \frac{d\boldsymbol{p} d\boldsymbol{Q}}{\left(2\pi\hbar\right)^{n-1}} \frac{e^{-\beta\left(\frac{p_s^2}{2\mu} + \frac{p^2}{2M} + V(s,\boldsymbol{Q})\right)}}{Q_r\left(T\right)} \delta\left(s\right) \frac{p_s}{\mu} P_r\left(s, p_s, \boldsymbol{Q}, \boldsymbol{p}\right) \tag{2.20}$$

where the Hamiltonian of the system is written explicitly and it assumed to be

separable. In this expression μ is the reduced mass associated to the reaction coordinate, while M is the total mass of the reactive system. Upon integration in ds one obtains

$$k(T) = \int \frac{dp_s d\boldsymbol{p} d\boldsymbol{Q}}{(2\pi\hbar)^n} \frac{e^{-\beta\left(\frac{p_s^2}{2\mu}+\frac{\boldsymbol{p}^2}{2M}+V(0,\boldsymbol{Q})\right)}}{Q_r(T)} \frac{p_s}{\mu} P_r(p_s, \boldsymbol{Q}, \boldsymbol{p}) \tag{2.21}$$

If the potential is rescaled so that the reference for the potential energy is the value of the saddle point, i.e. $V_{sp} = V(0, \boldsymbol{Q}_{TS})$

$$k(T) = \int \frac{dp_s d\boldsymbol{p} d\boldsymbol{Q}}{(2\pi\hbar)^n} \frac{e^{-\beta\left(\frac{p_s^2}{2\mu}+\frac{\boldsymbol{p}^2}{2M}+V(0,\boldsymbol{Q})+V_{sp}-V_{sp}\right)}}{Q_r(T)} \frac{p_s}{\mu} P_r(p_s, \boldsymbol{Q}, \boldsymbol{p})$$

$$k(T) = e^{-\beta V_{sp}} \int \frac{d\boldsymbol{p} d\boldsymbol{Q}}{(2\pi\hbar)^n} \frac{e^{-\beta\left(\frac{\boldsymbol{p}^2}{2M}+V(0,\boldsymbol{Q})-V_{sp}\right)}}{Q_r(T)} \int dp_s \frac{p_s}{\mu} e^{-\beta\frac{p_s^2}{2\mu}} P_r(p_s, \boldsymbol{Q}, \boldsymbol{p}) \tag{2.22}$$

At this stage the approximation of direct dynamics is introduced. This is the fundamental assumption of TST, and it is introduced to build a rate expression that does not need information from real time dynamics. In this way the TST can be regarded as a purely thermodynamics approach. To state in a mathematical form the direct dynamics approximation the reaction probability is set to be 1 if at a fixed instant in time the momentum of the classical trajectory at the dividing surface points towards the products. On the contrary, if the momentum points in the opposite direction the probability of reaction is 0. This implies that the projector factor is approximated as an Heaviside function $P_r(p_s, \boldsymbol{Q}, \boldsymbol{p}) \simeq h(p_s)$. By substituting it in 2.22 and by solving the needed

integrations, the TST approximation of the rate constant is achieved

$$\begin{aligned} k_{TST}(T) =& e^{-\beta V_{sp}} \int \frac{d\boldsymbol{p}d\boldsymbol{Q}}{(2\pi\hbar)^n} \frac{e^{-\beta\left(\frac{p^2}{2M}+V(0,\boldsymbol{Q})-V_{sp}\right)}}{Q_r(T)} \int_0^{+\infty} dp_s \frac{p_s}{\mu} e^{-\beta\frac{p_s^2}{2\mu}} \\ =& e^{-\beta V_{sp}} \int \frac{d\boldsymbol{p}d\boldsymbol{Q}}{(2\pi\hbar)^n} \frac{e^{-\beta\left(\frac{p^2}{2M}+V(0,\boldsymbol{Q})-V_{sp}\right)}}{Q_r(T)} \int_0^{+\infty} dp_s \frac{1}{\beta}\left(-\frac{\partial e^{-\beta\frac{p_s^2}{2\mu}}}{\partial p_s}\right) \\ =& e^{-\beta V_{sp}} \int \frac{d\boldsymbol{p}d\boldsymbol{Q}}{(2\pi\hbar)^n} \frac{e^{-\beta\left(\frac{p^2}{2M}+V(0,\boldsymbol{Q})-V_{sp}\right)}}{Q_r(T)} \left(0-\left(-\frac{1}{\beta}\right)\right) \\ =& e^{-\beta V_{sp}} \int \frac{d\boldsymbol{p}d\boldsymbol{Q}}{(2\pi\hbar)^n} \frac{e^{-\beta\left(\frac{p^2}{2M}+V(0,\boldsymbol{Q})-V_{sp}\right)}}{Q_r(T)} \frac{1}{\beta} \\ =& \frac{k_b T}{h} e^{-\beta V_{sp}} \frac{Q^{\dagger}(T)}{Q_r(T)} \end{aligned} \tag{2.23}$$

To apply the TST only few information is required: the reactants and transition state partition functions $Q_r(T)$ and $Q^{\dagger}(T)$, plus the height of the potential barrier separating the reactants from the products V_{sp}.

However, it is good to state again that this formula implies some important simplifications. It is considered that the reactants are distributed according to the Boltzmann distribution, the coordinates are considered to be separable at the transition state, and above all the dynamics does not allow recrossing. These observations make evident that TST gives only an upper bound to the classical rate constant. Moreover, this formula has been derived in a classical way, so the values of the reaction constant thus calculated do not include quantum effects such as tunneling.

It is interesting to make a connection with the empirical formula given by Arrhenius

$$k_{\text{Arrhenius}}(T) = Ae^{-\frac{E_{\text{act}}}{RT}} \tag{2.24}$$

It was originally inferred by interpolation of experimental data,[33] but can be rationalized with a similar assumption than the one for TST, but from a macroscopic point of view. More specifically, it is considered that the reaction can take place only if the energy of the system is higher than the activation barrier E_{act}. In this case the reaction probability is $P(E) = h(E - E_{\text{act}})$. By defining the rate constant as the mean value of the reaction probability, and, if the states of the reactants follow the Boltzmann distribution, the Arrhenius

expression follows

$$\begin{aligned} k_{\text{Arrhenius}}(T) &= \int_0^{+\infty} e^{-\frac{E}{RT}} P(E)\, dE \\ &= \int_{E_{\text{act}}}^{+\infty} e^{-\frac{E}{RT}} h(E - E_{\text{act}})\, dE \\ &= \int_{E_{\text{act}}}^{+\infty} e^{-\frac{E}{RT}} dE \\ &\propto e^{-\frac{E_{\text{act}}}{RT}} \end{aligned} \tag{2.25}$$

2.4 Quantum Reactive Scattering

The theory of quantum reactive scattering gives the exact formulation of thermal rate constants in quantum mechanics. The qualitative picture of reactive process in terms of wavepacket quantum evolution described in the introduction chapter is rigorously equivalent to the time independent formulation based on the definition of the scattering matrix (S) elements.[4]

To recall this treatment, the example of a triatomic reaction is considered. There are many ways in which the triatomic ABC can fragment, for instance A + BC, AB + C or A + B + C. These different kinds of fragmentations are called arrangement channels. A chemical reaction is hence a transition from one of this arrangement channels to another. Taking into account the process A + BC $\rightarrow$ AB + C, there are two possible γ reactive channels. The initial arrangement is the $\gamma = \alpha$ channel of reactants, while the final fragment is the $\gamma = \beta$ channel of products. In the regions of the potential that correspond to reactants (products) configurations, the fragment A (B) is far away from the fragment BC (AB). These parts of the PES are the asymptotic regions of the potential, and, since the interaction between the fragments is negligible due to their long separation distance, the Hamiltonian of the systems becomes separable in this limit. As a result, the eigenfunctions that solve the asymptotic time independent Schrödinger equation can be written as a product of eigenfunctions of the internal degrees of freedom of the fragments $\chi_{\gamma,n}$ (n is the set of internal motion quantum numbers), times a translational wavefunction $\phi_{\gamma,\pm k}$ (k is the wave vector associated to the translation) that describes the relative motion of A or B towards the center of mass of the other fragment BC or AB

$$\begin{aligned} \hat{H}^{\infty}_{\gamma} \Psi^{\infty}_{\gamma,E} &= E \Psi^{\infty}_{\gamma,E} \\ \Psi^{\infty}_{\gamma,E} &= \chi_{\gamma,n} \phi_{\gamma,\pm k} \end{aligned} \tag{2.26}$$

The complete Hamiltonian $\hat{H}$, that describes the system both in the interaction region and in the asymptotic regions, has the from

$$\hat{H} = H_{\gamma}^{\infty} + V_{\gamma} \tag{2.27}$$

The definition 2.27 highlights that in the limit of large separation between the fragments $V_{\gamma} \to 0$, and the complete Hamiltonian tends to the corresponding separable Hamiltonian. Therefore, the eigenfunction of $\hat{H}$ are asymptotically coincident to the asymptotic eigenstates of equation 2.26. The eigenstates of the complete Hamiltonian are the scattering eigenstates and can be labeled according to the characteristics of the asymptotic eigenstates to which they correspond (boundary conditions). For example, the scattering eigenstate $\Psi_{\alpha,n}^{+}$, in the limit of large separation between the fragments, is coincident with the asymptotic eigenstate $\Psi_{\alpha,E}^{\infty} = \chi_{\alpha,n}\phi_{\alpha,+k}$ that represents the fragment with internal degrees of freedom n and that is entering the α reactive channel. Scattering eigenstates corresponding to respectively incoming or outgoing boundary conditions from different arrangement channels are orthogonal

$$\langle \Psi_{\gamma',n'}^{\pm} | \Psi_{\gamma,n}^{\pm} \rangle = \delta_{\gamma'\gamma}\delta_{n'n}\delta\left(E - E'\right) \tag{2.28}$$

while eigenstates associated with incoming boundary conditions and outgoing boundary conditions are in general not orthogonal. Their overlap is the definition of the elements of the scattering matrix. They are the transition amplitude from a state that enters the reactive channel α to a state that exits the products channel β with another set of quantum numbers

$$S_{\beta n',\alpha n}\left(E\right)\delta\left(E - E'\right) = \langle \Psi_{\alpha,n'}^{\pm} | \Psi_{\beta,n}^{\pm} \rangle \tag{2.29}$$

The scattering matrix elements are then used to build the cumulative reaction probability (CRP), whose definition is

$$N\left(E\right) = \sum_{J}\left(2J+1\right)\sum_{n,n'}\left|S_{n_{\alpha n'}n_{\beta n}}\left(E,J\right)\right|^{2} \tag{2.30}$$

Therefore, the meaning of the CRP is the sum of the probabilities to reach each of the available product states starting from each of the available initial states that are open at a certain value of the total energy E and for a certain total angular momentum J of the system. Once the cumulative reaction probability is known, it gives straightforward the thermal rate constant by averaging over the Boltzmann distribution that accounts for the available energy states when the system has a

certain temperature T

$$k(T) = \frac{1}{hQ_r(T)} \int_{-\infty}^{+\infty} dE e^{-\beta E} N(E) \tag{2.31}$$

where h is the Plank constant, β=1/k_BT (k_B is the Boltzmann constant), and $Q_r(T)$ is the reactants partition function per unit volume.

This approach, despite being complete and exact is not doable for complex systems. As a result, the state of the art of exact quantum scattering calculations is limited to systems including at most six atoms.[49, 50] It is also important to point out that equation 2.30 and 2.31 (and the ones derived from it that will be discussed in the next paragraphs) are not formally proved to be suitable for condensed phase processes because during the derivation it was assumed that the boundary conditions of the scattering process are the one of a gas phase reaction, that are different from scattering boundary conditions in condensed phase.[51]

2.5 Flux Operator Approaches in Quantum Mechanics

The scattering matrix holds all state-to-state information about the reactive process, thought it is not efficient to compute the thermal rate constant by adopting such a complicate scheme. For practical applications, for example, realistic modeling of combustion and of atmospheric phenomena, it is required to compute rate constants for thousands of elementary gas-phase reactions. Equation (2.30) can be regarded as an average over the detailed state-to-state information that finally is lost. It would be better to find a more "direct" way to compute rate constants, that avoids the complete scattering calculation.[5] Attempts in this direction were done independently and at the same time by Miller,[52] and McLafferty and Pechukas.[53] In both these papers appears the same quantum mechanical expression for the rate constant

$$k(T) = \frac{1}{Q_r(T)} Tr[e^{-\beta \hat{H}} \hat{F} \hat{P}] \tag{2.32}$$

where $\hat{H}$ is the Hamiltonian operator of the system, $\hat{F}$ is the quantum mechanical flux operator across a dividing surface that divides the reactants and the products, and $\hat{P}$ is the projection operator. The meaning of the equation is exactly the same as the one in formula 2.31, but it is cast in a new language. The advantage is that there is no longer explicit reference to scattering quantities. In words the

expression 2.32 says that the thermal rate constant is the quantum mechanical Boltzmann average of the reactive flux operator $\hat{F}\hat{P}$.

The concept of flux operator is derived by elaborating the definition of the rate constant from quantum scattering that was recalled in the previous section. The idea is to rewrite the quantum mechanical equations in the spirit of classical mechanics, exploiting the picture of trajectories that are run on the PES as a guiding concept. More specifically, one first defines a dividing surface $f(\boldsymbol{q})$ as a function of the coordinates $\mathbf{q}$ of the system, in the same fashion of the classical case as in section 2.2. Mimicking the idea of a swarm of classical trajectories that flow through the surface, one can define the flux of the wavefunction $\psi(\boldsymbol{q})$ through this surface. From the principle of conservation of the probability in quantum mechanics, the definition of the probability current density associated to the wavefunction ψ can be derived

$$S(\boldsymbol{q}, t) = \mathrm{Re}\left[\psi^* \hat{v} \psi\right] \tag{2.33}$$

where $\hat{v} = \frac{\hbar}{im}\frac{\partial}{\partial \boldsymbol{q}}$ is the velocity operator for a particle of mass m. This probability current density is defined in analogy to the classical current density, i.e. the average flux of the particle at the position $\mathbf{q}$ and at a specific time t. The analogy is only formal, since this definition of flux is invalid in quantum mechanics, because requires the precise knowledge of position and velocity at the same time, that is prohibited by the indetermination principle.[54] To obtain the flux through the surface, $S(\boldsymbol{q}, t)$ has to be integrated over the surface that can be written as

$$\mathrm{Re}\int d\boldsymbol{q}\delta\left[f(\boldsymbol{q})\right]\psi^*(\boldsymbol{q})\left(\frac{\partial}{\partial \boldsymbol{q}} f(\boldsymbol{q}) \cdot \hat{v}\right)\psi(\boldsymbol{q}) \tag{2.34}$$

where the delta function restricts the volume integration to the surface defined by $f(\boldsymbol{q})$, while the scalar product $\frac{\partial}{\partial \boldsymbol{q}} f(\boldsymbol{q}) \cdot \hat{v}$ means that only the amount of velocity that is perpendicular at each point to the surface is considered. From equation 2.34, the flux operator is defined as

$$\hat{F} = \delta\left[f(\boldsymbol{q})\right]\frac{\partial}{\partial \boldsymbol{q}} f(\boldsymbol{q}) \cdot \hat{v} \tag{2.35}$$

The projector operator in the rate expression 2.32 must take allow for the complete set of scattering eigenstates, that accounts for both incoming and

outgoing states. Then, the projector operator is defined as

$$\begin{cases} \hat{P}\Psi^{-}_{\alpha,n} = \Psi^{-}_{\beta,n} \\ \hat{P}\Psi^{+}_{\alpha,n} = 0 \end{cases} \tag{2.36}$$

and the complete sum over states in equation 2.31 is now rewritten with the same meaning in the form of a quantum operator trace

$$k(T) = \frac{1}{Q_r(T)} \sum_n \int_{-\infty}^{+\infty} dp_1 \, \langle \Psi^{+}_{\alpha,n} | \hat{F} e^{-\beta \hat{H}} \hat{P} | \Psi^{-}_{\alpha,n} \rangle \tag{2.37}$$

This is equivalent to expression 2.32 because the Boltzmann operator and $\hat{P}$ commute.[52] Equation 2.37 is also the quantum analogue of the classical expression 2.13.

2.6 Flux-Flux Correlation Function in Quantum Mechanics

It was only in 1983 that Miller, Schwartz, and Tromp reformulated the exact quantum reaction rate in terms of flux correlation functions. Yamamoto had already provided expressions for reaction rates based on the linear response theory. Miller's expression turned out to be a generalization of Yamamoto's ones.[42, 51]

The derivation is done in analogy to the one given in section 2.2 for the classical case. The first observation is that the quantum analogue of the classical projector of equation 2.17 can be written just by considering that the time evolution is now carried out quantum mechanically. Its expression is

$$P_r = \lim_{t \to \infty} e^{\frac{i\hat{H}t}{\hbar}} \hat{h}(f) \, e^{-\frac{i\hat{H}t}{\hbar}} \tag{2.38}$$

where $h(f)$ Heaviside function. Following the same procedure used in the chain of equalities of equation 2.18, and recalling that the time derivative of a quantum mechanical operator $\hat{a}$ that does not explicitly depend on time is given by $\frac{d\hat{a}}{dt} = \frac{i}{\hbar}\left[\hat{H}, \hat{a}\right]$, one obtains

$$\hat{P}_r = \int_0^{\infty} dt \frac{d}{dt} e^{\frac{i\hat{H}t}{\hbar}} \hat{h}(f) \, e^{-\frac{i\hat{H}t}{\hbar}} = \int_0^{\infty} dt e^{\frac{i\hat{H}t}{\hbar}} \frac{i}{\hbar} \left[\hat{H}, \hat{h}\right] e^{-\frac{i\hat{H}t}{\hbar}} \tag{2.39}$$

The quantum flux operator 2.35 can now be written in terms of the momentum

operator, by using the identity $\hat{p} = -i\hbar\frac{\partial}{\partial q} = m\hat{v}$

$$\begin{aligned}\hat{F} &= \delta\left[f\left(\boldsymbol{q}\right)\right]\frac{\partial f\left(\boldsymbol{q}\right)}{\partial \boldsymbol{q}}\cdot\hat{v} \\ &= \frac{1}{m}\frac{\partial h\left[f\left(\boldsymbol{q}\right)\right]}{\partial t}\cdot\hat{p} \\ &= \frac{1}{2m}\left[\frac{\partial h\left[f\left(\boldsymbol{q}\right)\right]}{\partial t}\cdot\hat{p} + \hat{p}\cdot\frac{\partial h\left[f\left(\boldsymbol{q}\right)\right]}{\partial t}\right] \\ &= \frac{i}{\hbar}\left[\hat{H},\hat{h}\right]\end{aligned} \tag{2.40}$$

This means that the projection operator is the time integral of the quantum time evolution of the flux operator

$$\hat{P}_r = \int_0^\infty dt e^{\frac{i\hat{H}t}{\hbar}}\hat{F}e^{-\frac{i\hat{H}t}{\hbar}} \tag{2.41}$$

Inserting the definition 2.41 into the trace 2.32 the desired rate expression in term of a quantum mechanical correlation function is found

$$k_{QM}\left(T\right) = Q_r\left(T\right)^{-1}\int_0^\infty dt C_f\left(t\right) \tag{2.42}$$

where

$$C_f\left(t\right) = \mathrm{tr}\left(e^{-\beta\hat{H}}\hat{F}e^{\frac{i\hat{H}t}{\hbar}}\hat{F}e^{-\frac{i\hat{H}t}{\hbar}}\right) \tag{2.43}$$

This formulation is still exact, i.e. free of any approximations in principle, in fact descends directly from the scattering expression of rate constant.[5] This method makes possible to evaluate the rate constant with a short time quantum dynamics, because the flux-flux correlation of expression 2.43 decays fast in time. Therefore, it is not necessary to extend the limit of integration in equation 2.42 to infinity but only to a suitable amount of time to observe that the correlation function values has a stable zero value. This time interval is usually of the order of $\hbar\beta$, as showed for the example of the collinear H + H_2 reaction in figure 2.5.

It must be pointed out that equation 2.42 is not the unique form that gives the exact quantum mechanical rate. It has been shown that there are other two equivalent expressions.[42] The first one is given by the long time limit of the flux side correlation function

$$k_{QM}\left(T\right) = Q_r\left(T\right)^{-1}\lim_{t\to\infty} C_{fs}\left(t\right) \tag{2.44}$$

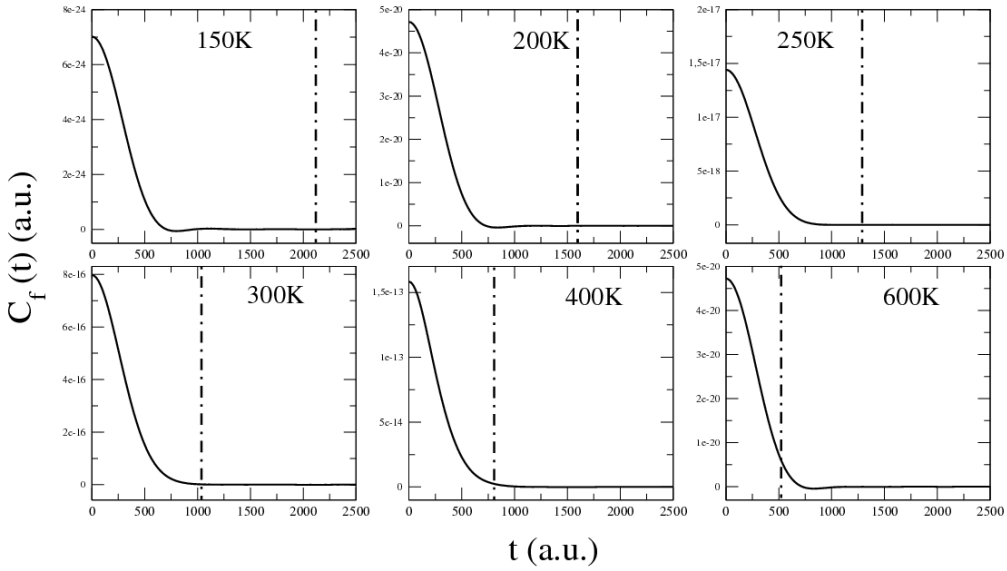

Figure 2.5: The flux flux correlation function computed with equation 2.43 for the case of H + H_2 collinear reaction at six temperatures (150K, 200K, 250K, 300K, 400K, and 600K). The vertical dashed lines indicate the value of $\hbar\beta$ in each case, respectively 2105 a.u., 1579 a.u., 1263 a.u., 1052 a.u., 789 a.u., and 525 a.u. (1a.u. $\simeq 2.42 \times 10^{-17}$s. In all cases the decay time of the flux-flux correlation function is smaller, or at least comparable, to these values.

where

$$C_{fs}(t) = \mathrm{tr}\left(e^{-\beta\hat{H}}\hat{F}e^{\frac{i\hat{H}t}{\hbar}}\hat{h}(f)\,e^{-\frac{i\hat{H}t}{\hbar}}\right) \tag{2.45}$$

the second one is the long time limit of the time derivative of the side side correlation function

$$k_{QM}(T) = Q_r(T)^{-1}\lim_{t\to\infty}\frac{d}{dt}C_s(t) \tag{2.46}$$

where

$$C_s(t) = \mathrm{tr}\left(e^{-\beta\hat{H}}\hat{h}(-f)\,e^{\frac{i\hat{H}t}{\hbar}}\hat{h}(f)\,e^{-\frac{i\hat{H}t}{\hbar}}\right) \tag{2.47}$$

The three correlation functions are related to each other as

$$C_f(t) = \frac{d}{dt}C_{fs}(t) = \frac{d^2}{dt^2}C_s(t) \tag{2.48}$$

and, since $C_f(t)$ is an even function of time, $C_{fs}(t)$ is odd and $C_s(t)$ is even.

2.7 Approximations

The expression 2.43 can be rearranged in a more suitable way. First, the Boltzmann operator can be split as $e^{-\beta\hat{H}} = e^{-\frac{\beta}{2}\hat{H}}e^{-\frac{\beta}{2}\hat{H}}$. Secondly, by noticing that the flux operator $\hat{F}$ and the half Boltzmann operator commute and by exploiting the property of quantum mechanical traces that are invariant upon cyclic permutation of the argument operators, one obtains

$$\begin{aligned} C_f(t) &= \mathrm{Tr}\left(e^{-\beta\hat{H}}\hat{F}e^{\frac{i\hat{H}t}{\hbar}}\hat{F}e^{-\frac{i\hat{H}t}{\hbar}}\right) \\ &= \mathrm{Tr}\left(e^{-\frac{\beta}{2}\hat{H}}e^{-\frac{\beta}{2}\hat{H}}\hat{F}e^{\frac{i\hat{H}t}{\hbar}}\hat{F}e^{-\frac{i\hat{H}t}{\hbar}}\right) \\ &= \mathrm{Tr}\left(e^{-\frac{\beta}{2}\hat{H}}\hat{F}e^{-\frac{\beta}{2}\hat{H}}e^{\frac{i\hat{H}t}{\hbar}}\hat{F}e^{-\frac{i\hat{H}t}{\hbar}}\right) \\ &= \mathrm{Tr}\left(\hat{F}e^{-\frac{\beta}{2}\hat{H}}e^{\frac{i\hat{H}t}{\hbar}}\hat{F}e^{-\frac{i\hat{H}t}{\hbar}}e^{-\frac{\beta}{2}\hat{H}}\right) \end{aligned} \tag{2.49}$$

At this stage, the complex time $t_c = t - \frac{i\hbar\beta}{2}$ can be introduced and the flux-flux correlation function is defined as

$$C_f(t) = \mathrm{Tr}\left(\hat{F}e^{\frac{i\hat{H}t_c^*}{\hbar}}\hat{F}e^{-\frac{i\hat{H}t_c}{\hbar}}\right) \tag{2.50}$$

The operator $e^{-\frac{i\hat{H}t_c}{\hbar}}$ has the same form of the ordinary quantum time propagator, but here the time variable t_c can assume complex values. The form of equation 2.50 points out that to evaluate the rate constant it is required (even if for a short time) a complex time evolution, a problem that is very hard to address. In fact, even if exact time dependent methods are well known, their scaling with the dimensionality of the system remains a major problem.[7] The state of the art of quantum calculation of the rate constant using the flux-flux formalism is represented by its combination with the Multi-Configurational Time-Dependent Hartree (MCTDH) approach.[55] With this approach a direct calculation of accurate thermal rate constants has been obtained for systems up to twelve degrees of freedom.[56, 57, 58] To make it possible to compute rates for more complex systems, it is however necessary to develop approximate approaches.

A first possibility to build an approximation to the rate constant is to quantum mechanically account for the statistical part, and to treat the much more challenging real time dynamics with a classical-mechanics based approximation. This is the case of semiclassical dynamics, a very promising and effective way to deal with large-size systems which allows to regain quantum mechanical features starting from classical simulations. Over the years, many SC techniques have been developed to efficiently tackle the sign problem for applications to both kinetics[59, 60, 61, 62, 63, 64, 65, 66, 67, 68, 69, 70, 71, 72, 73, 74, 75, 76, 77, 78, 79, 80, 81, 82, 83, 84, 85, 86, 87] and spectroscopy.[88, 89, 30, 90, 91, 92, 93, 32] More specifically, the starting point of this class of techniques is the observation that the main contribution to the time propagator matrix elements comes from classical paths that connect an initial position x to a final position x' in a time interval t. The exact Feynman Path Integral expression of the quantum time propagator is

$$\langle x'|e^{-\frac{i\hat{H}t}{\hbar}}|x\rangle = \sqrt{\frac{m}{2\pi i\hbar t}}\int \mathcal{D}\left[x\left(t\right)\right] e^{\frac{i}{\hbar}S(x,x',t)} \tag{2.51}$$

where $\hat{H}$ is the Hamiltonian operator, m the mass of the system, S(x,x',t) is the action and the symbol $\mathcal{D}[x\left(t\right)]$ represents the integration over all paths. A sound approximation to the exact propagator can be obtained by considering only the contribution from classical path. Furthermore, the exponent in equation 2.51 can be expanded in Taylor series

$$\langle x'|e^{-\frac{i\hat{H}t}{\hbar}}|x\rangle = \sqrt{\frac{m}{2\pi i\hbar t}}\sum_{\text{classical paths}}\int \mathcal{D}\left[x\left(t\right)\right] e^{\frac{i}{\hbar}\left(S+\delta S+\frac{1}{2}\delta^2 S\right)} \tag{2.52}$$

and recalling that for classical trajectories the least action principle prescribes

δS=0, the integral in expression 2.52 can be solved via stationary phase approximation which is detailed in appendix 2.7. The most basic version of this approximation is the Van Vleck Semiclassical propagator (VV) whose expression in N dimensions is

$$\langle x'|e^{-\frac{i\hat{H}t}{\hbar}}|x\rangle_{VV}^{SC} = \left(\frac{1}{2\pi i\hbar}\right)^{\frac{N}{2}} \left[\left|-\frac{\partial^2 S}{\partial x'\partial x}\right|\right]^{\frac{1}{2}} e^{\frac{i}{\hbar}S^{CL}(x,x',t)} \tag{2.53}$$

Interestingly, even if expression 2.53 is based only on classical trajectories and their classical action, it can regain quantum information. Many other semiclassical approximations that are based on the same concept have been designed to improve the practical applicability of this formalism. For instance, the semiclassical initial value representation (SC-IVR) aims at restating the propagator expression as a function of only initial conditions (x,p), avoiding the dependence on the final position x'. SC-IVR implementations, based on phase space real-time classical trajectory integration, such as the van Vleck SC-IVR (VV-IVR) and the forward-backward SC-IVR (FB-IVR), have been applied to the calculation of the thermal rate equations (2.42) and (2.43). [81, 94, 65, 64, 95, 74] For the same kind of application also the linearized SC-IVR (LSC-IVR) has been widely employed.[87, 68, 86] This approach consists in a linearization of the general SC-IVR expression for the correlation function. In this way, in a LSC-IVR calculation initial conditions of the classical trajectories are weighted by a Wigner function corresponding to the Boltzmannized flux operator. This linearized approximation to the SC-IVR is thus practical for systems with many degrees of freedom (e.g. a reaction coupled to a bath of harmonic oscillators). However the LSC-IVR describes quantum effects accurately only for short times ($t \lesssim \hbar\beta$). For longer times quantum effects are lost. Therefore, this approach is more suitable for describing quantum effects transition state theory-type dynamics in the absence of recrossing dynamics.[96]

An alternative and widely used class of classical-trajectory based approaches to rate constant calculations is constituted by the Ring Polymer Molecular Dynamics (RPMD),[97, 98, 99] which can also provide TST-like versions,[100, 101] and the Centroid Molecular Dynamics (CMD).[102, 103, 104] Differently from semiclassical techniques, CMD and RPMD make use of the imaginary-time path integral formalism, and take advantage of the exact mapping between a quantum mechanical particle and a classical "ring polymer", i.e. a ring of n replicas (beads) of the actual system where nearest neighbors are linked by harmonic springs. Even if based on static quantum information these methods can be used to approximate dynamical properties in quantum mechanical systems. On

one hand, in the CMD approach, a classical molecular dynamics simulation is performed on the effective potential generated by the thermal fluctuations of the ring polymer around its centroid (average position of the beads). On the other hand, RPMD exploits the equivalence between the outcome of application of the classical isomorphism to find the thermal expectation value of a product of two position-dependent operators and the zero time limit of the Kubo-transformed real-time correlation function of the two operators. The RPMD method therefore attempts to extend this correspondence to times t > 0.[97] As a result, RPMD uses the classical time evolution in the extended phase space of the ring polymer to approximate the evolution of the actual system. Classical dynamics generated by the artificial Hamiltonian has no obvious connection with the true quantum dynamics, and, at present, there is no systematic derivation of the approximation, even if links with the Semiclassical Instanton theory have appeared in the literature.[99] Nevertheless these methods can be satisfactorily applied to systems in condensed phase. This efficiency arises because for condensed phase systems real-time quantum coherence, which is neglected by RPMD, is not important.[105]

Another strategy is to approximate the rate expression by completely neglecting the real time dynamics. In fact, it is possible to calculate the quantum thermal factor $e^{-\beta\hat{H}}$ relying on the imaginary time Path Integral (PI) formulation.[106] In this case, the Monte Carlo (MC) integration of the PI representation of the thermal factor is doable even for systems with more than 100 dimensions.[107] On the contrary, other quantum methods[108, 109, 110] which explicitly include real-time evolution face the difficult sign problem which hampers the convergence of the MC integration because the dynamical factor $e^{-\frac{i\hat{H}t}{\hbar}}$ is an oscillating function of time due to the imaginary exponent. For this reason a method like the inverse Laplace transform approach attempts to obtain real time results from imaginary time propagation. Unfortunately the analytic continuation on which the method is based is ill behaved, and only short time inversion is possible. This is not sufficient to get a reliable rate constant estimate.[51, 111, 112, 113] Therefore, it is interesting to look for a quantum analogue of TST to overcome the approximation of classical dynamics, while retaining the TST-peculiar direct dynamics approximation. This quest is still under search. The main issue is the difficulty to have an universal definition of Quantum Transition State Theory (QTST) because in quantum mechanics any local evaluation of the reactive flux is invalidated by the uncertainty principle.[114] The most straightforward inclusion of quantum effects in a TST formulation consists in evaluating quantum mechanically the partition functions of the reactants and of the transition state.

A more refined strategy is to employ semiclassical theories. For instance the Rice–Ramsperger–Kassel–Marcus theory (RRKM)[115, 116] starts from classical TST and gives the rate of decay in a unimolecular reaction in terms of counts of states of the reactants and the transition state. Its expression for a total energy E and total angular momentum J is

$$k_{RRKM}(T) = \frac{N(E,J)}{h\rho(E,J)} \tag{2.54}$$

In equation 2.54 N(E,J) is the number of quantum states of the TS for a given J with energy less or equal to E in the degrees of freedom orthogonal to the reaction coordinate. ρ(E,J) is the density of states of the reactant. Within RRKM theory semiclassical estimates of these quantities are employed. In fact, accounting for anharmonicities and couplings between the degrees of freedom is far from trivial. Furthermore, to account for tunneling effects it is necessary to include corrections to N(E,J). This task is usually achieved in an ad hoc way, by adopting one dimensional tunneling corrections along the reaction coordinate.[117] Another version of QTST is called Semiclassical Instanton (SCI),[38, 39, 118, 119, 120] whose starting point is the substitution of the projection operator $\hat{P}$ in equation 2.32 with a step function of the momentum operator. The main feature of SCI is that the imaginary time propagator $e^{-\beta H}$ is approximated by adapting the semiclassical derivation of equation 2.53 from equation 2.51 at imaginary times. The Boltzmann matrix elements within this approximation make it possible to evaluate the thermal average of any operator via further stationary phase approximations. The final SCI expression is formally similar to that of classical TST, with the difference that all quantities in it refer to the full classical dynamics on the inverted potential energy surface. In place of the vibrational frequencies of the activated complex which appear in the conventional TST, the semiclassical expression contains characteristic frequencies related to the stability properties of a periodic classical trajectory, called the instanton.[38] SCTST is closely linked to SCI and both theories will be extensively presented in chapter 3. A further development of these QTST methods, that is of particular interest for the work presented in chapter 6, is the Quantum Instanton (QI).[121, 122, 73] QI is inspired by the SCI theory but adopts an exact quantum PI treatment for the quantum Boltzmann statistics. Being a TST approach, the only quantity which has to be evaluated is the Boltzmann operator (and its thermodynamic β derivatives) that can be estimated by imaginary time Path Integral techniques.[95, 123] QI has many appreciable features. First, it is very accurate, within 20%, over a wide temperature range, from the deep tunneling regime up to the higher

temperatures. Secondly, it makes no arbitrary assumptions about a specific reaction path or reaction coordinate. Finally, QI has been proven to incorporate correctly all tunneling, corner-cutting, and quantum-fluctuation effects and has provided very satisfactory results for a variety of problems, ranging from gas phase reactions,[122, 124, 121, 95, 125] to chemical reactions in a polar solvent,[106] from gas-surface reactions,[126, 127] to isotopic effects.[128, 129, 130, 131, 132]

The work presented in this thesis is aimed to develop new advances in the computation of rate constants in the gas phase. A first novel contribution is meant to speed up the evaluation of SCTST rate constants by means of the efficient parallel implementation reported in chapter 4. The other new method presented in chapter 6 addresses the problem of including real time dynamics contributions into the rate constant, thus overcoming the QTST approximation, but still without solving the full quantum dynamics.

Appendix 1.A: Application of Onsager's Regression Hypothesis to Chemical Kinetics

The macroscopic rate equation for the reaction

$$A \underset{k_{AB}}{\overset{k_{BA}}{\rightleftarrows}} B \tag{2.55}$$

can be expressed in terms of the instantaneous concentration of the two chemical species $c_A(t)$ and $c_B(t)$ and the forward and backward rate constant k_{BA} and k_{AB}. Under the constraint that at any time $c_A(t) + c_B(t)$ is a constant value the set of differential equations that describes the evolution of the system is

$$\begin{cases} \frac{dc_A}{dt} = & -k_{BA}c_A(t) + k_{AB}c_B(t) \\ \frac{dc_B}{dt} = & k_{BA}c_A(t) - k_{AB}c_B(t) \end{cases} \tag{2.56}$$

Its solution provides

$$c_A(t) - c_A^{eq} = \left[c_A(0) - c_A^{eq}\right] e^{-t(k_{AB}+k_{BA})} \tag{2.57}$$

where c_A^{eq} is the constant concentration of A at equilibrium.

If $q(t)$ is the reaction coordinate, $h[q(t)]$ defined in equation 2.3, is a dynamical variable whose instantaneous variation is linked to the the instantaneous concentration of A. The Onsager's principle can be applied. Dealing with a

system that is prepared in a non-equilibrium state that is allowed to relax to equilibrium, the Onsager's principle states that "the relaxation of a macroscopic non-equilibrium distribution is governed by the same laws as the regression of spontaneous microscopic fluctuations". This correspondence is valid for a system that is weakly displaced from equilibrium, and is thus described by the linear response theory. In fact, in the situation of a small perturbation that brings the system out of equilibrium, it is impossible to distinguish between spontaneous fluctuations and deviations from equilibrium that are externally prepared. Therefore, Onsager's hypothesis can be derived by first principles in the framework of linear response theory.[133]

In the case of the considered chemical reaction, the system is prepared in a non-equilibrium situation, since at the beginning the reactant A and B are put in contact in the reactant vessel at an arbitrary initial concentration. The reaction starts and it is left to itself, and spontaneously evolves towards equilibrium. In this case the relaxation of macroscopic non-equilibrium distribution is expressed by the ratio $\left[c_A(t) - c_A^{eq}\right] / \left[c_A(0) - c_A^{eq}\right]$, while the decay of spontaneous microscopic fluctuation is expressed in term of the reaction coordinate by the ratio $\langle \delta h[q(0)]\, \delta h[q(t)] \rangle / \langle \delta h[q(0)]\, \delta h[q(0)] \rangle$, $\delta h[q(t)]$ is defined according to 2.5. Finally, it is possible to write

$$\frac{c_A(t) - c_A^{eq}}{c_A(0) - c_A^{eq}} = \frac{\langle \delta h[q(0)]\, \delta h[q(t)] \rangle}{\langle \delta h[q(0)]\, \delta h[q(0)] \rangle} \tag{2.58}$$

that according to 2.57 is[43]

$$e^{-t(k_{AB}+k_{BA})} = \frac{\langle \delta h[q(0)]\, \delta h[q(t)] \rangle}{\langle \delta h[q(0)]\, \delta h[q(0)] \rangle} \tag{2.59}$$

and is the same expression as equation 2.9.

Appendix 2.A: The Stationary Phase Approximation

The stationary phase is a way to approximate an integral of the form

$$I = \int_{-\infty}^{+\infty} dt g(t)\, e^{-f(t)} \tag{2.60}$$

where $f(t)$ and $g(t)$ are continuous functions. Furthermore, $f(t)$ is a function with well separated stationary points, while $g(t)$ is almost constant (compared to $f(t)$) over the interval of integration. Each stationary point of $f(t)$, corre-

sponding to an extremum of the function, generates a very sharp feature in the plot of the exponential $e^{-f(t)}$. As a result, the main contributions to the integral come from the regions around these stationary points. A strategy to approximate the integral is to expand the exponent in Taylor series around each stationary point. For example, if a unique stationary point exists and it is located at t*, such that $f^{'}(t*) = 0$,

$$\begin{aligned} I \simeq & g(t*) \int_{-\infty}^{+\infty} dt e^{-\left[f(t*)+(t-t*)f^{'}(t*)+\frac{1}{2}(t-t*)^2 f^{''}(t*)\right]} \\ = & g(t*)\, e^{-f(t*)-\frac{1}{2}t*^2 f^{''}(t*)} \int_{-\infty}^{+\infty} dt e^{-\frac{f^{''}(t*)}{2}t^2-2\left[-\frac{f^{''}(t*)}{2}\right]t} \\ = & g(t*) \sqrt{\frac{2\pi}{|f^{''}(t*)|}} e^{-f(t*)} \end{aligned} \tag{2.61}$$

where the last integration has been performed recalling the Gaussian integral $\int_{-\infty}^{+\infty} dx e^{-ax^2-2bx} = \sqrt{\frac{\pi}{a}} e^{\frac{b^2}{a}}$. If there are N stationary points the integral is approximated as

$$I \simeq \sum_{i=1}^{N} g(t_i*) \sqrt{\frac{2\pi}{|f^{''}(t_i*)|}} e^{-f(t_i*)} \tag{2.62}$$

3 Semiclassical Reaction Rate Theory

It has been shown that for the H + H_2 reaction classical TST agrees exactly with a purely classical trajectory simulation, if the calculations are restricted to an energy region just above the barrier on the minimum energy path. The low energy constraint is necessary to minimize recrossing. This suggests that, if the interest is in studying reactions at low collision energy, the TST assumption of direct dynamics is a good one.[52, 53] Even from the quantum mechanical point of view, it was calculated that for H + H_2 collinear reaction the stream lines of quantum flux are smooth at low energies.[52]

However, as discussed in the introduction, TST is a classical theory, and at low energies and temperatures the contribution of tunneling to the reaction rate can not be ignored. Ad hoc tunneling corrections along the reaction coordinate to the classical TST can be tried but they usually lead to an overestimation of the rate constant. This kind of empirical corrections are obtained after assuming a specific functional form for the potential experienced by the reaction coordinate. This potential is a one dimensional barrier because in the TST approximation the reaction coordinate is considered separable. For instance, the Wigner transmission coefficient is found if the barrier is modeled as an inverted parabola.[134] Another possibility is to consider a one dimensional Eckart barrier, whose tunneling transmission coefficient is analytically derived.[135] To deal with a general barrier shape in one dimension, the WKB semiclassical theory can be applied.[136] For instance, by applying WKB to a truncated parabola potential a generalization of Wigner's result is found.[137, 138] In general, the WKB theory indicates that the probability of tunneling through a barrier depends exponentially on the imaginary action (a classical action computed on the upside down potential energy surface) accumulated between the two turning points.[136]

The failure of simple quantum corrections is due to an intrinsic drawback of TST which makes the inaccurate assumption of coordinate separability at the PES saddle point. This is clearly demonstrated by the presence of corner cutting effects that can be even found in classical trajectories simulations (see the example in chapter 1). A better way to obtain an approximation to the rate constant, that avoids any time propagation but simultaneously includes quantum effects, would be the implementation of TST direct dynamics assumption into

quantum mechanics, without assuming the further approximation of separability of the reaction coordinate at the saddle point. In such a theory, the tunneling would not be confined to a specific reaction path and orthogonal modes at the saddle point would effectively contribute to the reactive process. A formulation with these characteristics was derived by Miller, and it is called Semiclassical Transition State Theory (SCTST).[38, 39]

A first goal of this thesis is to extend to high dimensional systems the inclusion of quantum effects in rate constant computations. SCTST has been implemented for parallel architectures. In fact another advantage of this semiclassical theory is that it allows to calculate rate constants requiring only the evaluation of the partition functions of reactants and of the transition state. However, computing partition functions for high dimensional systems remains a difficult task, which requires a specific computational implementation to make it feasible. After reviewing the SCTST derivation and its parent semiclassical instanton theory in this chapter, a new algorithm for the efficient calculation of partition functions required to evaluate SCTST rate constants will be presented in chapter 4.

3.1 Extending TST to Quantum Mechanics

For simplicity a collinear reaction is considered. The PES for this system is two dimensional, and it is described by two normal modes at the saddle point denoted as u and s, as sketched in figure 3.1. A dividing surface is set orthogonally to the reactive coordinate s. For this two dimensional system the exact quantum expression for the reaction rate 2.32 reads as

$$k(T) = \frac{1}{Q_r} Tr\left[e^{-\beta\hat{H}}\delta(s)\,\hat{p}_s\hat{P}\right] \tag{3.1}$$

where the flux operator 2.35 has been written for this special case, and $\hat{p}_s$ is the momentum operator associated with the reaction coordinate s.

The simplest idea to produce a TST-like approximation from this quantum mechanical formula, would be to approximate the projection operator $\hat{P}$ as a step function of the type

$$h(p_s) = \begin{cases} 1 & p_s > 0 \\ 0 & p_s < 0 \end{cases} \tag{3.2}$$

Unfortunately, a problem arises, because this approximate projector operator does not commute with the Hamiltonian $\hat{H}$ operator, as the exact $\hat{P}$ does. For this reason, it is not clear how to choose the order of the operators in the trace.

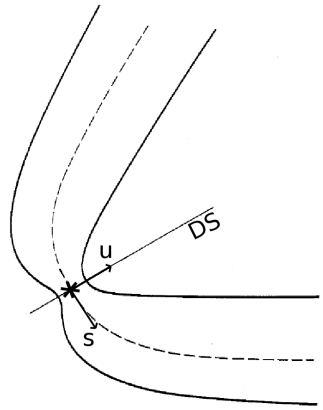

Figure 3.1: Setting of the dividing surface (DS) and the normal modes coordinates s and u for a generic collinear reaction. The dashed line is the minimum energy path (MEP) that crosses the saddle point of the potential (highlighted by the star). s is the reactive coordinates that is directed towards the products basin. The straight line is the dividing surface set at the saddle point that is parallel to the other normal mode coordinate u.

To overcome this difficulty, the Weyl correspondence rule is applied (for more information see the Appendix C of reference [139]). It gives a rule to build the operator which corresponds to a function in the phase space. To apply this rule, first the rate constant 3.1 can be written as

$$k(T) = \frac{1}{Q_r} \int ds \int du \int ds' \int du' \, \langle s, u | e^{-\beta \hat{H}} | s', u' \rangle \, \langle s', u' | \hat{R} | s, u \rangle \tag{3.3}$$

where an identity has been inserted to separate the Boltzmann factor from the other operators. Then, the operator $\hat{R}$ corresponding to the function $r(s, p_s) = \delta(s)\, p_s h(p_S)$ is needed. Therefore, its matrix elements are obtained thanks to the Weyl rule

$$\langle s', u' | \hat{R} | s, u \rangle = \delta(u' - u)\, \delta\left(\frac{s' + s}{2}\right) \frac{\hbar}{2\pi m_s} \left[-\frac{1}{(s' - s)^2} \right] \tag{3.4}$$

Inserting the result 3.4 in equation 3.3, upon integration by parts, the final QTST

expression is derived

$$k_{QM}^{TST}(T) = \frac{1}{Q_r}\frac{\hbar}{4\pi m_s}\int_{-\infty}^{+\infty} du \int_{-\infty}^{+\infty} ds \left(-\frac{1}{s}\right)\frac{\partial}{\partial s}\langle s,u|e^{-\beta\hat{H}}|-s,u\rangle \tag{3.5}$$

It is interesting to elaborate equation 3.5 in the case of a separable Hamiltonian $\hat{H} = \hat{H}_u + \hat{H}_s$. In this case the formula simplifies to

$$\begin{aligned} k_{QM}^{TST}(T) =& \frac{1}{Q_r}\frac{\hbar}{4\pi m_s}\int_{-\infty}^{+\infty} du \int_{-\infty}^{+\infty} ds \left(-\frac{1}{s}\right)\frac{\partial}{\partial s}\langle s,u|e^{-\beta\hat{H}_u}e^{-\beta\hat{H}_s}|-s,u\rangle \\ =& \frac{1}{Q_r}\frac{\hbar}{4\pi m_s}\int_{-\infty}^{+\infty} du \langle u|e^{-\beta\hat{H}_u}|u\rangle \int_{-\infty}^{+\infty} ds \left(-\frac{1}{s}\right)\frac{\partial}{\partial s}\langle s|e^{-\beta\hat{H}_s}|-s\rangle \\ =& \frac{k_B T}{h}\frac{Q_u}{Q_r}\frac{\hbar\beta}{2m_s}\int_{-\infty}^{+\infty} ds \left(-\frac{1}{s}\right)\frac{\partial}{\partial s}\langle s|e^{-\beta\hat{H}_s}|-s\rangle \end{aligned} \tag{3.6}$$

where $\int_{-\infty}^{+\infty} du \langle u|e^{-\beta\hat{H}_u}|u\rangle$ is identified as the partition function Q_u for the coordinate u, and m_s is the reduced mass associated to the motion along the coordinate s. Comparing the last expression in equation 3.6 with the usual TST formula 2.23, the term

$$\frac{\hbar\beta}{2m_s}\int_{-\infty}^{+\infty} ds \left(-\frac{1}{s}\right)\frac{\partial}{\partial s}\langle s|e^{-\beta\hat{H}_s}|-s\rangle \tag{3.7}$$

acts as a the tunneling correction Γ. In the following, this factor is evaluated adopting two specific models to describe the motion along the reaction coordinate.

A first possibility is to approximate the motion along the reaction coordinate s as a translation. In this case, the Hamiltonian is the free particle one $\hat{h}_s = \frac{\hat{p}^2}{2m_s}$, and the matrix elements $\langle s|e^{-\beta\hat{H}_s}|-s\rangle$ are

$$\begin{aligned} \langle s|e^{-\beta\hat{H}_s}|-s\rangle =& \int_{-\infty}^{\infty} dp_s \langle s|p_s\rangle \langle p_s|e^{-\frac{\beta p_s^2}{2m_s}}|-s\rangle \\ =& \int_{-\infty}^{\infty} dp_s e^{-\frac{\beta p_s^2}{2m_s}} \langle s|p_s\rangle \langle p_s|-s\rangle \\ =& \frac{1}{2\pi\hbar}\int_{-\infty}^{\infty} dp_s e^{-\frac{\beta p_s^2}{2m_s}+i\frac{2s}{\hbar}p_s} \\ =& \frac{1}{2\pi\hbar}\sqrt{\frac{2\pi m_s}{\beta}}e^{-\frac{2m_s}{\hbar^2\beta}s^2} \\ =& \sqrt{\frac{m_s}{2\pi\beta\hbar^2}}e^{-\frac{2m_s}{\hbar^2\beta}s^2} \end{aligned} \tag{3.8}$$

where the definitions $\langle s|p_s\rangle = \frac{e^{\frac{ip_s s}{\hbar}}}{\sqrt{2\pi\hbar}}$, and $\langle p_s|-s\rangle = (\langle -s|p_s\rangle)^* = \left(\frac{e^{-\frac{ip_s s}{\hbar}}}{\sqrt{2\pi\hbar}}\right)^* = \frac{e^{\frac{ip_s s}{\hbar}}}{\sqrt{2\pi\hbar}}$ were used, and the integral in $\mathrm{d}p_s$ is a Gaussian integral. Inserting the result 3.8 into 3.6 the tunneling correction is

$$\begin{aligned}
\Gamma_{fp} =& \frac{\hbar^2\beta}{2m_s}\int_{-\infty}^{+\infty} ds\left(-\frac{1}{s}\right)\frac{\partial}{\partial s}\sqrt{\frac{m_s}{2\pi\beta\hbar^2}}e^{-\frac{2m_s}{\hbar^2\beta}s^2} \\
=& \frac{\hbar^2\beta}{2m_s}\sqrt{\frac{m_s}{2\pi\beta\hbar^2}}\int_{-\infty}^{+\infty} ds\left(-\frac{1}{s}\right)\left(-\frac{4m_s}{\hbar^2\beta}s\right)e^{-\frac{2m_s}{\hbar^2\beta}s^2} \\
=& \left(\frac{4m_s}{\hbar^2\beta}\right)\sqrt{\frac{\hbar^2\beta}{m_s 8\pi}}\int_{-\infty}^{+\infty} ds e^{-\frac{2m_s}{\hbar^2\beta}s^2} \\
=& \left(\frac{4m_s}{\hbar^2\beta}\right)\sqrt{\frac{\hbar^2\beta}{m_s 8\pi}}\sqrt{\frac{\pi\hbar^2\beta}{2m_s}} \\
=& 1
\end{aligned} \tag{3.9}$$

In contrast, one can consider the case of a parabolic barrier along the reaction coordinate. This approximation is suitable for the shallow tunneling regime, since any barrier near the top can be approximated by a parabola. In this case the Hamiltonian is $\hat{H}_s = \frac{\hat{p}^2}{2m_s} - \frac{1}{2}m_s\omega^2 s^2$ and

$$\langle s|e^{-\beta\hat{H}_s}|-s\rangle = \sqrt{\frac{m_s\omega}{2\pi\hbar\sin(\hbar\omega\beta)}}\quad \exp\left[-\frac{m_s\omega}{\hbar}\cot\left(\frac{\hbar\omega\beta}{2}\right)s^2\right] \tag{3.10}$$

Inserting this result into 3.6 the tunneling correction is

$$\begin{aligned}
\Gamma_{pb} =& \frac{\hbar^2\beta}{2m_s}\int_{-\infty}^{+\infty} ds\left(-\frac{1}{s}\right)\frac{\partial}{\partial s}\sqrt{\frac{m_s\omega}{2\pi\hbar\sin\left(\hbar\omega\beta\right)}}\exp\left[-\frac{m_s\omega}{\hbar}\cot\left(\frac{\hbar\omega\beta}{2}\right)s^2\right] \\
=& \frac{\hbar^2\beta}{2m_s}\sqrt{\frac{m_s\omega}{h\sin\left(\hbar\omega\beta\right)}}\int_{-\infty}^{+\infty} ds\left(-\frac{1}{s}\right)\frac{\partial}{\partial s}\exp\left[-\frac{m_s\omega}{\hbar}\cot\left(\frac{\hbar\omega\beta}{2}\right)s^2\right] \\
=& \frac{\hbar^2\beta}{2m_s}\sqrt{\frac{m_s\omega}{h\sin\left(\hbar\omega\beta\right)}}\left[\frac{2m_s\omega}{\hbar}\cot\left(\frac{\hbar\omega\beta}{2}\right)\right]\int_{-\infty}^{+\infty} ds\exp\left[-\frac{m_s\omega}{\hbar}\cot\left(\frac{\hbar\omega\beta}{2}\right)s^2\right] \\
=& \frac{\hbar^2\beta}{2m_s}\sqrt{\frac{m_s\omega}{h\sin\left(\hbar\omega\beta\right)}}\left[\frac{2m_s\omega}{\hbar}\cot\left(\frac{\hbar\omega\beta}{2}\right)\right]\sqrt{\frac{\pi\hbar}{m_s\omega\cot\left(\frac{\hbar\omega\beta}{2}\right)}} \\
=& \hbar\beta\sqrt{\frac{1}{2\sin\left(\hbar\omega\beta\right)}}\left[\omega\cot\left(\frac{\hbar\omega\beta}{2}\right)\right]\sqrt{\frac{1}{\cot\left(\frac{\hbar\omega\beta}{2}\right)}} \\
=& \hbar\omega\beta\sqrt{\frac{\cot\left(\frac{\hbar\omega\beta}{2}\right)}{4\sin\left(\frac{\hbar\omega\beta}{2}\right)\cos\left(\frac{\hbar\omega\beta}{2}\right)}} \\
=& \frac{\frac{1}{2}\hbar\omega\beta}{\sin\left(\frac{\hbar\omega\beta}{2}\right)}
\end{aligned} \tag{3.11}$$

This last result demonstrates that the QTST formula in equation 3.5 regains the well known TST Wigner tunneling correction.[47, 52]

3.2 Semiclassical Instanton rate approximation

In the previous section it has been demonstrated that assuming the separability of the coordinates at the saddle point for equation 3.5 leads to the usual quantum corrected TST expression. In this section a method that allows to evaluate the expression 3.5 in the general non-separable case is presented. The operators in equation 3.5 could be represented in a discrete basis, but this would require a numerical matrix diagonalization that is generally too computationally expensive. A semiclassical strategy to deal with the problem is known as the Semiclassical Instanton (SCI). The detailed derivation of this approach is the subject of a pivotal paper by Miller,[140] while a brief summary of it is reported in the following.

The starting point is the description of an N dimensional system by means of a set of positions and momenta described by the vectors $\boldsymbol{q}=(q_1, q_2, ..., q_N)$

and $\boldsymbol{p}$=$(p_1, p_2, ..., p_N)$. The reaction coordinate is associated to the phase space variables q_1 and p_1. Instead of making use of the Weyl rule, the quantum mechanical trace in equation 3.1 can be replaced by an average over the classical phase space

$$k(T) = \frac{1}{Q_r} \int d\boldsymbol{q} \int d\boldsymbol{p} W(\boldsymbol{p}, \boldsymbol{q}) \, \delta(q_1) \left(\frac{p_1}{m}\right) h(p_1) \tag{3.12}$$

by using the Wigner transform of the Boltzmann operator

$$W(\boldsymbol{p}, \boldsymbol{q}) = \frac{1}{h^N} \int d\boldsymbol{q'} e^{-i\frac{\boldsymbol{p}\cdot\boldsymbol{q'}}{\hbar}} \langle \boldsymbol{q} + \frac{1}{2}\boldsymbol{q'} | e^{-\beta\hat{H}} | \boldsymbol{q} - \frac{1}{2}\boldsymbol{q'} \rangle \tag{3.13}$$

To analytically evaluate expression 3.12, one can consider the semiclassical representation of the Boltzmann operator, that is obtained as the analytic continuation of the semiclassical time propagator

$$\langle \boldsymbol{q_f} | e^{-\beta\hat{H}} | \boldsymbol{q_i} \rangle_{SC} = \left(\frac{1}{2\pi i\hbar}\right)^{\frac{N}{2}} \left(\left|\frac{\partial \boldsymbol{q_f}}{\partial \boldsymbol{p_i}}\right|\right)^{-\frac{1}{2}} \exp\left[\frac{i}{\hbar} S(\boldsymbol{q_f}, \boldsymbol{q_i})\right] \tag{3.14}$$

where $S(\boldsymbol{q_f}, \boldsymbol{q_i})$ is the classical action associated to the classical trajectory that starts with momentum $\mathbf{p}_i$ from position $\mathbf{q}_i$ at time t = 0 and ends at position $\mathbf{q}_f$ at t = -i$\hbar\beta$. By inserting equation 3.14 in expression 3.12, and after the variable change

$$\begin{cases} \boldsymbol{q} + \frac{1}{2}\boldsymbol{q'} = \boldsymbol{q_f} \\ \boldsymbol{q} - \frac{1}{2}\boldsymbol{q'} = \boldsymbol{q_i} \end{cases} \rightarrow \begin{cases} \boldsymbol{q'} = \boldsymbol{q_f} - \boldsymbol{q_i} \\ \boldsymbol{q} = \frac{1}{2}(\boldsymbol{q_f} + \boldsymbol{q_i}) \end{cases} \tag{3.15}$$

the following formula is obtained

$$\begin{aligned} k(T) = & \frac{1}{Q_r} \left(\frac{1}{h^N}\right) \left(\frac{1}{2\pi i\hbar}\right)^{\frac{N}{2}} \times \\ & \int d\boldsymbol{p} \int d\boldsymbol{q_i} \int d\boldsymbol{q_f} \delta\left(\frac{q_{f,1} + q_{i,1}}{2}\right) \left(\frac{p_1}{m}\right) h(p_1) \left(\left|\frac{\partial \boldsymbol{q_f}}{\partial \boldsymbol{p_i}}\right|\right)^{-\frac{1}{2}} \times \\ & \exp\left\{-\frac{i}{\hbar}\left[S(\boldsymbol{q_f}, \boldsymbol{q_i}) - \boldsymbol{p}\cdot(\boldsymbol{q_f} - \boldsymbol{q_i})\right]\right\} \end{aligned} \tag{3.16}$$

The integrals over $\mathbf{p}$ and $\mathbf{q}_f$ in expression 3.16 can be evaluated via the stationary phase approximation (see appendix 2.7). For the integration over $\mathbf{p}$ the stationary

phase prescription implies

$$\frac{\partial}{\partial \boldsymbol{p}}\left[S\left(\boldsymbol{q}_f,\boldsymbol{q}_i\right)-\boldsymbol{p}\cdot\left(\boldsymbol{q}_f-\boldsymbol{q}_i\right)\right]=0\Rightarrow \boldsymbol{q}_f=\boldsymbol{q}_i \tag{3.17}$$

while for the integration in $\mathbf{q}_f$ it gives

$$\frac{\partial}{\partial \boldsymbol{q}_f}\left[S\left(\boldsymbol{q}_f,\boldsymbol{q}_i\right)-\boldsymbol{p}\cdot\left(\boldsymbol{q}_f-\boldsymbol{q}_i\right)\right]=0\Rightarrow \boldsymbol{p}_f=\boldsymbol{p} \tag{3.18}$$

where $\mathbf{p}_f$ is the momentum at position $\mathbf{q}_f$. After the two stationary phase approximations are carried out, only the integral over q_i is left. This surviving integral can be rearranged by expanding the N components of the vector q_i

$$k\left(T\right)=\frac{1}{Q_r}\int dq_{i,1}\delta\left(q_{i,1}\right)\int dq_{i,2}\int dq_{i,3}...\int dq_{i,N}\frac{1}{2}\left|\dot{q}_{i,1}\right|\left\langle \boldsymbol{q_i}\right|e^{-\beta\hat{H}}\left|\boldsymbol{q_i}\right\rangle \tag{3.19}$$

Again the stationary phase approximation can be applied, whose condition implies

$$\frac{\partial}{\partial \boldsymbol{q_i}}\left[S\left(\boldsymbol{q_i},\boldsymbol{q_i}\right)\right]=0\Rightarrow \boldsymbol{p}_f=\boldsymbol{p_i} \tag{3.20}$$

Conditions 3.17, 3.20 mean that periodic trajectories (on the upside down potential energy surface) give the main contribution to the integral 3.16. However, since the integration over variable $q_{i,1}$ can be easily achieved exploiting the delta function $\delta\left(q_{i,1}\right)$, the stationary phase approximation is done only for the N - 1 remaining integrations over $q_{i,2}$, $q_{i,3}$, ..., $q_{i,N}$. It can be shown that integration over the latter set of variables gives the result (for further detail see reference [140])

$$\begin{aligned}&\int dq_{i,2}\int dq_{i,3}...\int dq_{i,N}\left\langle \boldsymbol{q_i}\right|e^{-\beta\hat{H}}\left|\boldsymbol{q_i}\right\rangle=\\&\frac{1}{2\pi\hbar}\int dEe^{-\beta E}\frac{1}{\left|\dot{q}_{i,1}\right|}\sum_{k=1}^{\infty}\left(-1\right)^{k-1}e^{\frac{ikS}{\hbar}}\prod_{j=1}^{N-1}\frac{1}{2\sinh\left[\frac{ku_j(E)}{2}\right]}\end{aligned} \tag{3.21}$$

Finally, integrating over the last $q_{i,1}$ variable, the final expression for the rate constant is

$$k_{SCI}\left(T\right)=\frac{1}{Q_r}\frac{1}{h}\int dEe^{-\beta E}N\left(E\right) \tag{3.22}$$

with

$$N\left(E\right)=\sum_{k=1}^{\infty}\left(-1\right)^{k-1}e^{\frac{ikS(E)}{\hbar}}\prod_{j=1}^{N-1}\left\{2\sinh\left[\frac{ku_j\left(E\right)}{2}\right]\right\}^{-1} \tag{3.23}$$

Comparing this result with the exact rate expression that was derived from scattering theory 2.31, it is clear that $N(E)$ is a semiclassical approximation for the cumulative reaction probability (CRP).

In the expressions 3.21 and 3.23 u_j are the stability parameters of the periodic trajectory. Given the monodromy matrix

$$M = \begin{pmatrix} \frac{\partial q_f(q_i,p_i)}{\partial q_i} & \frac{\partial q_f(q_i,p_i)}{\partial p_i} \\ \frac{\partial p_f(q_i,p_i)}{\partial q_i} & \frac{\partial p_f(q_i,p_i)}{\partial p_i} \end{pmatrix} \tag{3.24}$$

associated to the motion along the periodic trajectory, its eigenvalues are $e^{\pm u_j}$, with j=1,2,..,N. In the separable case, for the harmonic motion, $u_j = \hbar\omega_j\beta$, where ω_j are the vibrational frequencies of the transition state (see Appendix 3.3). Therefore, the product in equation 3.23 can be seen as a generalization to the non separable case of the vibrational partition function at the transition state. In fact, this factor contains N - 1 generalized frequencies, because the imaginary one is considered apart. Moreover, the exponent in equation 3.23 can be seen as a multidimensional generalization of the WKB penetration integral (θ) through a one dimensional potential energy barrier,[136] i.e.

$$\frac{iS(E)}{\hbar} = -2\theta(E). \tag{3.25}$$

Equations 3.22 and 3.23 constitute a non separable semiclassical transition state formulation, which takes into account only the states of the activated complex, but does not imply the selection of a specific reaction path. A more useful form of equation 3.23 can be obtained by expanding in a geometric series each sinh term in the product as

$$\left\{2\sinh\left[\frac{ku_j(E)}{2}\right]\right\}^{-1} = \sum_{n_j}^{\infty}\exp\left[-k\left(n_j + \frac{1}{2}\right)u_j(E)\right] \tag{3.26}$$

where j = 1, 2, ..., N - 1.With this substitution and after reordering the sums in equation 3.23, the one over k becomes a convergent binomial series of the type

$\sum_{k=0}^{\infty}(-1)^k x^k = \frac{1}{1+x}$. The CRP can be then evaluated as

$$\begin{aligned} N(E) &= \sum_{n_1=0}^{\infty}\sum_{n_2=0}^{\infty}\ldots\sum_{n_{N-1}=0}^{\infty}\sum_{k=1}^{\infty}(-1)^{k-1}e^{-2k\theta(E)}\exp\left[-k\left(n_j+\frac{1}{2}\right)u_j(E)\right] \\ &= -\sum_{n_1=0}^{\infty}\sum_{n_2=0}^{\infty}\ldots\sum_{n_{N-1}=0}^{\infty}\sum_{k=1}^{\infty}(-1)^k\left\{\exp\left[-2\theta(E)-\left(n_j+\frac{1}{2}\right)u_j(E)\right]\right\}^k \\ &= \sum_{n_1=0}^{\infty}\sum_{n_2=0}^{\infty}\ldots\sum_{n_{N-1}=0}^{\infty}-\left\{1+\exp\left[-2\theta(E)-\left(n_j+\frac{1}{2}\right)u_j(E)\right]\right\}^{-1} \\ &= \sum_{n_1=0}^{\infty}\sum_{n_2=0}^{\infty}\ldots\sum_{n_{N-1}=0}^{\infty}\left\{1+\exp\left[2\theta(E)+\sum_{j=1}^{N-1}\left(n_j+\frac{1}{2}\right)u_j(E)\right]\right\}^{-1} \end{aligned} \tag{3.27}$$

Equation 3.27 is easy to evaluate in the separable case. In fact, the stability parameters can be related to the frequencies of vibration through the period ($\tau(E)$) of the SCI periodic trajectory, i.e. $u_j(E) = \omega_j\tau(E) = -2\theta'(E)\hbar\omega_j$,[140] where in the r.h.s. the energy derivative of the action along the periodic trajectory and equation 3.25 have been employed. Equation 3.27 becomes

$$\begin{aligned} N^{\mathrm{SEP}}(E) =& \sum_{n_1=0}^{\infty}\sum_{n_2=0}^{\infty}\ldots\sum_{n_{N-1}=0}^{\infty}\left\{1+\exp\left[2\theta(E)-2\theta'(E)\sum_{j=1}^{N-1}\left(n_j+\frac{1}{2}\right)\hbar\omega_j(E)\right]\right\}^{-1} \\ =& \sum_{n_1=0}^{\infty}\sum_{n_2=0}^{\infty}\ldots\sum_{n_{N-1}=0}^{\infty}\left\{1+\exp\left[2\theta(E)-2\theta'(E)(E-E_n)\right]\right\}^{-1} \\ \simeq& \sum_{n_1=0}^{\infty}\sum_{n_2=0}^{\infty}\ldots\sum_{n_{N-1}=0}^{\infty}\left\{1+\exp\left[2\theta(E_n)\right]\right\}^{-1} \end{aligned} \tag{3.28}$$

E_n is the amount of energy that is associated to the translation along the reaction coordinate. Therefore, in the separable case, the probability of reaction is the sum of the WKB one dimensional tunneling probability for all accessible states.[38]

3.3 Semiclassical Transition State Theory

The explicit evaluation of equation 3.27 in the general non-separable case is problematic. The main difficulty consists in the computation of the penetration integral $\theta(E)$ and of the stability parameters $u_j(E)$. The same analytical form for the CRP as the one previously found in the separable case is also valid in the general instance of a non-separable Hamiltonian if "good" action-angle variables

for the transition state are constructed.[141] Therefore, for the reactive mode, by means of the Bohr Sommerfeld quantization rule the following equality holds

$$\left(n_N + \frac{1}{2}\right) = \frac{i\theta}{\pi} \tag{3.29}$$

Equation 3.29 allows to write the energy as a function of the penetration integral, i.e. E(n_1,...,n_{N-1}, θ). If one succeeds in inverting this relation to get $\theta(E)$, then the CRP is readily calculated

$$N(E) = \sum_{n_1=0}^{\infty} \sum_{n_2=0}^{\infty} ... \sum_{n_{N-1}=0}^{\infty} \{1 + \exp[2\theta(E)]\}^{-1} \tag{3.30}$$

The difference between equation 3.30 and the corresponding one for the separable case 3.28 is that the penetration integral is now a function of the total energy and no longer only of the translational energy in the reactive mode as before.

Hernandez and Miller provided a solution to the inversion problem, by means of their Semiclassical Transition State Theory (SCTST).[39] The starting point of their strategy is the standard perturbative expression for the vibrational levels of a molecule with N vibrational degrees of freedom. For a stable configuration which corresponds to a minimum on the potential energy surface, if the total angular momentum is J = 0, then the total vibrational energy can be evaluated as

$$E(n_1, n_2...n_N) = V_0 + \sum_{j=1}^{N} \hbar\omega_j \left(n_j + \frac{1}{2}\right) + \sum_{j \leq j'=1}^{N} x_{jj'} \left(n_j + \frac{1}{2}\right)\left(n_j + \frac{1}{2}\right) \tag{3.31}$$

where V_0 is the potential value at the bottom of the well, ω_j are the normal modes frequencies that are computed by diagonalizing the Hessian at the equilibrium geometry, and $x_{jj'}$ are the elements of the anharmonicity matrix that are computed from cubic and some of the quartic force constants. The expansion is stopped at the second order, which is usually sufficient for the purpose of computing SCTST rates.[142] Calculation of the anharmonicity matrix is the core of Second Order Vibrational Perturbation Theory (VPT2) that nowadays is routinely implemented in many quantum chemistry programs.[143, 144, 145]

Equation 3.31 can be also generalized to the case of a molecular configuration that corresponds to a saddle point on the potential energy surface, i.e. a transition state. In this case if the N-th degree of freedom corresponds to the imaginary

frequency, then for that mode the following imaginary quantities can be defined

$$\begin{aligned} \omega_N &= i\left|\omega_N\right| \\ x_{jN} &= -i\left|x_{jN}\right|, j = 1, 2..., N \end{aligned} \tag{3.32}$$

In this way the equation E = E(n_1,...,n_{N-1},θ) is a quadratic expression in θ. It can be easily inverted to obtain the following generalized barrier penetration integral

$$\begin{aligned} \theta\left(n_1, ..., n_{N-1}, E\right) =& \frac{\pi\Delta E}{\hbar\Omega_N} \frac{2}{1+\sqrt{1+\frac{4x_{NN}\Delta E}{\left(\hbar\Omega_N\right)^2}}} \\ \Delta E =& V_0 - \left[E - \sum_{j=1}^{N-1} \hbar\omega_j \left(n_j + \frac{1}{2}\right) - \sum_{j\leq j'=1}^{N-1} x_{jj'} \left(n_j + \frac{1}{2}\right)\left(n_j + \frac{1}{2}\right)\right] \\ \hbar\Omega_N =& \hbar\left|\omega_N\right| - \sum_{j=1}^{N-1} \left|x_{jN}\right| \left(n_j + \frac{1}{2}\right) \end{aligned} \tag{3.33}$$

In the previous equations, V_0 is the potential at the saddle point, while the term in squared brackets is the amount of energy that remains in the reactive mode characterized by the imaginary frequency. When the energy associated to the reaction coordinate is very close to the value V_0, ΔE is small. In this limit, the penetration integral 3.33 becomes

$$\theta\left(n_1, ..., n_{N-1}, E\right) \approx \frac{\pi\Delta E}{\hbar\Omega_N} - \pi\frac{x_{NN}\Delta E^2}{\left(\hbar\Omega_N\right)^3} + ... \tag{3.34}$$

The leading term of this expression recalls the one dimensional penetration integral of a parabolic barrier. In fact, in this limit the barrier top is the important part of the potential, and the parabolic approximation is a good one. However, the first term in equation 3.34 also accounts for the couplings with all the others degrees of freedom via the effective frequency Ω_N. More specifically, from the expression of Ω_N in 3.33, it is evident that if the coupling of the reaction coordinate with the other modes is positive ($\left|x_{jN}\right|$>0) then $\theta\left(E\right)$ increases. The magnitude of the second term in equation 3.34 depends on the x_{NN} anharmonic coupling. From VPT2 this quantity is given by

$$x_{NN} = \frac{h^2}{16\left|\omega_N\right|^2}\left[-f_{NNNN} - \frac{5}{3}\frac{f_{NNN}^2}{\left|\omega_N\right|^2} + \sum_{l=1}^{N-1}\frac{f_{NNl}^2}{\omega_l^2}\frac{\left(8\omega_N^2 + 3\omega_l^2\right)}{\left(4\left|\omega_N\right|^2 + 3\omega_l^2\right)}\right] \tag{3.35}$$

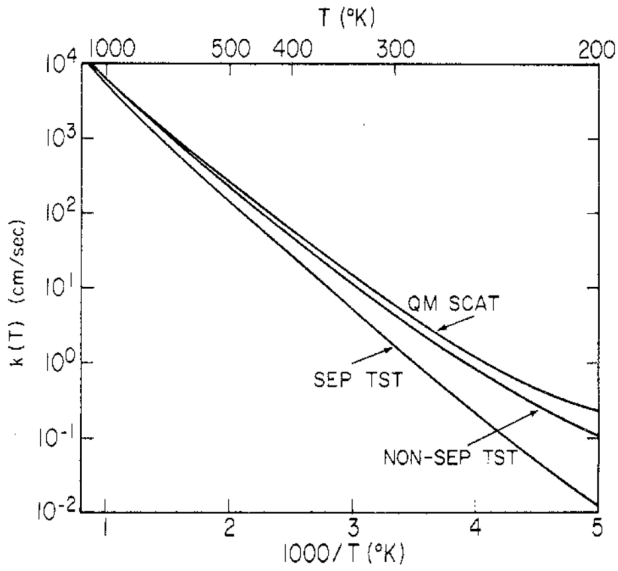

Figure 3.2: The picture shows a comparison of the exact quantum mechanical rate constant obtained from scattering calculations (QM SCAT), the semiclassical transition state theory of expression 3.22 (NON-SEP TST), and the conventional separable transition state theory with the Wigner tunneling correction (SEP TST) for the H + H_2 reaction. Equation 3.22 gives a much better estimate of the rate constant, which underestimates the exact result by 25% at 200K. The conventional transitions state theory is wrong by more than a order of magnitude at the same temperature. Figure from reference [147].

where the elements with three indexes are cubic force constants, and the one with four indexes is a quartic force constant. In this expression the two negative contributions depend on the anharmonicity due to the N-th mode only. As a consequence, the more anharmonic the motion along the reaction coordinate, the bigger $\theta(E)$, and the smaller the cumulative reaction probability $N(E)$. The positive contribution to x_{NN} comes from the third term in equation 3.35, that is the coupling of the reaction coordinate with the other modes. A large and positive x_{NN} decreases the value of $\theta(E)$. This means that the coupling of the reaction coordinate with other modes leads to a higher cumulative reaction probability. This qualitative analysis makes it evident that SCTST is indeed a non-separable and quantum corrected TST.[39] Figure 3.2 illustrates the importance of the non separability even in the case of the two-dimensional H + H_2 and the success of the SCTST in this application.[146, 147]

Unfortunately, even if the previous derivation has demonstrated how to compute $\theta(E)$, there is yet another hindrance to the evaluation of the SCTST version of equation 3.22. In fact, it is numerically very hard to evaluate the nested sums in equation 3.30, especially as the number of degrees of freedom and accessible states to deal with becomes larger and larger. In the next chapter we provide an efficient strategy to afford this computation, which makes SCTST doable even for systems with more than 100 internal degrees of freedom.

Appendix 3.A: Stability Parameters for the Harmonic Oscillator 1D

The analytic solution for the classical equations of motion for the classical harmonic oscillator Hamiltonian $\mathcal{H} = \frac{p^2}{2m} + \frac{1}{2}m\omega^2$ are

$$\begin{cases} q_f(p_i, q_i) = q_i \cos(\omega t) + \frac{p_i}{m\omega} \sin(\omega t) \\ p_f(p_i, q_i) = -m\omega q_i \sin(\omega t) + p_i \cos(\omega t) \end{cases} \tag{3.36}$$

where the subscript f indicates the final value of the variable, i.e. after an evolution time t, while the subscript i is for the initial t=0 value. The monodromy matrix 3.24 in this case reads

$$M_{1D-HO} = \begin{pmatrix} \cos(\omega t) & \frac{\sin(\omega t)}{m\omega} \\ -m\omega \sin(\omega t) & \cos(\omega t) \end{pmatrix} \tag{3.37}$$

Its eigenvalues are $e^{\pm i\omega t}$, therefore the stability parameters defined in section 3.2 are u=iωt. By going back to the imaginary time domain, with the substitution t=-i$\hbar\beta$, one obtains u=$\hbar\omega\beta$.

4 An Efficient Computational Approach for the Calculation of the Vibrational Density of States[1]

In this chapter, we present an optimized approach for the calculation of the vibrational density of states in high dimensional systems. This task is of paramount importance, since partition functions and several thermodynamic properties can be accurately estimated once the density of states is known. A new code, called ParADenSum, based on the implementation of the Wang-Landau Monte Carlo algorithm for parallel architectures is described and applied to real complex systems. Moreover, we show how to extend this code for the computation of effective vibrational density of states for transition state structures. Once this quantity is known, the SCTST rate constant is readily evaluated. This extension has been implemented in the ParSCTST code. We test the accuracy of our implementations on several molecular systems, including some benchmarks for which an exact evaluation of the vibrational density of states is doable by direct counting. In addition, we find a significant computational speed-up with respect to standard approaches when applying our code to molecules up to 66 degrees of freedom. The new code can easily handle 150 degrees of freedom. These features make ParADenSum and ParSCTST very promising tools for future calculations of thermodynamic properties and thermal rate constants of complex systems.

4.1 Introduction

The vibrational density of states of a chemical system is the number of vibrational states per unit of energy. This quantity is of paramount importance in molecular and chemical physics. All information about energetics, thermodynamics at equilibrium, as well as molecular spectroscopy can be obtained from the knowledge

[1]This chapter is the reproduction with some minor changes of the paper **Chiara Aieta**, Fabio Gabas, and Michele Ceotto, "An Efficient Computational Approach for the Calculation of the Vibrational Density of States" *J. Phys. Chem. A* **120**, 4853 (2016).

of the density of states ρ (E). More specifically, the vibrational density of states yields the vibrational partition function upon Laplace transform

$$Q_{vib}(\beta) = \int \rho_{vib}(E)\, \mathrm{e}^{-\beta E} dE \tag{4.1}$$

where β=1/k_BT, k_B being the Boltzmann constant and T the temperature of the system. $Q_{vib}(\beta)$ is used not only to compute specific heats but also thermal rate constants. More generally, statistical kinetic theories of dynamical processes, such as energy transfer and reactivity,[148, 149, 150, 151, 152, 119] employ the density of states in their formulation.

Unfortunately, quantum densities of states can be calculated exactly by direct counting of quantum states only for low dimensional systems or can be obtained only for a restricted number of separable systems. When the BS algorithm is combined with the Stein Rabinovitch (SR) one, the combination of the two (BSSR) enables very fast calculations for separable models of high dimensional systems.[153, 154] Such models may include not only harmonic degrees of freedom (consisting of uncoupled harmonic oscillators), but also highly anharmonic ones, such as Morse oscillators or hindered internal rotations. An alternative route consists in inverting eq. 4.1 and calculate ρ_{vib} (E) as the Inverse Laplace Transform (ILT) of the canonical partition function. Clearly, this approach is advantageous when the partition function can be determined via computationally affordable Monte Carlo methods. Below, we will test the ILT approach and show that its successful application is limited in dimensionality and in energy range, as already pointed out elsewhere.[155] A more widely used method is based on Steepest Descents approximation.[156, 157]Nevertheless, ILT is a viable tool, which has already been employed in several cases to estimate microcanonical densities of states.[158, 159, 160, 116] Other more manageable (but approximated) approaches have been developed in the past. For example, in the so called Simple Perturbation Theory (SPT) of Isaacson et al.[161, 162] an effective harmonic frequency for each mode is defined as

$$\overline{\nu}_i = \nu_i + 2x_{ii} + \frac{1}{2}\sum_{j\neq i} x_{ij} \tag{4.2}$$

where ν_i is the harmonic frequency of the i-th mode, and x_{ij} is the i, j element of the matrix of anharmonic couplings. SPT approximates ρ_{vib} (E) as that of a set of uncoupled harmonic oscillators of frequencies provided by eq. 4.2.

In general, to calculate ρ_{vib} (E) directly and with high accuracy for large systems is a difficult task. The challenge ahead of us is to include not only anhar-

monicities, but also intermode couplings and quantum effects in the calculation of $\rho_{vib}(\mathrm{E})$. This goal can be reached, at least in part, by using a perturbative approach, where the energy of the quantized vibrational levels is expanded around a stationary point up to the second order, including the anharmonic coupling terms as follows

$$E = \sum_{i=1}^{nvib} \omega_i \left(v_i + \frac{1}{2} \right) + \sum_{i,j=1}^{nvib} x_{ij} \left(v_i + \frac{1}{2} \right) \left(v_j + \frac{1}{2} \right) \tag{4.3}$$

where E is the vibrational energy, nvib is the number of vibrational degrees of freedom, ω_i is the i-th element of the vector ω of harmonic frequencies, v_i is the vibrational quantum number of the i-th mode, and x_{ij} is the i, j element of the x-matrix of anharmonic couplings. In principle, adoption of eq. 4.3 would permit the calculation of $\rho_{vib}(\mathrm{E})$ via Monte Carlo sampling.[163, 164, 165, 166] However, a straightforward application of the Monte Carlo approach is hindered by a drastic increase of the variance with the number of degrees of freedom.[165, 166] As an alternative, Basire et al.[167] first, and Nguyen and Barker[168] later, showed that the Wang-Landau (WL) method,[169, 170] in which Monte Carlo walker visits are driven by the criterion of uniform histogram of visits, can successfully be applied to calculate not only classical but also quantum $\rho_{vib}(\mathrm{E})$. In particular, Barker et al.[40] implemented the WL approach for $\rho_{vib}(\mathrm{E})$ calculations in the code ADenSum of the MultiWell suite. This program suite can also solve the internal energy master equation for complex unimolecular reactions systems, calculate exact $\rho_{vib}(\mathrm{E})$ (DoLoops code) and approximate ones using the BSSR algorithm (code DenSum), and estimate thermal rate constants and other thermodynamic quantities.[41]

Quite recently, there has been a significant boost in the WL application provided by its parallelization.[171, 172, 173, 174, 175, 176, 177] Vogel et al.[171] showed how the WL algorithm can be systematically implemented for application to large dimensional problems. Their parallelization idea is based on the splitting of the total energy range into smaller windows with large overlaps between adjacent windows. Multiple independent walkers are sampled in each energy window, and replica exchanges between walkers across overlapping windows are allowed. There is no *a priori* limit on the number of windows, and this parallel WL scheme can scale up to thousands of CPUs. We find this hierarchical parallel framework potentially advantageous for vibrational density of states calculations.

4.2 The Algorithm ParADenSum

The quantum molecular density of vibrational states ρ_{vib} (E) is rigorously obtained by counting the vibrational eigenstates N_{vib} (E) per energy interval ΔE within the interval $[E,\ E+\Delta E]$, i.e.

$$\rho_{vib}(E) = N_{vib}(E)/\Delta E. \tag{4.4}$$

To perform the counting, the exact vibrational eigenvalues should be known in advance. When eigenvalues are calculated with grid methods, such as Discrete Variable Representation methods,[178, 179, 180] the complexity of the system is usually confined to a few atoms. For higher dimensional systems, one can either rely on semiclassical approximations [181, 182, 183, 184, 91, 185, 186, 90, 187, 188] or perturbation expansions around the molecular minimum geometry.[189]

The perturbation approach approximates the vibrational energy with the well known Dunham expansion.[163, 164] Here, nvib normal modes are coupled to each other and quantum effects are included by the quantum numbers v=$(v_1, v_2, ..., v_i, ..., v_{nvib})$. Since the first occupied quantum state is at the zero point energy value (E_{ZPE}), a convenient expression for the vibrational energy relative to the zero-point one (E') can be derived from eq. 4.3

$$E' = E - E_{ZPE} = \sum_{i=1}^{nvib} \omega_i \left(v_i + \frac{1}{2}\right) + \sum_{i,j=1}^{nvib} x_{ij} \left(v_i + \frac{1}{2}\right)\left(v_j + \frac{1}{2}\right) - E_{ZPE}. \tag{4.5}$$

Harmonic frequencies and the x-matrix have to be supplied as input and can be computed with quantum chemistry codes (see, for instance, Ref.[145, 143]). All combinations of vibrational quantum numbers v providing bounded states, i.e. with energy in between the ZPE and the dissociation energy, are counted. However, eq.(4.5) is not accurate near the dissociation threshold or above. The number of states N_{vib} (E) for each interval of vibrational energies between E and E + ΔE will provide the density of states ρ_{vib} (E) according to eq. 4.4.

The DoLoops code in MultiWell is based on a direct counting of the number of vibrational states N_{vib} (E) by using as many nested do cycles on the vibrational quantum numbers as the number of degrees of freedom. The algorithm is useful for small-size systems (up to 4 atoms), while, for larger systems, the computational overhead quickly becomes unaffordable. For this reason, Basire et al.[167] first, and Nguyen and Barker later,[168] implemented the calculation of ρ_{vib} (E) within a Wang Landau Monte Carlo scheme.[169, 170] The algorithm is based upon the observation that the histogram of visits H(E) will be flat when

the probability of visiting each energy level for a random walk in the space of the quantum numbers is proportional to $1/\rho_{vib}\,(\mathrm{E})$. In this way, the random walk is forced to visit regions with low density of states and is not trapped in high density zones. The Wang Landau algorithm is rigorously proven to converge,[190] and it has been shown to be even suitable for building the density of states of rough energy landscapes.[169, 170] In the WL scheme, after a starting guess $\rho_{vib}\,(\mathrm{E})$=1, random walks are performed in energy space. The energy range spanning from $\mathrm{E_{min}}$ to E_{max} is discretized in intervals of fixed width ΔE named bins. with an acceptance probability p from a vibrational state with energy $\mathrm{E'}_i$ to another at $\mathrm{E'}_f$ is given by

$$p\left(\mathrm{E'}_i \rightarrow \mathrm{E'}_f\right) = \min\left(\frac{\rho_{vib}\left(\mathrm{E'}_i\right)}{\rho_{vib}\left(\mathrm{E'}_f\right)}, 1\right). \tag{4.6}$$

Once the step is accepted, it is determined to which bin the energy $\mathrm{E'}_f$ belongs, and $\rho_{vib}\,(\mathrm{E}_i)$ is multiplied by the modification factor f. Initially, f_0=e. During each random walk, the histogram H(E) of visits of each energy level is updated together with $\rho_{vib}\,(\mathrm{E})$. The procedure halts when the flatness of H(E) is within a cutoff value. Once the flatness criterion for the j-th iteration is satisfied, the modification factor is reduced using a monotonically decreasing function of the type f_{j+1}=$\sqrt{f_j}$, and a new random walk begins starting from the last estimate of the density of states $\rho_{vib,j}\,(\mathrm{E})$. A sort of WL rule of thumb[169, 170, 171] is to take the whole algorithm completed after 21 such iterations, since, after that, the modification factor has reached a value really close to 1 and the density of states does not change anymore when it is updated in the limit of numerical precision used in molecular system calculations. The main advantage of the WL algorithm is that it can be employed for the calculation of the density of states of any system.[191] Regarding the problem of calculating the density of vibrational states of a molecule, $\rho_{vib}\,(\mathrm{E})$ is normalized by setting the width of the first energy bin to contain only the vibrational ground state.

The ADenSum code of the MultiWell suite[40, 41] represents the state of the art for molecular density of states calculations. Each quantum number v_k of the k-th degree of freedom has an upper limit provided by the equation $\partial \mathrm{E'}/\partial v_k$=0, which enforces the system to be bound along the k-th degree of freedom.[168] Vibrational modes associated to hindered rotations are convoluted as rotations in the vibrational states count. Nguyen et al.[168] also tested the possible expression of the transition probability of eq. 4.6 and they finally set p=MIN$(1/N, 0.25)$, since the result standard deviation is quite stable with respect to the choice of p. The critical issues of the ADenSum code are that the number of random

walkers over the entire energy space is restricted to a single one and that there is no flatness requirements over the histogram, since the total number of Monte Carlo iterations are fixed either at 10^2, 10^3, 10^4, or 10^5 times the energy bin number.[168] This implementation was sufficient to deal with reactive systems with small number of atoms, like the ones relevant for atmospheric or combustion chemistry, but it was not adequate for higher dimensional systems such as the ones encountered in organic synthesis.

To overcome the limitations of the MultiWell ADenSum code, we have modified its algorithm structure and then we have implemented it for parallel architectures by using the MPI (Message Passing Interface) API. The code structure does not allow for a straightforward parallelization, since the outer *do cycle* is the evaluation of $\rho_{vib}\,(\mathrm{E})$, with the j-th iteration starting from the converged $\rho_{vib,j-1}\,(\mathrm{E})$ value of the (j-1)-th iteration. Instead, the parallelization strategy we employ is to divide the energy range into windows and set the calculations of $\rho_{vib}\,(\mathrm{E})$ for each window on a single processor. This strategy is dictated by the observation that less random sampling events and reduced computational effort is needed for Monte Carlo convergence in a restricted energy range. The number of processors is given by the choice of windowing. Since the WL density of states is notoriously biased at the edges of small energy windows,[171] we always keep a percentage of overlap between neighbor windows. We call the new code ParADenSum and its structure is sketched in picture 4.1. The code supports the possibility to run multiple walkers for each energy window. The new algorithm starts with a preliminary single walk that is performed on the entire energy range to pick up the initial configurations of each walker in each window. Given the uniformly distributed probability in energy space, this single walk is quite efficient in providing initial quantum numbers configurations. After choosing the starting configuration in each window as described above, unique random number generator seeds are created from the processor ID for each task and random walks start. In the ADenSum code f is updated after a fixed number of Monte Carlo sweeps. Instead, in ParADenSum the WL flatness criterion is applied and monitored separately for each window. In case of multiple walkers, they average out their estimate of $\rho_{vib}\,(\mathrm{E})$ before the update of the modification factor f and the beginning of a new iteration. This set up makes ParADenSum quite flexible and able to fit the energy domain better than the ADenSum code. As a general strategy to better handle the data in this parallelization scheme, we set arrays of dimensionality equal to the number of windows. $\rho_{vib}\,(\mathrm{E})$ and $\mathrm{H(E)}$ are represented as three dimensional arrays where the indexes define the number of grains per window, the number of walkers per window and, a third index, the window number. In this way, each processor accesses the array part corre-

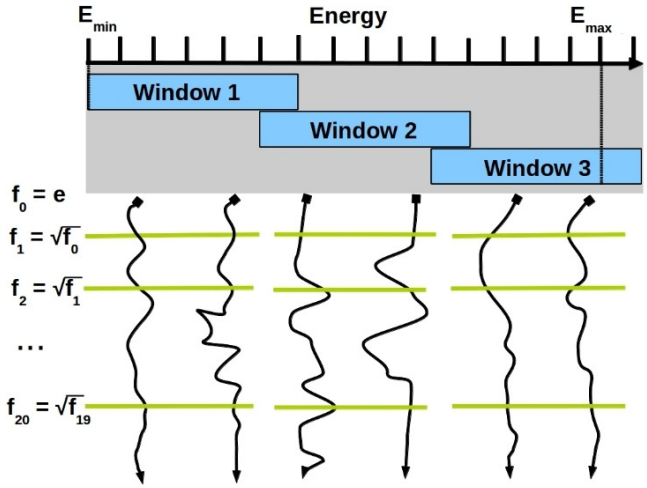

Figure 4.1: ParADenSum code structure. E_{min} and E_{max} are respectively the minimum and maximum energy E for ρ_{vib} (E) evaluation. The energy range is divided into overlapping windows, and each energy window contains the same number of bins. Black continuous lines represent random Monte Carlo walks, and green lines the averaging of ρ_{vib} (E) and the rescaling of the modification factor.

sponding to its own window without interfering with other tasks. At the end of the random walks, MPI reduction is invoked to merge each processor array into a global unique one that includes the results of all walkers. This strategy is depicted in figure 4.2. Following Barker et al.,[168] we set the number of energy bins for the lowest energy window such that the lowest energy bin contains just a single quantum state, i.e. the ZPE one. In this way $\rho_{vib}\left(E_{zpe}\right)=1/\Delta E$ for that energy bin and the values of ρ_{vib} (E) for the other bins are rescaled accordingly. A matching between the overlapping energy window bins allows to extend this normalization to all windows. The final rescaled density profile T_{tot} (E) is built by joining the ρ_{vib} (E) of different windows where the inverse microcanonical temperature $d\ln\left(\rho_{vib}\left(E\right)\right)/dE$ matches more accurately, as described in Ref. [171]. Eventually, the ParADenSum pseudo code is reported in figure 4.3.

4.3 The Algorithm ParSCTST

The code ParADenSum is applied to compute fully coupled anharmonic vibrational partition functions. The same implementation can be adapted to evaluate SCTST rate constants. To achieve this goal the starting point is the expression

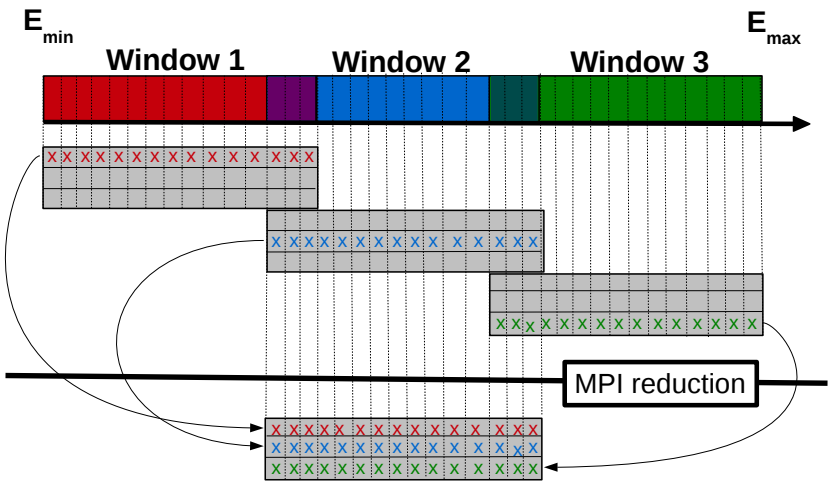

Figure 4.2: MPI reduction scheme.

for the SCTST rate whose derivation have been recalled in the previous chapter. Equation 3.22 can be simplified considering that the translation of the center of mass is separable, and, at low temperatures, also the rotations can be considered apart. With these assumption the semiclassical rate constant is

$$k_{SCTST}(T) = \frac{1}{h}\frac{Q^{\dagger}_{tran}Q^{\dagger}_{rot}}{Q_r}\int dE e^{-\beta E} P(E) \tag{4.7}$$

where the integration variable E is the vibrational energy, Q_r is the reactant partition function that can be computed with the ParADenSum program described in the previous section, while $Q^{\dagger}_{tran}$ and $Q^{\dagger}_{rot}$ are the translational and rotational partition functions of the transition state.

The problem in evaluating expression 4.7 is the computation of $P(E)$, that, according to its definition 3.27, is a nested sum that cannot be computed directly for systems with more than 4 atoms. To overcome this difficulty Barker et al. provided a simple modification of the WL strategy described in the previous section that was implemented in the code SCTST.[192] The idea is to compute the effective vibrational partition function at the transition state. This quantity is obtained by considering all the real frequencies of the transition state and

Algorithm 1 ParAdensum pseudo-code.

Require: n, number of windows
Require: w, number of walkers
Require: o, overlap between neighbour windows
Require: fp, flatenss percentage

1: Divide the whole energy range in n windows with overlap o
2: Initialize: $f = e$, $g_{n,w}(E) = 0$, $H_{n,w}(E) = 0 \; \forall \; n, w$
3: Associate the window n to the process n
4: **for** $i = 1$, 21 **do**
5: **for** $j = 1$, w **do**
6: Initialize random number generator with process dependent seed
7: **if** $i = 1$ **then**
8: Find an acceptable **v** in the window by WL in whole energy range
9: **else**
10: Retrieve walker information
11: **end if**
12: **while** $\min[H_{n,w}(E)] > \overline{H_{n,w}(E)} * fp$ **do**
13: Select new **v** varying old one
14: **if v** has an energy in the process window **then**
15: Accept or reject the step
16: $g_{n,w}(E) = g_{n,w}(E) + \ln(f)$ and $H_{n,w}(E) = H_{n,w}(E) + 1$
17: **end if**
18: **if** number of iterations exceeds a cut off value **then**
19: Exit from while loop
20: **end if**
21: **end while**
22: Save information of the walker
23: **end for**
24: Average $g_{n,w}(E)$ over all walkers in the window
25: Redistribute $\overline{g_{n,w}(E)}$ to all w walkers in the window
26: $f = \sqrt{f}$
27: **end for**
28: Reinitialize walkers information
29: Normalize $g_{n,w}(E)$ respect to the first non-zero element in the overlap to obtain $T_{n,w}(E)$
30: MPI reduction of $g_{n,w}(E)$, $H_{n,w}(E)$ and $T_{n,w}(E)$
31: Scale $T_{n,w}(E)$ sequentially
32: Join $T_{n,w}(E)$ from all windows to make $T_{tot}(E)$ with derivatives method

Figure 4.3: ParADenSum pseudo code. Here the variable g indicates the logarithm of the vibrational density of states function. In the pseudo code the term "process" is a shortcut for MPI parallel processes.

their anharmonicities, while disregarding the imaginary mode. This effective vibrational partition function is evaluated with the same algorithm that was employed for the partition function of stable molecule. Then it is used to sample the most important set of vibrational quantum numbers that contribute to the sum 3.27. The imaginary frequency $i\omega_{nvib}$ and its coupling factor $x_{i,nvib}$ with the i-th degree of freedom (i=1, nvib-1) with all the others degrees of freedom are used only in the evaluation of the generalized barrier penetration integral 3.33. Our parallel algorithm ParADenSum can be adapted in the same way to obtain the ParSCTST code. In conclusion, the combination of ParADenSum and ParSCTST programs provides an efficient parallel implementation of SCTST that can be applied to high dimensional systems.

To test the ParSCTST code we first address the computation of the rate constant for the OH + H_2 reaction. The results are reported in graph 4.4. A well known problem in evaluating rate constants that the result is very sensitive from the accuracy of the potential energy surface. An advantage of the SCTST method is that the full potential energy surface is not necessary, nevertheless the frequencies and anharmonicity matrix, as well as the height of the barrier, must be computed with a high level of theory to assure reliable results. In our case we have compared two ab intio levels of theory UCCSD/cc-pVTZ and UMP2/cc-pVTZ. The comparison with the exact calculation is only qualitative because the SEWD PES was obtained with a different level of accuracy.[193] From inspection of figure 4.4 it is clear that TST gives very inaccurate estimates at lower temperatures due to tunneling neglect, while the SCTST are in qualitative agreement with the exact values. Interestingly, the exclusion of the anharmonicity couplings leads to an overestimation of the rate constant at low temperatures (compare for instance the light blue and the green dots is the graph).

To demonstrate the potentialities of this implementation to get semiclassical rate constant of high dimensional systems work is in progress to evaluate the isomerization reaction of the the aryl radical 2,4,6-tri-tert-butylphenyl to 3,5-di-tert-butyleneophyl. As sketched in scheme 4.5, this process is a proton transfer reaction. This problem is challenging for two reasons. First the system includes 135 fully coupled vibrational degrees of freedom. Secondly, tunneling is known to play a crucial role due to the proton transfer mechanism which characterizes the reaction,[194] and experimental values for the rate constant for this process have been measured (see figure 4.6).[195] Thus, this system has already been adopted as a test case for tunneling corrected rate expressions.[196]

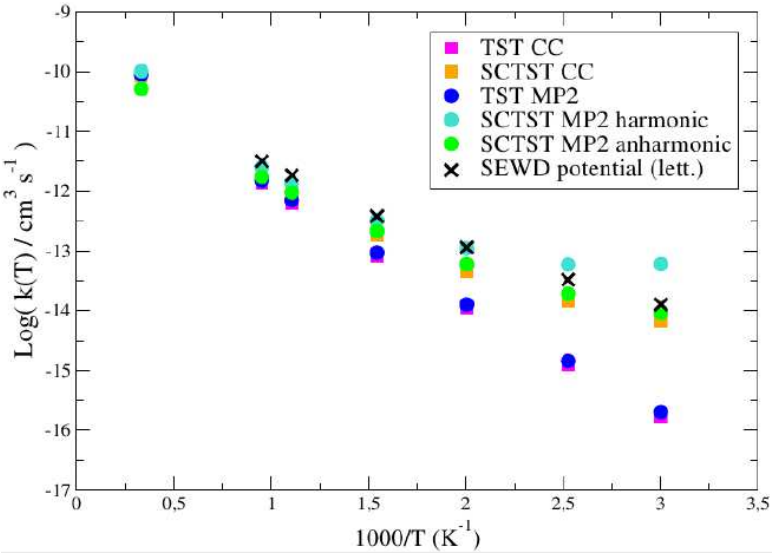

Figure 4.4: The graph compares the OH + H_2 reaction rate constant computed with various methods. Squares are the TST (pink) and the SCTST (yellow) estimates based on ab initio calculations at the UCCSD/cc-pVTZ level of theory. The circles are the results obtained from UMP2/cc-pVTZ ab initio calculations. In particular, the blue circle is the TST result, the green circles are the SCTST results, while the light blue circles are the SCTST results in which all anharmonic couplings are set to zero. Finally, the black crosses are the exact quantum scattering results based on the SEWD potential energy surface.[193]

4.4 Results and Discussion

In this section we describe the results of the calculation of $\rho_{vib}\,(\mathrm{E})$ for several systems. First, we consider model systems to check the correctness and the scalability of our implementation. Then we analyze which is the impact of the flatness criterion and the exploitation of multiple walkers in the accuracy and efficiency of our codes. Finally, we turn into real and complex molecule calculations to show the computational advantages of our strategy with respect to other codes for density of states calculations.

4.4.1 Model Systems

The calculation of the density of states $\rho_{vib}\,(\mathrm{E})$ for harmonic model systems, i.e. uncoupled harmonic oscillators, is only in part analytical. While the harmonic

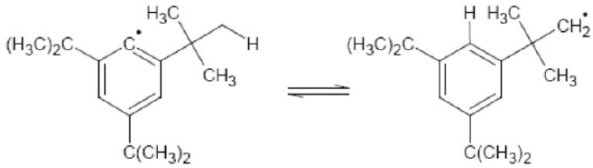

Figure 4.5: The isomerization reaction of the 2,4,6-tri-tert-butylphenyl to 3,5-di-tert-butyleneophyl is a proton transfer reaction.

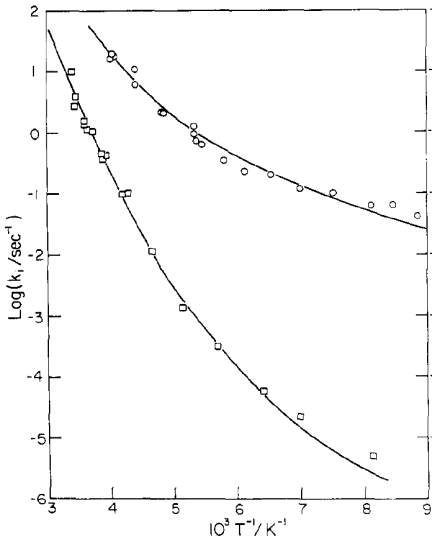

Figure 4.6: The experimental rate constant as a function of the temperature for the isomerization reaction of the the Aryl radical 2,4,6-tri-tert-butylphenyl to 3,5-di-tert-butyleneophyl. The upper curve is for the regular process, while the lower curve is the for the isotopic substitution of the transferred proton with deuterium. In both cases a significant deviation from Arrhenius behavior is observed. (Figure from reference [195]).

partition function is analytical, ρ_{vib} (E) is obtained by a convolution in energy space. This integration is not analytical unless the single mode density of states is approximated. This is the case of the classical approximation where the one dimensional harmonic ρ_{vib} (E) = $1/\hbar\omega$ is convoluted with the N-dimensional expression to obtain

$$\rho_{vib}(E) = \frac{E^{N-1}}{(N-1)!\prod_{j=1}^{N}\hbar\omega_j} \tag{4.8}$$

which is employed in the classical RRKM theory.[197] Alternatively, we can consider that the cumulative sum of states $N_{vib}(E)$ is related to the partition function by the inverse Laplace transform:

$$N_{vib}(E) = \frac{1}{2\pi i}\int_{\sigma-i\infty}^{\sigma+i\infty}\frac{e^{\beta E}}{\beta 2^N\prod_{j=1}^{N}\sinh\left(\frac{1}{2}\beta\hbar\omega_j\right)}d\beta \tag{4.9}$$

and that ρ_{vib} (E)=d$N_{vib}(E)$/dE. To exploit this route, we perform the inverse Laplace transform numerically, using an algorithm based on an expansion in Fourier Series.[198] We found this approach useful to manage the cumulative sum of states up to 20 uncoupled harmonic oscillators. The main limitation of this approach is that the inversion of the Laplace transform is numerically stable only within a small energy range, and reliable results of $N_{vib}(E)$ are limited to energies up to around 1500 cm^{-1} above the zero point energy. Given the inaccuracy of Eq.(4.8),[156, 157, 199, 200] in alternative, for higher energies the Whitten and Rabinovitch semi-empirical approximation can be employed.[201, 202]

In figure 4.7 we consider a 1-d harmonic oscillator. ParADenSum correctly reproduces the results provided by the exact counting of states. The classical results, labeled as CL, reproduce on average the discrete quantum mechanical counting given by the straight line. The ILT can manage the exact counting up to an energy threshold. For higher energy, ILT results are on the top of the CL results. However, within this limitations, ILT is going to be useful for higher dimensionality systems where the "Exact Count" approach becomes unfeasible.

We then consider the calculation of the cumulative density of vibrational states N_{vib} (E) for uncoupled harmonic systems of increasing dimensionality. The harmonic frequencies have been chosen randomly within a range from 100 cm^{-1} to 4000 cm^{-1} which is representative of typical molecular vibrations, and the anharmonicity matrix elements x_{ij} are set to 0. Up to four dimensions, exact calculations can be performed. The typical quantum mechanical staircase profile of N_{vib} (E) is still visible for such a low dimensionality. As reported on the top panel of 4.8, ParADenSum and ILT faithfully reproduce the staircase exact results.

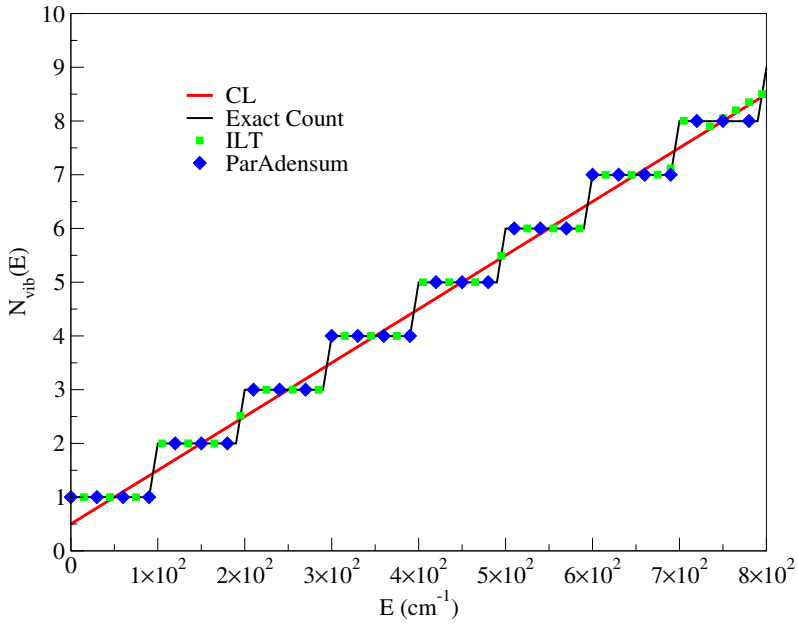

Figure 4.7: Cumulative sum of the density of states $N_{vib}\,(E)=\int_0^E \rho_{vib}\left(E^{'}\right)\mathrm{d}E^{'}$ for the one dimensional harmonic oscillator. Exact results are the "Exact Count" ones. CL stands for classical, ParADenSum for the present WL calculations and ILT for the inverse Laplace transform approach.

Instead, CL calculations overestimate $\rho_{vib}\,(\mathrm{E})$ at low energies while reproducing the exact results at higher energy ranges. The reasons of this deviation are explained by the approximation employed to obtain eq. 4.8. The convolution summation over all possible quantum numbers is approximated as an integration over a continuum of energies and corresponding fictitious fractional quantum numbers. This over-counting is severe at low energies where the density of states is low, while it is moderated at higher energies where the density of states is higher and the variation over the quantum numbers generates a quasi-continuum of states. A comparison between the three panels in 4.8 also shows that the CL approximation at low energies becomes less accurate as the dimensionality is increased. As a result ParADenSum and ILT are in excellent agreement up to twenty dimensions. When the dimensionality is further increased, the ILT approach can no longer be applied, and an implementation of the SPT of eq. 4.2 is not even possible.

In 4.9 we look at the cumulative density of states $N_{vib}\,(\mathrm{E})$ for a system of 80 (4.9-a and 4.9-b) and 150 (4.9-c and 4.9-d) harmonic oscillators. We check

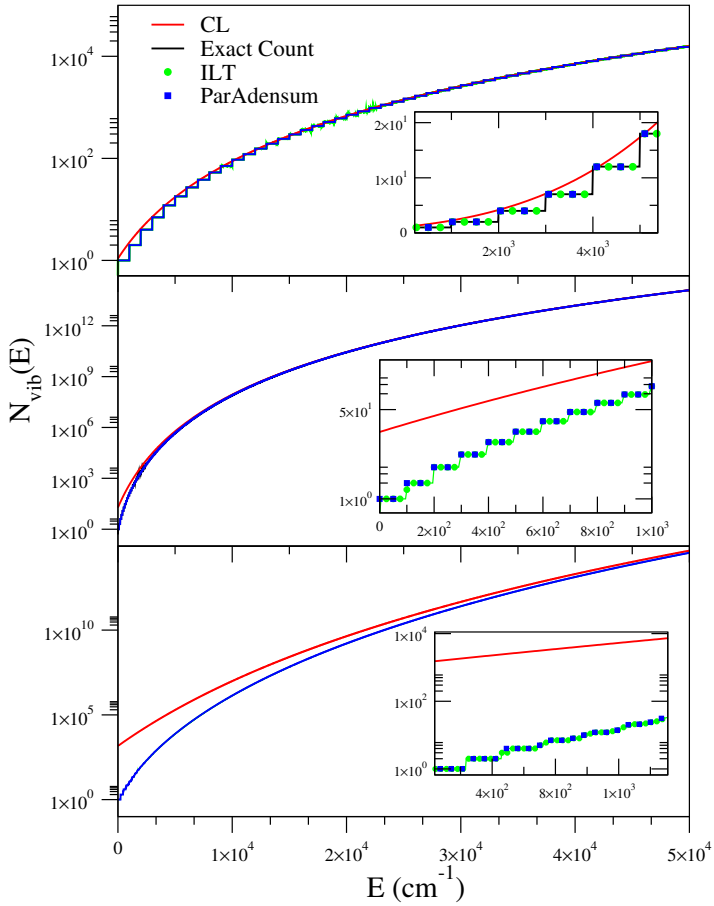

Figure 4.8: Cumulative sum of state N_{vib} (E) calculations. 4 (upper panel), 10 (middle panel) and 20 (lower panel) uncoupled harmonic oscillators. "Exact Count" are the exact results (continuous black line), CL stands for the classical approximation of eq. 4.8 (continuous red line), and ILT for the numerical Inversion of Laplace Transform of eq. 4.9 (green diamonds). ParADenSum results are reported as blue squares.

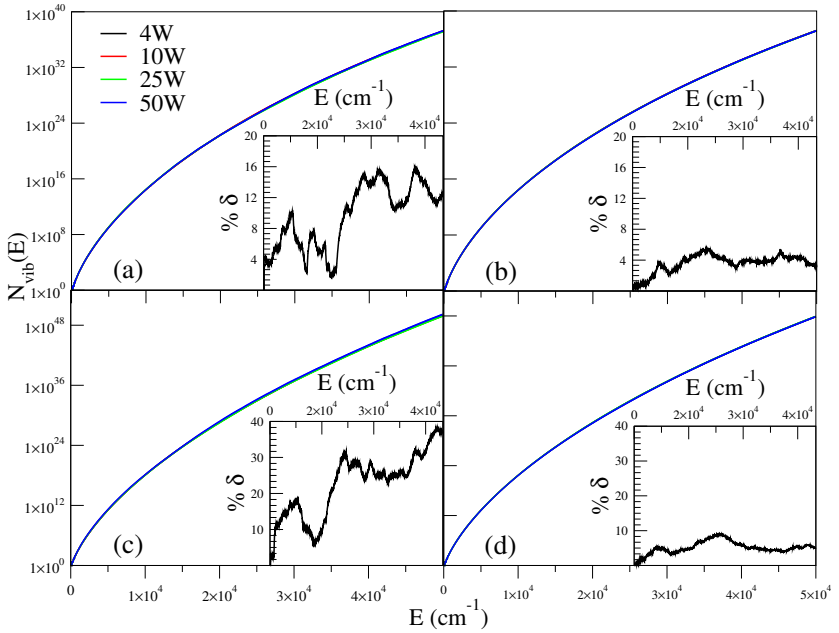

Figure 4.9: ParADenSum code results for uncoupled harmonic oscillator systems with increasing degrees of freedom. (a) and (b) refer to 80 oscillators, while and (c) and (d) to 150. Flatness criterion is 80% for (a) and (c), 95% for (b) and (d). Insets report the values of the percentage deviation of $N_{vib}(E)$ calculated with different window partitioning $\delta(E)=100\times\sqrt{\sum_{i=1}^{W}\left(N_{vib,i}(E)-\overline{N_{vib}(E)}\right)^2}/\overline{N_{vib}(E)}$ where $\overline{N_{vib}(E)}=\frac{1}{W}\sum_{i=1}^{W}N_{vib,i}(E)$ and W is the number of windows.

how ParADenSum performs for different windowing strategy and which WL flatness criterion is more suitable. For this purpose, we compare the left panels calculations where a 80% (4.9-a and 4.9-c) of flatness criterion for the histogram H(E) is applied to right ones where a 95% (4.9-b and 4.9-d) flatness criterion is employed. For each panel, N_{vib} (E) is calculated with different numbers of windows and reported in logarithmic scale. The inset of each panel reports the percentage deviations for different choices of window numbers. An increase in WL flatness criterion significantly reduces standard deviations of the windowing and guarantees that results are independent of the windowing choice. We will show below how computational efficiency increases when increasing the number of the windows. The original ADenSum code is limited to systems of about one hundred degrees of freedom, while ParADenSum can easily allocate 150 degrees

of freedom, and this is not yet an upper bound, since further increment in the dimensionality of the problem is achievable.

The main conclusion of this section is that ParADenSum is not only able to reproduce exact cumulative vibrational densities of states for low-dimensionality systems, as calculated by means of the "Exact Count" approach, but it can also be successfully applied to significantly more complex systems.

4.4.2 Influence of Flatness Criterion and Multiple Walkers

We now investigate the possibility to exploit multiple walkers as a possible parallelization strategy. We chose the water molecule as a test case, since the exact $\rho_{vib}(E)$ can be obtained by direct counting. We employed the experimental vibrational data for the exact counting.[203]

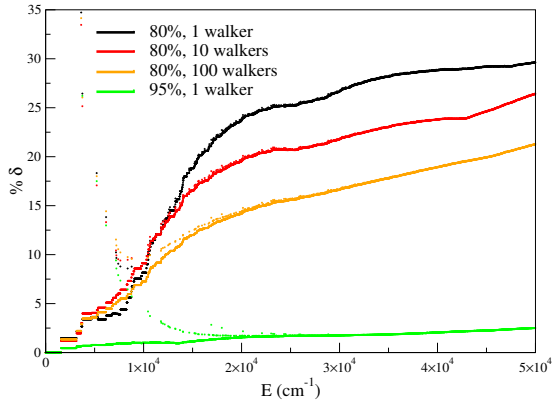

Figure 4.10: Percentage error deviations for the $N_{vib}(E)$ calculation of water molecule. Black dots is the result obtained in a single run with one walker per window and 80% flatness criterion. Red and orange dots are the averaged results over 10 or 100 runs for WL 80% flatness simulations employing respectively 1 walker in each windows. Green dots are for a single walker WL simulation at 95% flatness criterion.

We wonder if greater accuracy can be achieved by increasing the number of walkers. We performed these tests for a given 80% flatness of the WL algorithm and compare the results to a single-walker 95% flatness simulation. Indeed, we expect that the more the walkers, the greater the accuracy. This test gives just a rough estimate, because it compares a run with one walker per window with 95% flatness with the average DOS obtained with 10 or 100 runs done with a single walker in each energy window with 80% flatness. Figure 4.10 clearly

shows that a single-walker simulation with a 95% flatness criterion provides by far more accurate results than simulations based on a larger number of walkers, but with a weaker flatness constraint. Figure 4.10 reports the percent error deviation of different ParADenSum setups. For all simulations reported, the energy range has been divided into 20 windows made of 338 energy bins each (including the overlap). We observe that the accuracy is roughly linear with respect to the energy variation, except for a few bins. However, accuracy is still preserved within 35%. Computational overheads must also be taken into account for a fair assessment of the most efficient setup. A typical WL simulation for water at 80% of flatness requires a total of 2.1×10^8 sweeps. Considering a parallelization strategy where multiple walkers are placed on different cores with different seeds, the total computational cost is a multiple of the number of walkers. For instance, if 100 walkers are employed, the number of total Monte Carlo sweeps is 2.1×10^9. In comparison, when simulating the same molecule with the much stricter flatness criterion of 95% but with a single walker, after 21 iterations, we find a total number of Monte Carlo sweeps of 1.36×10^9, which is almost the same order of magnitude than the 100-walker simulation. At the light of these considerations, it is clear that a straightforward embarrassing parallel version of the code is not convenient since averaging over 100 runs one had a worse accuracy than a single run with higher flatness with almost the same computational cost.

For this reasons, in the code we implemented the multiple walkers in such a way they average their DOS estimate at the end of each one of the 21 iterations, as illustrated in picture 4.1. This intermediate averaging turns out to have a significant impact on the code performance. To prove this, for different flatness criteria, we have compared the computational effort and the accuracy of the DOS calculations performed with a single random walk in each window with the computations done with multiple walkers in each window. We have taken into account two test cases, the water molecule and the transition state (TS) of Cl + CH_4 reaction, using ParADenSum and ParSCTST codes respectively. For both systems with a fixed number of energy windows, we computed 10 DOS while an increasing number of walkers per window was employed. Every walker was initialized with a different seed for the generation of the random numbers chains. In this way the random walks are completely independent. We computed the Mean Relative Error (MRE) for each one of the 10 DOS using the formula (4.10)

$$MRE_j = \frac{1}{N_{tot}} \sum_{i=1}^{N_{tot}} \frac{|DOS_i - Ref_i|}{Ref_i} \times 100 \qquad j = 1, \ldots, 10 \tag{4.10}$$

where N_{tot} is the total number of energy bins in the whole energy range. The energy bins are labeled by the i index. Ref_i and DOS_i are respectively the values of the computed DOS and the value of the DOS taken as a reference at the energy of the i-th energy bin. The j index labels the simulations that produce a DOS function. To obtain the exact value we used the DoLoop code for the water molecule. On the contrary, for the transition state of the Cl + CH_4 reaction a direct count calculation of the DOS is not feasible. Therefore, in this case we took as a reference the DOS calculated in a single run with the 99% flatness value and using 100 walkers in each energy windows. After, we evaluated the average MRE

$$\overline{MRE} = \sum_{j=1}^{10} \frac{MRE_j}{10} \tag{4.11}$$

and the corresponding standard deviation value

$$\sigma = \sqrt{\sum_{j=1}^{10} \frac{\left(MRE_j - \overline{MRE}\right)^2}{9}} \tag{4.12}$$

We regard these quantities as a measure of the accuracy of the results. To evaluate the computational effort instead, we calculated the average Steps To Flatness (ave-STF), averaging the total number of Monte Carlo steps needed to reach the convergence over the 10 independent runs.

The Panel a of both Tables 4.1 and 4.2 shows the results from a set of simulations done with a single walker in each energy window and with an increase of the flatness criterion. The $\overline{MRE}$ and the σ values decrease along with the increase of the flatness value. This trend suggests that if it was possible to do a simulation with a 100% flatness, the $\overline{MRE}$ and σ would be equally 0. Practically, it is impossible to run such a simulation because it would require an excessive computational effort. By looking at panels (b), (c), (d), (e) and (f) of Table 4.1 and panels (b), (c), (d) of Table 4.2, we observe a convergence of the $\overline{MRE}$ and the σ by rising the number of walkers with a fixed flatness criterion. It is important to point out that if the required flatness criterion is too low, the density of states cannot be improved indefinitely by increasing the number of walkers in each energy window, as panels (b) of Table 4.1 clearly show. Here the $\overline{MRE}$ reaches a plateau increasing the walkers number from 10^3 to 10^4 walkers, while the σ is reduced.

We turn now to the computational effort evaluation. Comparing the ave-STF and the$\overline{MRE}$ of the 99.9% flatness criterion calculation reported in the panel (a) of Table 4.1 with the 100 walkers in the panel (d) of the same Table, (or also the

99.9% flatness criterion calculation reported in the panel (a) of the Table 4.2 with the 100 walkers one in the panel (b) in the same Table), we conclude that the exploitation of multiple walkers in a simulation with a sufficiently high flatness criterion, can reach a comparable $\overline{MRE}$ than a single walker run with higher flatness.

4.4.3 Molecules

We now turn to real and more complex molecule calculations, aiming at estimating the cumulative sum of the number of vibrational states in the bound-state energy region. We have investigated several molecules of increasing complexity, i.e. the HOCO radical, N-methylmethanimine ($CH_2 = NCH_3$), naphtalene ($C_{10}H_8$), triethylphosphine ($P(CH_3CH_2)_3$), and anthracene ($C_{14}H_{10}$). The number of vibrational degrees of freedom involved are 6, 18, 48, 60, and 66 respectively. Results are reported in 4.11, where each panel shows the cumulative density of vibrational states and the percentage deviation of the windowing strategy as defined above (see caption of 4.9).

panel (a)				
Walkers	Fltn(%)	$\overline{MRE}$	σ	ave-STF
1	95	0.87	0.42	7.71×10^{8}
1	99	0.26	0.11	7.74×10^{9}
1	99.9	0.20	0.06	2.92×10^{11}
1	99.99	0.18	0.05	9.01×10^{11}

panel (b)				
Walkers	Fltn(%)	$\overline{MRE}$	σ	ave-STF
10	80	1.38	0.88	-
100	80	0.83	0.30	-
1000	80	0.39	0.07	5.92×10^{10}
10000	80	0.42	0.03	5.90×10^{11}

panel (c)				
Walkers	Fltn(%)	$\overline{MRE}$	σ	ave-STF
10	85	0.84	0.53	-
100	85	0.41	0.29	-
1000	85	0.29	0.07	9.64×10^{10}

panel (d)				
Walkers	Fltn(%)	$\overline{MRE}$	σ	ave-STF
10	90	0.63	0.30	-
100	90	0.21	0.05	1.92×10^{10}
1000	90	0.14	0.02	1.89×10^{11}

panel (e)				
Walkers	Fltn(%)	$\overline{MRE}$	σ	ave-STF
10	95	0.35	0.15	-
100	95	0.14	0.04	5.80×10^{10}
1000	95	0.13	0.02	5.78×10^{11}

panel (f)				
Walkers	Fltn(%)	$\overline{MRE}$	σ	ave-STF
10	99	0.14	0.03	5.47×10^{10}
100	99	0.10	0.01	5.25×10^{11}

Table 4.1: Test of the performance of multiple walkers for the water molecule, obtained using ParADenSum code. The exact DOS calculated with the DoLoop code has been considered as the reference to compute the Mean Relative Error (MRE) and the corresponding standard deviation value σ of the others simulations according to equations 4.10, 4.11, and 4.12. The average steps required (ave-STF) to satisfy the flatness criterion (Fltn(%)) that halts the algorithm is reported as an indication of the computational effort required by each simulation.

panel (a)

Walkers	Fltn(%)	$\overline{MRE}$	σ	ave-STF
1	95	1.06	0.80	-
1	99	0.42	0.21	1.37×10^{10}
1	99.9	0.28	0.21	1.56×10^{11}
1	99.99	0.27	0.18	7.40×10^{11}

panel (b)

Walkers	Fltn(%)	$\overline{MRE}$	σ	ave-STF
10	90	0.90	0.42	2.96×10^{9}
100	90	0.30	0.22	2.87×10^{10}
1000	90	0.22	0.09	2.86×10^{11}

panel (c)

Walkers	Fltn(%)	$\overline{MRE}$	σ	ave-STF
10	95	0.36	0.12	9.20×10^{9}
100	95	0.18	0.07	8.91×10^{10}

panel (d)

Walkers	Fltn(%)	$\overline{MRE}$	σ	ave-STF
10	99	0.13	0.07	9.00×10^{10}
100	99	0.00	-	8.46×10^{11}

Table 4.2: Test of the performance of multiple walkers for the calculation of the DOS of the transition state of Cl + CH_4 reaction, obtained using ParSCTST code. The results of the simulation with 100 walkers in each energy window and 99% of flatness has been considered as the reference to compute the Mean Relative Error (MRE) and the corresponding standard deviation value σ of the others simulations according to equations 4.10, 4.11, and 4.12. The average steps required (ave-STF) to satisfy the flatness criterion (Fltn(%)) that halts the algorithm is reported as an indication of the computational effort required by each simulation.

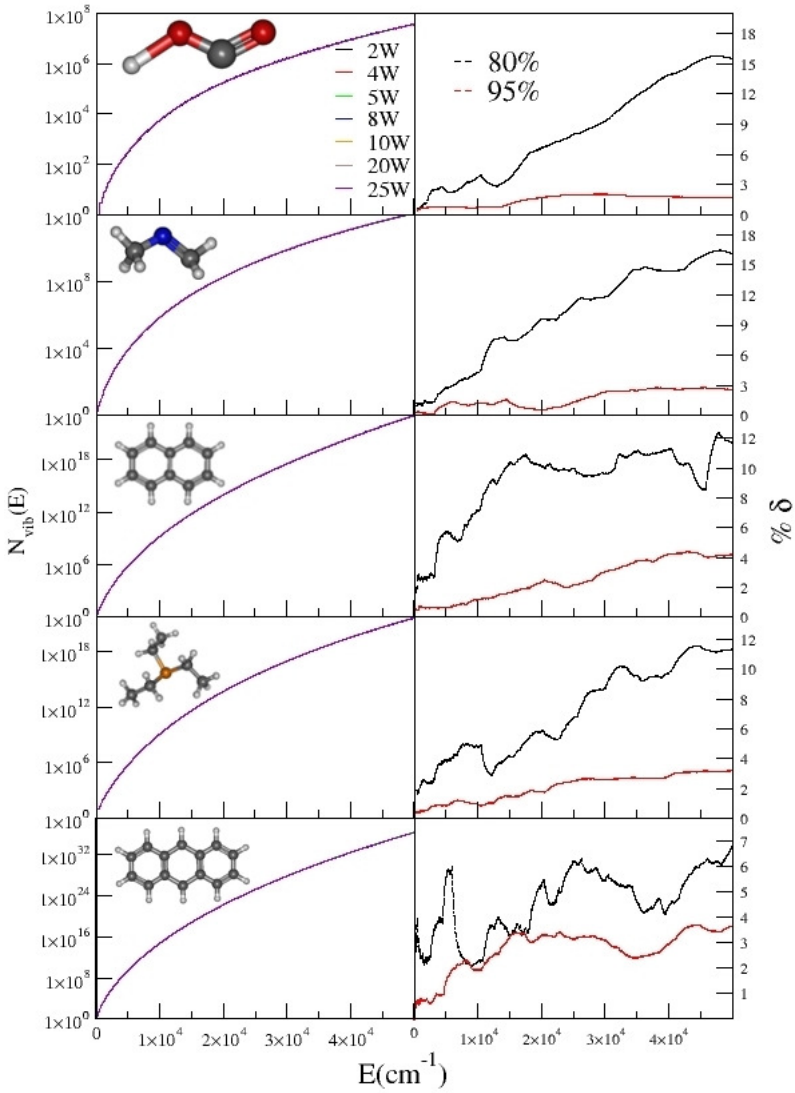

Figure 4.11: Cumulative density of states for five molecules of increasing complexity: HOCO radical, N-methylmethanimine, naphtalene, triethylphosphine, and anthracene $C_{14}H_{10}$. In the right column, the percent deviations of $N_{vib}(E)$ are reported for a WL flatness choice of 80% (black dashed) and 95% (red dashed). A single walker per energy window has been employed.

The needed harmonic frequencies ω and anharmonic x_{ij} coupling parameters have been calculated using either the Gaussian09[145] or Cfour[143] codes. In

particular, Gaussian09 has been employed to calculate frequencies and anharmonic coupling parameters at the MP2/cc-pvdz level for $CH_2 = NCH_3$ and $C_{10}H_8$, and B3LYP/cc-pvdz level for $P(CH_3CH_2)_3$ and $C_{14}H_{10}$. Furthermore, we have employed Cfour at the CCSD(T)/ANO1 level for the HOCO radical. Results for different numbers of windows are within 10% using a flatness criterion of 80% and the agreement is stricter, i.e. within 5%, for a 95% flatness choice. This value is comparable to what is expected from the WL Monte Carlo statistical deviation, so it clears the field from any possible systematic error that may have been introduced by windowing or parallelization. In other words, such a statistical interval of confidence for systems of dimensionality up to 66 degrees of freedom proves the reliability of the parallelization strategy adopted. Higher energy ranges are not plotted because Eq.(4.5) can not be applied.

4.4.4 Timing and Scalability

We now look at the computational time scaling of the code ParADenSum with the number of cores employed for the systems presented in the previous sections. All the considerations exposed in this analysis apply to the ParSCTST code as well, because the two algorithms differ only for minor features that do not affect the parallel core of the procedure. We have performed single-walker simulations with a 95% flatness constraint. The computational speed up generated by partitioning the energy range into windows is reported on the two upper panels of 4.12. The efficiency of the strategy based on multiple windows is analyzed on the lower panels of the same figure, and it is calculated as the ratio between the corresponding windowing speedup and the number of processors. We start by looking at the harmonic oscillators simulations reported on the left panels. Here the computational speed up is almost ideal (dashed line), except for the relatively low dimensional 10- and 20-harmonic oscillator systems. The almost ideal scaling makes sense by considering that the energy space for a set of uncoupled harmonic oscillators is quite trivial. The unfavorable scaling of the lower dimensional systems can be explained by the more accentuated sparsity of their energy levels at low energy. As a consequence, bins within the low-energy windows are characterized by bigger differences in the density of states, thus requiring a higher number of Monte Carlo sweeps before the flatness criterion is satisfied, and creating a bottleneck for the whole calculation. For this reason we developed an enhanced version of the code that supports the possibility to divide the whole energy range in windows with different width. For instance, in computing the partition function of the 2-4-6-tri-tert-butylphenyl radical, we first set all the windows with the same width. By analyzing the computational

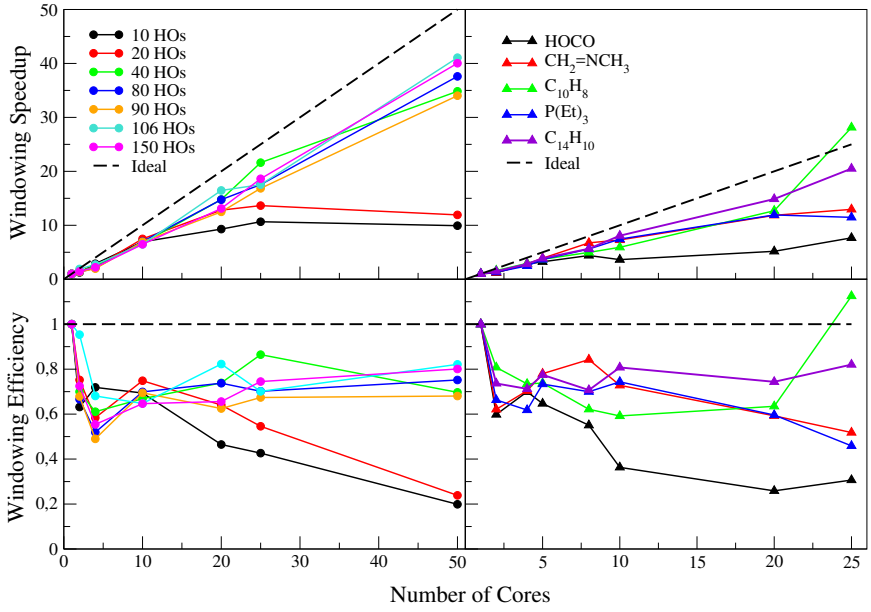

Figure 4.12: Computational speed-up and efficiency with respect to the number of cores for several systems. Left panels report results for uncoupled harmonic oscillators and right panels for molecules.

time required by each thread, as reported in the second column of table 4.3, the first window is much slower than the others. Its execution time is the overall computation time, since the other threads have to wait for it to be completed. Therefore, we have tried to perform the same computation setting the first two windows to be smaller compared to all the others. In this case (third column of table 4.3), a more equilibrated execution time is measured for all threads, and the total execution time is almost halved. In fact, even if the first window is still the slower one, it requires half of the computation time compared to the implementation with equal windows width. This promising strategy with unbalanced windows width is under development.

Indeed, the lower left panel confirms that ParADenSum outperforms serial codes like ADenSum, even if its efficiency deteriorates when too many energy windows are employed for the lower dimensional systems. When considering real molecules, the rationalization of the results is more cumbersome, since one needs to consider that the spacing of the vibrational levels is quite different for different molecules. We observe again that for small molecules the parallelization is not very efficient, as reported on the lower right panel. From 4.12, it is clear that the strategy adopted in ParADenSum becomes more and more convenient as the

	Equally spaced wid.	Unequally spaced wid.
1	2280	1194
2	1140	534
3	780	1182
4	600	798
5	540	711
6	540	621
7	480	543
8	420	516

Table 4.3: Comparison of the execution time per thread of the implementation with windows of the same width (Equally spaced wid.) with the implementation with windows of different width (Unequally spaced wid.). In this case, the first two windows are smaller that all the others. The test case is the computation of the partition function for 2-4-6-tri-tert-butylphenyl radical, with eight windows. The underlined value in each column is the longest execution time, that represent the total time required by the parallel algorithm to complete the computation.

number of degrees of freedom of the molecule increases. However, the speed-up does not monotonically increase with the number of degrees of freedom. For example, the parallelization efficiency for naphtalene ($C_{10}H_8$) is greater than that of both P $(CH_3CH_2)_3$ and $C_{14}H_{10}$, even if the vibrational space dimensionality of naphtalene is smaller. Actually, naphtalene presents super-scalability, as it scales with parallelization even better than a set of uncoupled harmonic oscillators. We believe that the reason for naphtalene super-scalability lies in the rigidity of this molecule, which is responsible for its quite high vibrational frequencies if compared to those of other molecules where internal floppy modes are present. As described above, the frequencies of the uncoupled harmonic oscillators were chosen randomly in a range of frequencies that includes floppy modes. This explains the better scalability of naphtalene even with respect to the harmonic systems tested.

5 Beyond Transition State Theory

The last two chapters have dealt with Miller's SCTST and its practical implementation. [38, 39, 118, 204, 120] Even if this method accounts for anharmonicities and relies on sophisticated quantum corrections, it is still a TST approach. The main assumption of all TSTs theories is the direct dynamics approximation. Therefore, this class of methods, rely on the definition of a dividing surface that separates reactants from products and assumes that only the positive flux measured at time zero contributes to the rate constant.

The first difficulty in applying this approximation arises from the necessity to choose a specific dividing surface. The basic TST prescription is to set the DS in correspondence of the saddle point of the potential, that is identified with the transition state (TS).[47, 205] In fact, thanks to the zero time approximation, the point of view of TST is that the narrow region around the saddle point of the PES rules the reaction behavior. For instance, SCTST on which the work of the previous chapter was based, takes into account anharmonic modes couplings, includes tunneling corrections, and has the advantage that it can be applied to large dimensional reactive systems. However, being a TST like approach, it has been shown to be not very accurate in representing corner-cutting effects due to tunneling, and it is not very accurate for representing large deviations of the variational transition-state location from the saddle point for overbarrier processes.[206] In general, TSTs are good at describing reactions with a significant energy barrier that separate reactants and products, while they are problematic when a precise position of the saddle point on the PES is not well defined. A first situation of this kind the reactions of an ion with a molecule. In this case, their PES is characterized by a barrier preceded by a well. For instance, for the SN2 reactions Cl^- + CH_3Br, and F^-(H2O) + CH_3Cl it has been shown that multiple crossings of the barrier may take place, in contrast to the direct dynamics assumption of TST. Another type of process that is difficult to handle with TST like treatments is the case of barrierless reactions, that is typical for association and dissociation unimolecular reactions. Finally, there are cases in which the dynamical bottleneck lies in the proximity of a flat region of the potential.[206] This is the case of recently detected roaming dynamics, that, for instance, was found to be significant in the unimolecular dissociation of H_2CO

and CH_3CHO.[207, 208] In addition, other studies reveal reaction dynamics that are either not dominated by a TS or that appear to occur without passing through an obvious TS. For example, the formation of CO + H + H_2 products from the reaction CH_3 + O takes place in stepwise fashion from reaction intermediates. Furthermore, the H + HBr and H + CH_4 reactions (at high energies) follow pathways that are very far from the transition state (TS) location. Thus, it has been proved, also through experiments, that reaction mechanisms that bypass the TS or do not involve a TS are not only possible, but also may be widespread.[209]

Besides these cases, when it is possible to divide the coordinate space between reactants and products, the direct dynamics assumption makes it possible to conveniently formulate rate expressions that are based only on thermodynamics information. Unfortunately, in general, this leads to low accuracy rate estimates. For example, in classical mechanics TST rate is only an upper bound to the exact rate value. To overcome this problem, more sophisticated version of TST have been formulated. The state of the art from the classical point of view is represented by Variational Transition State Theory (VTST).[48, 210] In this case, the position of the DS is optimized in a way that recrossing is minimized. Thus the rate estimate given by VTST is the lower upper bound to the exact rate. The extension of TST in quantum mechanics is cumbersome, because it is invalidated by the uncertainty principle. However, in the literature many attempts in this direction can be found. In particular, a full quantum theory that embodies all the qualitative aspects of TST is the Quantum Instanton (QI).[121, 122, 73] Even in this case, the position of the two dividing surfaces have to be optimized. It is therefore evident that TSTs are characterize by a strong dependence of the position of the dividing surface. On the contrary, full dynamical approaches to both classical and quantum reaction rate constants calculations, are independent on the choice of the dividing surface.

For all these reasons, a reaction rate formulation that goes beyond the TST approximation would be very valuable. To get rid of the direct dynamics approximation, it is necessary to take into account contribution from real time dynamics that allows to include recrossing effect contribution to the rate constant. An interesting formulation would include these real time effects without the necessity to afford the full quantum dynamics evolution of the reactive system. A valuable approach would rely on a local dynamics, in the vicinity of the reaction bottleneck. In this way, by moving away from the zero time approximation, it would also affect the strict dependence of the rate on the particular position of the dividing surface. A new approach that goes in this direction is described in the next chapter.

6 A Quantum Method for Thermal Rate Constants Calculation[1]

In this chapter we introduce a quantum formulation for the calculation of the thermal rate constant with the main goal of reducing the strong dividing surfaces (DS) dependency of previous QTST formulations. The method is obtained by stationary phase approximation (see appendix 2.7) of the thermal flux-flux correlation function integral 2.42.

The idea is pictorially described in Fig.(6.1), where a wave function is transmitted across a barrier. Differently from classical TST and some previous QTST approaches, we propose a two DSs approximation, where the DSs are arbitrarily located apart, i.e. on opposite sides of the barrier. The idea is to have the wave packet propagating from one DS to the barrier, tunneling through the barrier and finally ending up to the products side DS through an additional real time quantum propagation. The picture can be easily extended to many dimensions by considering the wave packet propagating along any energy path. The amount of real versus imaginary time and the expression of the quantum propagator that follow this picture is not obtained by the product of three (two real and one imaginary time) propagators. Since all paths should be taken into account, this approach would end up in a real-time Path Integral calculation, which is numerically quite challenging. Instead, we will show below how the rate expression and the amount of real versus imaginary time can be found directly through a stationary phase approximation to the flux-flux correlation function time integral. Given this picture, any re-crossing effect is greatly reduced, since the two DSs are far apart, one on the reactants and the other one on the products valley. In particular, to obtain the rate estimate we will show that one needs only a single time evaluation of the flux-flux correlation function, which is the time t_s at which a given quantity is stationary. When t_s=0, one may obtain the QI formulation, a typical QTST approximation. When $t_s \neq 0$, the estimate of the thermal rate is

[1]This chapter is the reproduction with some minor changes of the paper **Chiara Aieta**, and Michele Ceotto, "A Quantum Method for Thermal Rate Constant Calculations From Stationary Phase Approximation of the Thermal Flux-flux Correlation Function Integral" *J. Chem. Phys.* **146**, 21411 (2017).

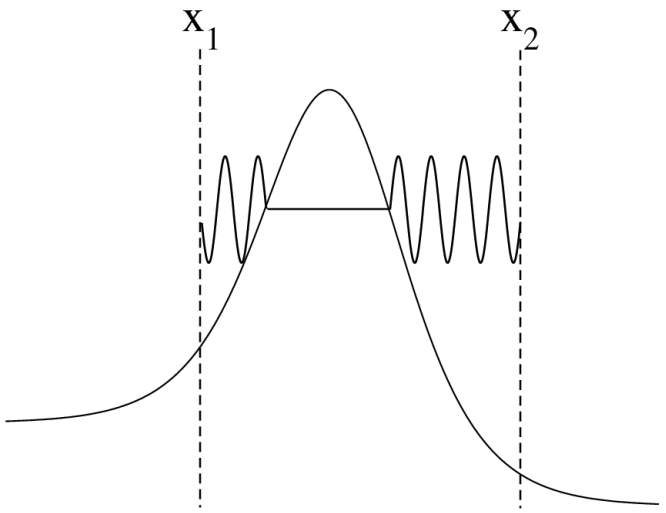

Figure 6.1: Pictorial representation of the method here presented: the thermal rate constant is calculated at fixed DSs positions by evaluating the quantum real and imaginary time propagator for a fixed amount of total time.

much less dependent on the DSs position than other QTST formulations. This is a very important feature, since the best DSs location is not trivial to find for complex systems.

Chapter 6 is organized as follows. In Section 6.1 we introduce our stationary phase approximation to the thermal flux-flux correlation function integral. In the following Section, we show how the approximation is related to the QI one, and we apply it to an analytically solvable problem, i.e. the free particle. In Section 6.2 we test the method for the symmetric and asymmetric Eckart barriers and for the two collinear reactions H + H_2 and D + H_2. Finally, results are compared to some approximate methods to the calculation of thermal reaction rate constants and to exact values.

6.1 The Method

6.1.1 The Approximate Thermal Rate Expression

This paragraph presents the main idea of this work and introduces an approximate expression for the thermal rate constant. The derivation is done for the one dimensional case. However, the results can be easily generalized to many dimensions.

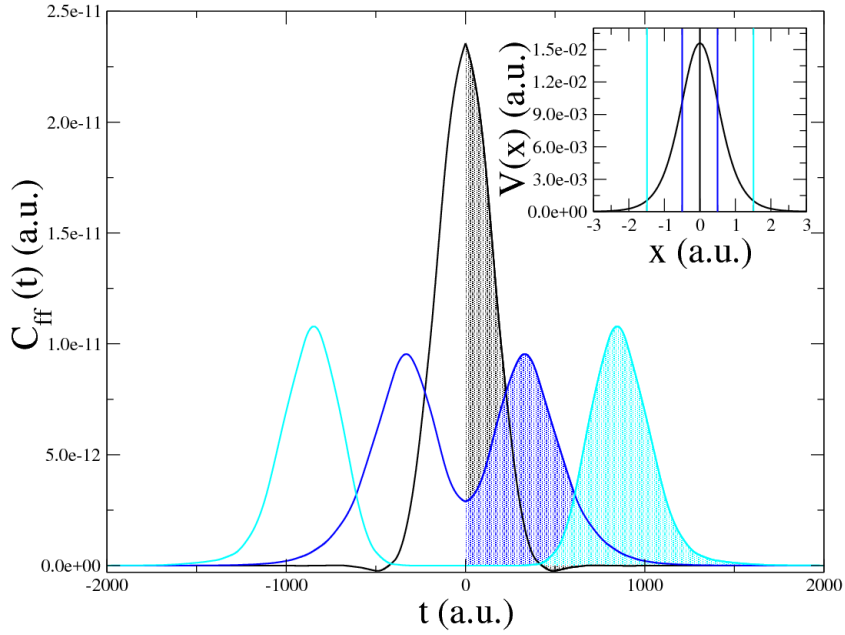

Figure 6.2: Shape of the flux-flux correlation function at different DSs locations for the Eckart barrier at 400K. The black curve is obtained when the two DSs are both located on the top of the barrier, as shown for the potential depicted in the inset. By increasing the distance between the two DSs the shape of the flux-flux correlation function gradually changes as shown by the blue and the cyan curves. The shaded area represents the value of the rate constant which is independent of the position of the two DSs. These features are general and independent of the particular potential and temperature considered.

We start from the exact quantum rate expression given by Eq.(2.42) and Eq.(2.50). The value of the exact thermal rate constant $k(T)$, which is the shaded area under the curves of Fig. (6.2), is independent of the position of the two DSs. However, the shape of the flux-flux correlation function significantly changes depending on the position of the DSs, as shown in Fig. (6.2). More specifically, when the two DSs are coincident , i.e. when $\hat{F}_1 = \hat{F}_2 = \hat{F}$, the profile of $C_{ff}(t)$ has its maximum at time t=0. Once the two DSs are separated and the distance between them increased, the correlation function becomes double bell shaped with the maxima moving away from t=0. Once the DSs are far enough, the flux-flux correlation function value for t=0 is $C_{ff}(0) \approx 0$. We now use the symmetry property of $C_{ff}(t)$ which is an even function of time, and extend the integration

limit of Eq.(2.42) to -∞ by taking half the integral

$$k(T)\,Q_r(T) = \frac{1}{2}\int_{-\infty}^{+\infty} C_{ff}(t)\,dt \tag{6.1}$$

By multiplying and dividing the integrand by the positive-definite term $\left|\left\langle x_1 \left| e^{-\frac{\beta\hat{H}}{2}-\frac{i\hat{H}t}{\hbar}} \right| x_2 \right\rangle\right|^2$ where x_1 and x_2 are the DSs position, we can restate the rate Eq.(6.1) in an equivalent form

$$k(T)\,Q_r(T) = \frac{1}{2}\int_{-\infty}^{+\infty} \frac{C_{ff}(t)}{\left|\left\langle x_1 \left| e^{-\frac{\beta\hat{H}}{2}-\frac{i\hat{H}t}{\hbar}} \right| x_2 \right\rangle\right|^2} e^{\ln\left|\left\langle x_1 \left| e^{-\frac{\beta\hat{H}}{2}-\frac{i\hat{H}t}{\hbar}} \right| x_2 \right\rangle\right|^2} dt \tag{6.2}$$

We have numerically observed that, depending on the DSs location, there is a certain range where $C_{ff}(t) \,/\, \left|\left\langle x_1 \left| e^{-\frac{\beta\hat{H}}{2}-\frac{i\hat{H}t}{\hbar}} \right| x_2 \right\rangle\right|^2$ is a slowly varying function of time,
and $\exp\left[\ln\left|\left\langle x_1 \left| e^{-\frac{\beta\hat{H}}{2}-\frac{i\hat{H}t}{\hbar}} \right| x_2 \right\rangle\right|^2\right]$ is the fast varying part of the integrand. Under this condition we can evaluate the time integral of Eq.(6.1) by stationary phase approximation. The stationary phase prescription implies that

$$\frac{d}{dt}\ln\left|\left\langle x_1 \left| e^{-\frac{\beta\hat{H}}{2}-\frac{i\hat{H}t}{\hbar}} \right| x_2 \right\rangle\right|^2\Bigg|_{t=t_s} = 0 \tag{6.3}$$

where t_s is the time when the phase is stationary. Eq.(6.3) implies that

$$-\frac{i}{\hbar}\frac{\left\langle x_1 \left| \hat{H}e^{-\frac{\beta\hat{H}}{2}-\frac{i\hat{H}t_s}{\hbar}} \right| x_2 \right\rangle}{\left\langle x_1 \left| e^{-\frac{\beta\hat{H}}{2}-\frac{i\hat{H}t_s}{\hbar}} \right| x_2 \right\rangle} + \frac{i}{\hbar}\left(\frac{\left\langle x_1 \left| He^{-\frac{\beta\hat{H}}{2}-\frac{i\hat{H}t_s}{\hbar}} \right| x_2 \right\rangle}{\left\langle x_1 \left| e^{-\frac{\beta\hat{H}}{2}-\frac{i\hat{H}t_s}{\hbar}} \right| x_2 \right\rangle}\right)^* =$$

$$= -\frac{i}{\hbar}\left[E(\beta,t_s) - E^*(\beta,t_s)\right] =$$

$$= \frac{2}{\hbar}\mathrm{Im}\left[E(\beta,t_s)\right] = 0 \tag{6.4}$$

where we have defined

$$E(\beta,t) = \frac{\left\langle x_1 \left| \hat{H}e^{-\frac{\beta\hat{H}}{2}-\frac{i\hat{H}t}{\hbar}} \right| x_2 \right\rangle}{\left\langle x_1 \left| e^{-\frac{\beta\hat{H}}{2}-\frac{i\hat{H}t}{\hbar}} \right| x_2 \right\rangle}. \tag{6.5}$$

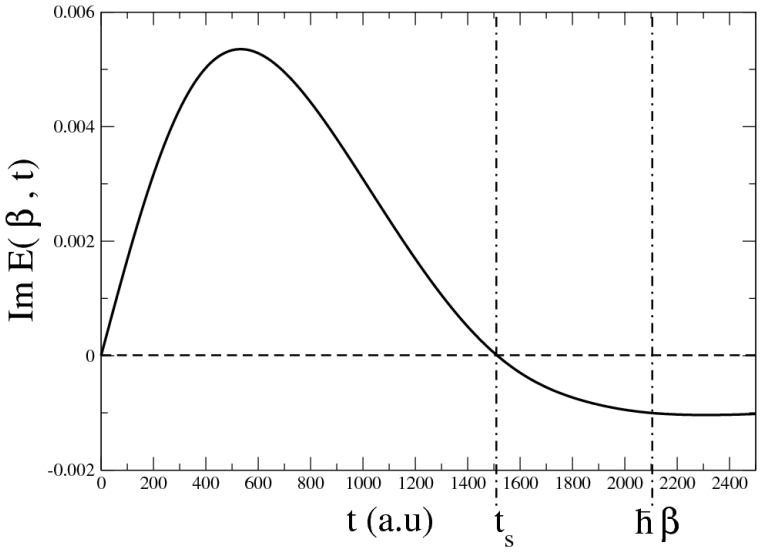

Figure 6.3: Typical plot of Im $[E(\beta, t)]$ for the Eckart barrier at 150K. The DSs are placed at 4.62 a.u. distance. The $C_{ff}(t)$ decay time $\hbar\beta$ is indicated by a vertical dash-dotted line as well as the stationary time t_s.

$E(\beta, t)$ is an odd function of time and t_s=0 is always a solution of Eq.(6.4). Therefore, independently from the system considered, there will be for all DSs positions at least one solution (t_s=0), and, if $t_s \neq 0$ is an additional stationary time, also -t_s will be a stationary point. A typical plot of Im $[E(\beta, t)]$ versus time is reported in Fig. (6.3). We can see that the DSs position can be chosen such that t_s is smaller than the flux-flux correlation function decay time, i.e. $\hbar\beta$.[42]

Now we expand the exponent in Eq. (6.2) in Taylor series up to second order around each stationary time t_s point

$$\begin{aligned}\ln\left|\left\langle x_1\left|e^{-\frac{\beta H}{2}-\frac{iHt}{\hbar}}\right|x_2\right\rangle\right|^2 \approx \ln\left|\left\langle x_1\left|e^{-\frac{\beta H}{2}-\frac{i\hat{H}t_s}{\hbar}}\right|x_2\right\rangle\right|^2 \\ +(t-t_s)\,\frac{d}{dt}\ln\left|\left\langle x_1\left|e^{-\frac{\beta H}{2}-\frac{iHt}{\hbar}}\right|x_2\right\rangle\right|^2\Big|_{t=t_s} \\ +\frac{(t-t_s)^2}{2}\,\frac{d^2}{dt^2}\ln\left|\left\langle x_1\left|e^{-\frac{\beta H}{2}-\frac{iHt}{\hbar}}\right|x_2\right\rangle\right|^2\Big|_{t=t_s}\end{aligned} \tag{6.6}$$

By defining

$$\Delta H^2(\beta, t_s) = \frac{\left\langle x_1 \left| \hat{H}^2 e^{-\frac{\beta\hat{H}}{2} - \frac{i\hat{H}t_s}{\hbar}} \right| x_2 \right\rangle}{\left\langle x_1 \left| e^{-\frac{\beta\hat{H}}{2} - \frac{i\hat{H}t_s}{\hbar}} \right| x_2 \right\rangle} - \left(\frac{\left\langle x_1 \left| \hat{H} e^{-\frac{\beta\hat{H}}{2} - \frac{i\hat{H}t_s}{\hbar}} \right| x_2 \right\rangle}{\left\langle x_1 \left| e^{-\frac{\beta\hat{H}}{2} - \frac{i\hat{H}t_s}{\hbar}} \right| x_2 \right\rangle} \right)^2 \tag{6.7}$$

and by taking the second derivative

$$\frac{d^2}{dt^2} \ln \left| \left\langle x_1 \left| e^{-\frac{\beta\hat{H}}{2} - \frac{i\hat{H}t}{\hbar}} \right| x_2 \right\rangle \right|^2 \Bigg|_{t=t_s} = -\frac{2}{\hbar^2} \mathrm{Re}\Delta H^2(\beta, t_s) \tag{6.8}$$

we evaluate the stationary-phase approximation,

$$\begin{aligned} k(T) Q_r(T) \approx & \sum_{t_s} \frac{1}{2} \int_{-\infty}^{+\infty} dt \frac{C_{ff}(t_s)}{\left| \left\langle x_1 \left| e^{-\frac{\beta H}{2} - \frac{i\hat{H}t_s}{\hbar}} \right| x_2 \right\rangle \right|^2} \\ & \times e^{\ln \left| \left\langle x_1 \left| e^{-\frac{\beta H}{2} - \frac{i\hat{H}t_s}{\hbar}} \right| x_2 \right\rangle \right|^2 + \frac{(t-t_s)^2}{2} \left[-\frac{2}{\hbar^2} \mathrm{Re}\Delta H^2(\beta, t_s) \right]} \\ = & \sum_{t_s} \frac{1}{2} \frac{C_{ff}(t_s)}{\left| \left\langle x_1 \left| e^{-\frac{\beta H}{2} - \frac{i\hat{H}t_s}{\hbar}} \right| x_2 \right\rangle \right|^2} e^{\ln \left| \left\langle x_1 \left| e^{-\frac{\beta H}{2} - \frac{i\hat{H}t_s}{\hbar}} \right| x_2 \right\rangle \right|^2} \times \\ & \int_{-\infty}^{+\infty} dt e^{-\frac{(t-t_s)^2}{\hbar^2} \mathrm{Re}\Delta H^2(\beta, t_s)} \end{aligned} \tag{6.9}$$

and after the Gaussian integration at each stationary point, we obtain

$$k(T) Q_r(T) \approx \sum_{t_s} \frac{1}{2} \frac{\hbar\sqrt{\pi}}{\sqrt{\mathrm{Re}\Delta H^2(\beta, t_s)}} C_{ff}(t_s) \tag{6.10}$$

where $C_{ff}(t_s)$ is the flux-flux correlation function value at time $t = t_s$ defined as

$$C_{ff}(t_s) = \mathrm{Tr}\left[\hat{F}_1 e^{-\frac{\beta\hat{H}}{2} + \frac{i\hat{H}t_s}{\hbar}} \hat{F}_2 e^{-\frac{\beta\hat{H}}{2} - \frac{i\hat{H}t_s}{\hbar}} \right] \tag{6.11}$$

From the symmetry considerations pointed out above, and considering that both the flux-flux correlation function and $\mathrm{Re}\Delta H^2(\beta, t_s)$ are even functions of time, we can restate Eq.(6.10) as the sum

$$
\begin{aligned}
k(T)\,Q_r(T) \approx & \frac{1}{2}\frac{\hbar\sqrt{\pi}C_{ff}(t_s=0)}{\sqrt{\mathrm{Re}\Delta H^2(\beta,t_s=0)}} \\
& + \frac{1}{2}\frac{\hbar\sqrt{\pi}C_{ff}(t_s)}{\sqrt{\mathrm{Re}\Delta H^2(\beta,t_s)}} + \frac{1}{2}\frac{\hbar\sqrt{\pi}C_{ff}(-t_s)}{\sqrt{\mathrm{Re}\Delta H^2(\beta,-t_s)}} \\
= & \frac{1}{2}\frac{\hbar\sqrt{\pi}C_{ff}(t_s=0)}{\sqrt{\mathrm{Re}\Delta H^2(\beta,t_s=0)}} + \frac{\hbar\sqrt{\pi}C_{ff}(t_s)}{\sqrt{\mathrm{Re}\Delta H^2(\beta,t_s)}}
\end{aligned}
\tag{6.12}
$$

which includes a single value of $t_s \neq 0$. Finally, recalling that we have chosen the two DSs sufficiently far apart that $C_{ff}(0)=0$, we obtain the central result of this chapter

$$
k(T)\,Q_r(T) \approx \frac{\hbar\sqrt{\pi}}{\sqrt{\mathrm{Re}\Delta H^2(\beta,t_s)}} C_{ff}(t_s) \tag{6.13}
$$

Following Miller et al.[121], Eq.(6.13) can be extended to multidimensional problems by taking

$$
\begin{aligned}
& \Delta H^2(\beta,t_s) \approx \left\langle \Delta H^2(\beta,t_s) \right\rangle = \\
& \frac{\int d\mathbf{Y_1} \int d\mathbf{Y_2} \left\langle x_1\mathbf{Y_1} \left| \hat{H}^2 e^{-\frac{\beta H}{2}-\frac{iHt_s}{\hbar}} \right| x_2\mathbf{Y_2} \right\rangle \left\langle x_1\mathbf{Y_1} \left| e^{-\frac{\beta H}{2}-\frac{iHt_s}{\hbar}} \right| x_2\mathbf{Y_2} \right\rangle}{\int d\mathbf{Y_1} \int d\mathbf{Y_2} \left(\left\langle x_1\mathbf{Y_1} \left| e^{-\frac{\beta H}{2}-\frac{iHt_s}{\hbar}} \right| x_2\mathbf{Y_2} \right\rangle \right)^2} \\
& - \frac{\int d\mathbf{Y_1} \int d\mathbf{Y_2} \left(\left\langle x_1\mathbf{Y_1} \left| \hat{H} e^{-\frac{\beta H}{2}-\frac{iHt_s}{\hbar}} \right| x_2\mathbf{Y_2} \right\rangle \right)^2}{\int d\mathbf{Y_1} \int d\mathbf{Y_2} \left(\left\langle x_1\mathbf{Y_1} \left| e^{-\frac{\beta H}{2}-\frac{iHt_s}{\hbar}} \right| x_2\mathbf{Y_2} \right\rangle \right)^2}
\end{aligned}
\tag{6.14}
$$

where the average is over the $\mathbf{Y}$ coordinates, i.e. the set of coordinates orthogonal to the reactive one at the TST location. This approximation is exact in the separable limit and it is an extension to complex time of what was previously derived for purely imaginary time.[121]

In summary, the procedure for the approximate evaluation of the thermal rate constant is first to fix the two DSs sufficiently far apart such that $C_{ff}(0)=0$. Then, find the zero of Eq.(6.4) and finally, evaluate Eq.(6.13) at the time t_s.

6.1.2 An Alternative Derivation of the Quantum Instanton Approximation

In this paragraph we show that the same procedure presented above can be employed to derive the QI expression, at least in its simplest one DS version. To

prove this, we first choose the two DSs to be the same, i.e. x_1=x_2=x_0

$$k(T)\,Q_r(T) = \frac{1}{2}\int_{-\infty}^{+\infty} dt \frac{C_{ff}(t)}{\left|\left\langle x_0 \left| e^{-\frac{\beta H}{2}-\frac{iHt}{\hbar}} \right| x_0 \right\rangle\right|^2} e^{\ln\left|\left\langle x_0 \left| e^{-\frac{\beta H}{2}-\frac{iHt}{\hbar}} \right| x_0 \right\rangle\right|^2} \tag{6.15}$$

We now remember that the QI approximation is a zero-time approximation, i.e. a proper QTST approximation, differently from Eq.(6.13). To retrieve its expression one could naively impose t=0 in Eq.(6.15), but in this way the integral is too approximated. Hence, we expand the exponent in Eq.(6.15) up to the second order around the QI stationary time t=0

$$\begin{aligned}\ln\left|\left\langle x_0 \left| e^{-\frac{\beta H}{2}-\frac{iHt}{\hbar}} \right| x_0 \right\rangle\right|^2 \simeq & \ln\left|\left\langle x_0 \left| e^{-\frac{\beta H}{2}} \right| x_0 \right\rangle\right|^2 \\ & + t\,\frac{d}{dt}\ln\left|\left\langle x_0 \left| e^{-\frac{\beta H}{2}-\frac{iHt}{\hbar}} \right| x_0 \right\rangle\right|^2\Bigg|_{t=0} \\ & + \frac{t^2}{2}\,\frac{d^2}{dt^2}\ln\left|\left\langle x_0 \left| e^{-\frac{\beta H}{2}-\frac{iHt}{\hbar}} \right| x_0 \right\rangle\right|^2\Bigg|_{t=0}\end{aligned} \tag{6.16}$$

Then, we observe that the stationary condition is always satisfied since the l.h.s of Eq.(6.16) is an even function of time and the first order term vanishes for any choice of x_0. The second derivative is given by Eq.(6.8) and we obtain

$$\begin{aligned}k(T)\,Q_r(T)^{approx}_{QI} = & \frac{1}{2}\int_{-\infty}^{+\infty} dt \frac{C_{ff}(0)}{\left|\left\langle x_0 \left| e^{-\frac{\beta H}{2}} \right| x_0 \right\rangle\right|^2} \times \\ & e^{\ln\left|\left\langle x_0 \left| e^{-\frac{\beta H}{2}} \right| x_0 \right\rangle\right|^2 + \frac{t^2}{2}\left[-\frac{2}{\hbar^2}\mathrm{Re}\Delta H^2(\beta,0)\right]} \\ = & \frac{1}{2}\frac{C_{ff}(0)}{\left|\left\langle x_0 \left| e^{-\frac{\beta H}{2}} \right| x_0 \right\rangle\right|^2} e^{\ln\left|\left\langle x_0 \left| e^{-\frac{\beta H}{2}} \right| x_0 \right\rangle\right|^2} \times \\ & \int_{-\infty}^{+\infty} dt e^{-\frac{t^2}{\hbar^2}\mathrm{Re}\Delta H^2(\beta,0)}\end{aligned} \tag{6.17}$$

We now perform the Gaussian integral and obtain the familiar QI expression[121]

$$k(T)\,Q_r(T)^{approx}_{QI} = \frac{1}{2}C_{ff}(0)\,\frac{\hbar\sqrt{\pi}}{\sqrt{\mathrm{Re}\Delta H^2(\beta,0)}} \tag{6.18}$$

where

$$\Delta H^2(\beta,0)=\frac{\left\langle x_0\left|\hat{H}^2e^{-\frac{\beta\hat{H}}{2}}\right|x_0\right\rangle}{\left\langle x_0\left|e^{-\frac{\beta\hat{H}}{2}}\right|x_0\right\rangle}-\left(\frac{\left\langle x_0\left|\hat{H}e^{-\frac{\beta\hat{H}}{2}}\right|x_0\right\rangle}{\left\langle x_0\left|e^{-\frac{\beta\hat{H}}{2}}\right|x_0\right\rangle}\right)^2 \tag{6.19}$$

The QI rate in Eq.(6.18) can be applied to any x_0 dividing surface position. However, this single stationary time formulation is more accurate when the zeroth order term $\ln\left|\left\langle x_0\left|e^{-\frac{\beta H}{2}}\right|x_0\right\rangle\right|^2$ is maximized respect to x_0, i.e. $\partial\left\langle x_0\left|e^{-\frac{\beta H}{2}}\right|x_0\right\rangle/\partial x_0=0$, which is the original QI dividing surface requirement.[121]

6.1.3 An Analytical Case: The Free Particle

In order to investigate the general high temperature limit of Eq.(6.13), we look at the free particle case. We start from the matrix elements

$$\left\langle x_1\left|e^{-\left(\frac{\beta}{2}+\frac{it}{\hbar}\right)\hat{H}}\right|x_2\right\rangle=\sqrt{\frac{m}{2\pi\hbar^2\left(\frac{\beta}{2}+\frac{it}{\hbar}\right)}}e^{-\frac{m\left(x_2-x_1\right)^2}{2\hbar^2\left(\frac{\beta}{2}+\frac{it}{\hbar}\right)}} \tag{6.20}$$

and the squared modulus of the propagator

$$\left|\left\langle x_1\left|e^{-\left(\frac{\beta}{2}+\frac{it}{\hbar}\right)\hat{H}}\right|x_2\right\rangle\right|^2=\frac{m}{2\pi\hbar\sqrt{t^2+\left(\frac{\beta\hbar}{2}\right)^2}}e^{-\frac{m\left(x_2-x_1\right)^2\beta}{2\left[t^2+\left(\frac{\beta\hbar}{2}\right)^2\right]}} \tag{6.21}$$

For the free particle and considering two distinct DSs, the flux-flux correlation function is

$$\begin{aligned}C_{ff}(t)_{fp}=&\frac{k_BT}{h}\frac{\left(\hbar\beta/2\right)^2}{\left[t^2+\left(\frac{\beta\hbar}{2}\right)^2\right]^{3/2}}\left\{1+\frac{m\beta}{\left(\hbar\beta/2\right)^2}\frac{\left(x_2-x_1\right)t^2}{\left[t^2+\left(\frac{\beta\hbar}{2}\right)^2\right]}\right\}\times\\&\exp\left\{-\frac{m\left(x_2-x_1\right)^2\beta}{2\left[t^2+\left(\frac{\beta\hbar}{2}\right)^2\right]}\right\}\end{aligned} \tag{6.22}$$

as demonstrated at the end of Appendix A.

From Eq.(6.21), the stationary phase condition (6.3) is satisfied whenever the

time variable t is such that

$$t\left\{\frac{m\left(x_2-x_1\right)^2\beta}{\left[t^2+\left(\frac{\beta\hbar}{2}\right)^2\right]^2}-\frac{1}{t^2+\left(\frac{\beta\hbar}{2}\right)^2}\right\}=0 \tag{6.23}$$

or, besides the solution $t_s = 0$, when

$$t_s=\pm\sqrt{m\left(x_2-x_1\right)^2\beta-\left(\frac{\beta\hbar}{2}\right)^2} \tag{6.24}$$

Real time condition for t_s implies that $\mathrm{m}(x_2-x_1)^2\beta > (\hbar\beta/2)^2$. This inequality provides a lower bound for the minimum distance between the DSs at temperature β, according to the least uncertainty principle. More specifically, the above inequality can be written as

$$m\left(x_2-x_1\right)^2/\beta=\Delta x^2 mk_BT=\Delta x^2m^2v^2=\Delta x^2\Delta p^2>\left(\frac{\hbar}{2}\right)^2 \tag{6.25}$$

where the equipartition theorem $k_B\mathrm{T}/2 = \mathrm{m}v^2/2$ has been employed. This criterion is also equivalent to requiring that the distance between the two surfaces has to be larger than half the thermal de Broglie wave length. The solution $t_s = 0$ does not contribute to the approximate rate. In fact, the flux-flux correlation function given in Eq.(6.22) evaluated at this time gives

$$C_{ff}\left(0\right)_{fp}=\frac{1}{\pi\hbar^2\beta^2}e^{-\frac{2m\left(x_2-x_1\right)^2}{\beta\hbar^2}} \tag{6.26}$$

and its value vanishes when taking the two DSs sufficiently distant from each other.

After evaluating

$$\left|\left\langle x_1\left|e^{-\left(\frac{\beta}{2}+\frac{it}{\hbar}\right)\hat{H}}\right|x_2\right\rangle\right|^2\Bigg|_{t=t_s}=\frac{m}{2\pi\hbar\sqrt{m\left(x_2-x_1\right)^2\beta}}e^{-\frac{1}{2}} \tag{6.27}$$

we obtain the ratio and evaluate it at t=t_s

$$\left.\frac{C_{ff}(t)_{fp}}{\left|\left\langle x_1\left|e^{-\left(\frac{\beta}{2}+\frac{it}{\hbar}\right)\hat{H}}\right|x_2\right\rangle\right|^2}\right|_{t=t_s}=\frac{1}{m\beta} \tag{6.28}$$

By evaluating the second derivative of the phase, i.e. the first derivative of the stationary condition (6.23) at t=t_s , we obtain

$$\left.\frac{d^2}{dt^2}\ln\left(\left|\left\langle x_1\left|e^{-\left(\frac{\beta}{2}+\frac{it}{\hbar}\right)\hat{H}}\right|x_2\right\rangle\right|^2\right)\right|_{t=t_s}=\frac{2\left[\left(\frac{\hbar\beta}{2}\right)^2-m(x_2-x_1)^2\beta\right]}{m^2(x_2-x_1)^4\beta^2} \tag{6.29}$$

Finally, after the Gaussian integration, we get to the approximate free particle rate

$$\begin{aligned}Q_r(T)k(T)_{fp}\approx&\frac{\sqrt{\pi}}{m\beta}\frac{me^{-1/2}}{2\pi\hbar\sqrt{m(x_2-x_1)^2\beta}}\left[-\frac{2\left(\left(\frac{\hbar\beta}{2}\right)^2-m(x_2-x_1)^2\beta\right)}{2m^2(x_2-x_1)^4\beta^2}\right]^{-1/2}\\=&\frac{k_BT}{h}\sqrt{\frac{\pi}{e}}\sqrt{\frac{m(x_2-x_1)^2\beta}{m(x_2-x_1)^2\beta-\left(\frac{\beta\hbar}{2}\right)^2}}\\=&\frac{k_BT}{h}\sqrt{\frac{\pi}{e}}\sqrt{1+\left(\frac{\hbar\beta}{2t_s}\right)^2}\end{aligned} \tag{6.30}$$

The free particle expression of Eq.(6.30) is quite accurate at high temperatures, regardless the actual position of the two DSs. In fact, for small β, $Q_r(T)k(T)_{fp}\approx(k_BT/h)\sqrt{\pi/e}$ which is quite a good approximation of the exact k_BT/h rate, since $\sqrt{\pi/e}=1.075$, and to be compared with the QI free particle limit equals to $(k_BT/h)\sqrt{\pi/2}$.[121] At low temperature the accuracy depends on the position of the DSs. However, fixing the DSs such that $t_s\sim\hbar\beta$, we obtain again a better accuracy than the QI one.

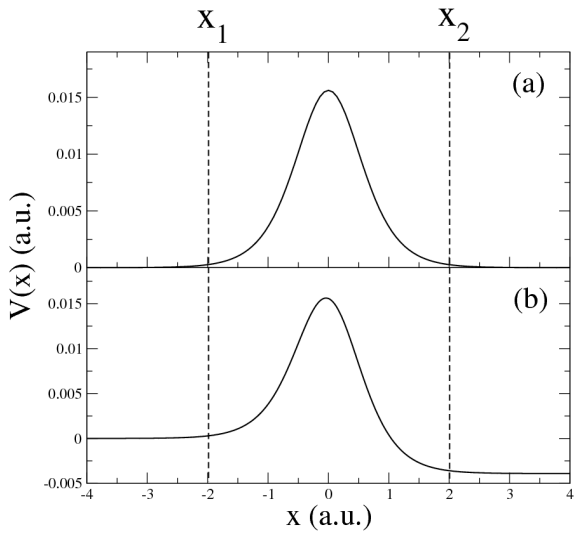

Figure 6.4: The symmetric (a) and asymmetric (b) Eckart barrier potentials. The two dashed vertical lines located at x_1 and x_2 represent possible positions of the DSs.

6.2 Results and Discussion

6.2.1 Results for the 1D Symmetric and Asymmetric Eckart Barrier

The one dimensional Eckart barrier problem is a standard test for approximate rate theories. The Eckart symmetric potential is

$$V(x) = V_0 \mathrm{sech}^2(ax) \tag{6.31}$$

and the parameters are chosen to approximately model the H + H_2 minimum energy path, i.e. V_0 = 0.425eV, a = 1.36 Bohr^{-1} and a reduced mass m = 1060m_e. Another useful one dimensional potential is the Eckart asymmetric potential, which can be regarded as a model for an heteroatomic bimolecular reaction

$$V(x) = \frac{V_0(1-\alpha)}{1+e^{-2ax}} + \frac{V_0\left(1+\sqrt{\alpha}\right)^2}{4\cosh^2(ax)} \tag{6.32}$$

In our tests we set the parameters in Eq.(6.32) as V_0=0.01562eV, a=1.3624 Bohr^{-1}, α=1.25 and m=1060m_e The potentials of Eq.s (6.31) and (6.32) are reported in Fig.(6.4). All the matrix elements needed to calculate Eq.(6.13) have been

x_1(a.u.)	x_2(a.u.)	T(K)		
		150	300	1000
-1.47	1.47	12.7%	0.8%	-3.9%
-1.75	1.75	7.0%	2.5%	-3.3%
-2.03	2.03	4.6%	3.4%	-2.8%
-2.31	2.31	0.9%	2.5%	-3.2%
-2.59	2.59	4.4%	3.4%	-1.8%
-2.87	2.87	2.0%	1.3%	-2.4%
-3.15	3.15	5.0%	2.0%	-1.2%
-3.43	3.43	1.4%	-0.5%	-1.9%

Table 6.1: Percentage error (%Err=100$\times$(k^{approx}-k^{exact})/k^{exact}) of the calculated rate constant with respect to the exact rate for the 1D symmetric Eckart potential of Eq.(6.31) at three temperatures (150K, 300K, and 1000K). x_1 and x_2 are the positions of the two DSs with respect to the top of the barrier.

evaluated by diagonalizing the Hamiltonian in a DVR representation (Sinc-DVR).[178] This approach is described in details in appendix 6.2.2. For both potential profiles, we have obtained the estimates of the thermal rate constant at several positions of the two DSs (see Tables (6.1) and (6.2)) after evaluating the stationary time t_s as shown in Fig.(6.3). Both for the symmetric and asymmetric potentials, we intentionally set the surfaces symmetrically with respect to the top of the barrier. We find that the results are just a few percentage away from the exact ones that we calculated by DVR, independently from the position of the two DSs and provided they are sufficiently far from each other. It is surprising that a symmetric DSs disposition gives accurate results even for the asymmetric potential, and comparable in accuracy to those obtained for the symmetric barrier. Furthermore, the asymmetric potential results can be improved by choosing the DSs positions in an asymmetric fashion, as shown in Table (6.3).

To better appreciate the accuracy of the present approximation (Eq.(6.13)), we compare the results of Table (6.1) with other approximate approaches for the calculation of the thermal rate constants, as shown in Table (6.4). The present approach can predict very accurate rate constants (with errors below 13%). In contrast, the RPMD,[98] the Linearized Semiclassical Initial Value Representation

x_1(a.u.)	x_2(a.u.)	T(K)		
		150	300	1000
-1.77	1.77	3.5%	2.2%	-5.2%
-2.30	2.30	-7.8%	2.4%	-4.2%
-2.83	2.83	-6.0%	0.9%	-3.4%
-3.37	3.37	-3.8%	-1.5%	-3.0%
-3.90	3.90	-3.6%	-4.1%	-2.5%
-4.43	4.43	-3.4%	-6.8%	-2.3%
-4.97	4.97	-3.3%	-9.3%	-2.1%

Table 6.2: The same as in Table (6.1) but for the asymmetric Eckart potential of Eq.(6.32).

x_2(a.u.)	x_1(a.u.)		
	-2.03	-2.50	-3.10
2.03	2.6%	2.4%	1.4%
2.50	2.2%	1.8%	0.6%
3.10	2.0%	1.2%	-0.2%
3.63	1.6%	0.4%	-1.1%
4.17	1.2%	-0.3%	-1.8%

Table 6.3: Percentage error (%Err=$100\times(k^{approx}$-$k^{exact})/k^{exact}$) of the calculated rate constant with respect to the exact rate for different choices of the DSs positions at 300K in the asymmetric Eckart barrier case. Results are reported as a function of the position x_2 of the right DS and for different settings of the left DS x_1 .

T(K)	LSC-IVR[94]	SC-VV-IVR[94]	RPMD[98]	QI[121]	HD-QI[73]	Eq.(6.13)
150K	∼-62	∼-33	-	+1.7 (-3.2)	∼+2	+12.7
200K	∼-37	∼-16	∼-45	+2.5 (-1.6)	∼-4	+10.7
300K	∼-11	∼+3	∼-25	+19.5 (+15.8)	∼+2	+3.4
1000K	∼-7	∼+3	∼-5	+21.4 (+2.5)	∼-2	-4

Table 6.4: Comparison of the percentage error (%Err=$100\times(k^{approx}$-$k^{exact})/k^{exact}$) of the thermal rate constant obtained with the present method (Eq.(6.13)) with respect to the exact value for the symmetric Eckart barrier obtained with different approximate approaches. Values deduced graphically from the cited paper are indicated by the ∼ symbol. The percentage error reported for the present method is the worst estimate obtained in Table (6.1). Free particle corrected QI results in brackets. (The acronyms meaning are Linearized Semiclassical Initial Value Representation (LSC-IVR), Semiclassical Van Vleck Initial Value Representation (SC-VV-IVR), Ring Polymer Molecular Dynamics (RPMD), QI based on Higer Derivatives of the flux-flux correlation function (HD-QI)).

(LSC-IVR),[94] and the Semiclassical van Vleck Initial Value Representation (SC-VV-IVR)[94] methods cannot retain a high accuracy for the rate estimates in the deep tunneling regime for this one dimensional case. QI is very precise at low temperatures, but looses accuracy in the high temperature limit.[121] To correct this deviation, Miller et al. introduced an *ad hoc* free particle correction reported in brackets in Table 6.4. Also, a refined QI approach that relies on the Higher Derivatives of the flux-flux correlation function (HD-QI) is better performing over the entire temperature range, but the calculation of higher flux-flux correlation function derivatives can be quite demanding and the approach difficult to be applied to more complex systems.[73] Remarkably, the new approximation of Eq.(6.13) is stable over a wide temperature range, from deep tunneling regime up to higher temperatures without any *ad hoc* correction. Furthermore, our new approach provides a reliable estimate compared to pre-existing methods even if the positions of the DSs have not been optimized.

6.2.2 Application to the H + H_2 and D + H_2 Reactions

A severe and common multidimensional test for quantum transition state theories is without any doubts the collinear H + H_2 reaction, where the amount of

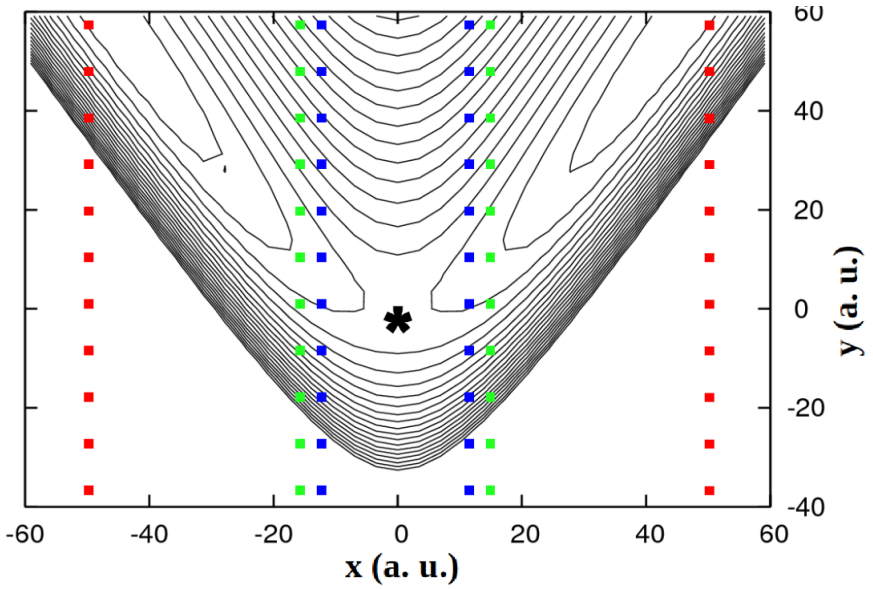

Figure 6.5: The LSTH potential energy surface plotted in mass scaled normal mode coordinates for the H + H_2 reaction. The black star represents the location of the transition state. The dotted vertical lines represent three possible positions (blue, green and red) for the two DSs.

tunneling and corner-cutting for the rate calculation is prominent. Theories based on vibrational adiabatic separation fail to correctly predict the rate for this simple bidimensional system, because of the rapid change of curvature for the potential energy surface around the saddle point.[211] For these reasons, we tested Eq.(6.13) on the collinear H + H_2 reaction. To show that we do not take advantages from any symmetry property of the potential, we apply our rate approximation also to the collinear D + H_2 reaction. We have employed the LSTH potential energy surface.[212, 213] The matrix elements of Eq.(6.13) are calculated again by DVR methods.[178] For these two dimensional cases the DSs are assumed to be straight lines and we employ mass scaled normal mode coordinates (x and y). Initially, we choose the DSs to be "vertical" surfaces defined by the equation $x = x_1$ and $x = x_2$, where x is the asymmetric stretch mass-scaled normal mode at the transition state, as depicted in Fig.(6.5). The results obtained with this setup are reported in Table (6.5).

If compared with the one dimensional cases, the results in Table (6.5) are less accurate and a stronger dependence on the DSs position can be observed. Nevertheless, the error are still limited to 60% in the worst case scenario.

150K		300K		600K		1000K	
x_2	%Err	x_2	%Err	x_2	%Err	x_2	%Err
36	-20.7	16	+33.0	9	+47.3	9	+19.6
40	-18.0	18	+2.1	12	-3.2	12	-21.7
44	-10.3	20	-8.5	15	+37.1	18	-8.3
48	-5.4	24	-23.1	21	-23.3	21	-36.9
52	-0.3	28	-31.2	24	-43.4	24	-54.3
56	+4.4	30	-30.4	27	-49.5	27	-38.8

Table 6.5: Percentage error (%Err=100$\times$(k^{approx}-k^{exact})/k^{exact}) of the new approach (Eq.(6.13)). The rate constants at four temperatures (150K, 300K, 600K, and 1000K) are reported as a function of the position of the right DS. This results are obtained with the DSs placed as in Fig.(6.5), i.e. vertically and symmetric respect to the saddle point position.

We now turn to the collinear D + H_2 reaction, where the potential in the mass scaled normal mode coordinates is asymmetric. We set the two DSs in the same fashion as done for the H + H_2, i.e. along the y-coordinate and specularly with respect to the saddle point. We find the accuracy of rate estimates is sensitive with respect to the position of the two DSs, as reported in Table (6.6). The same range of precision is found even if we try to set the two DSs in an asymmetric fashion, following the idea we applied to the one-dimensional asymmetric Eckart barrier.

T (K)	%Err (max; min)
150K	-34; - 4.1
200K	-59; -23
600K	-68; -13

Table 6.6: Worst and best percentage error (%Err=100$\times$ $\left(k^{approx} - k^{exact}\right)/k^{exact}$) of the approach (Eq.(6.13)) for the D + H_2 collinear reaction at three different temperatures. These results are obtained with the DSs positions as indicated in Fig.(6.5).

150K		300K		600K		1000K	
x_2	%Err	x_2	%Err	x_2	%Err	x_2	%Err
35	-0.9	20	-4.9	20	-1.5	9	+4.1
40	+0.4	22	-9.3	22	-2.4	12	+0.6
45	+1.8	24	-10.3	25	-7.7	15	+7.7
50	+3.4	26	-10.0	30	-7.0	18	+2.2
55	+4.0	28	-9.5	32	-4.1	21	+7.4
60	+6.1	30	-9.2	35	-3.4	24	-4.2

Table 6.7: Percentage error (%Err=100$\times$ $\left(k^{approx} - k^{exact}\right)/k^{exact}$) of the rate constant calculated with Eq.(6.13) for the collinear H + H_2 reaction at four temperatures (150K, 300K, 600K, and 1000K). The results are reported as a function of the x-coordinate intersection point between the right DS and the MEP. The DSs are always perpendicular to the MEP and symmetric respect to the x=0 axis.

At this point we observe that the idea of the stationary phase approximation of the flux-flux correlation function integral is based on a fast and a slow part of the time integration. We also consider that the reactive coordinate usually changes faster than the non-reactive ones and we conclude that a location of the DSs perpendicular to the minimum (classical) energy path (MEP) better suits the rate constant approach presented above. Thus, if we place the DSs as shown in Fig.(6.6) we obtain the results reported in Table (6.7). In this way rate constants are always within 10% of the exact ones and are almost independent of the position of the DSs. We find similar accuracy for the isotopic D + H_2 reaction, where the results are in excellent agreement with the exact value of the rate constant, even for symmetric DSs locations (see Table (6.8)). These multidimensional calculations show that the position of the DSs are close to each other at high temperatures and then they become far apart as the temperature is lowered. The explanation for this reasonable behavior is provided by reporting in Fig.(6.6) the turning points of the Semiclassical Instanton (SCI) paths. The SCI trajectories are imaginary time classical trajectories that represent the analytical continuation in imaginary time of the real time classical trajectories. Pictorially one can imagine a classical trajectory which represents the time evolution of the reactants approaching the barrier. When the trajectory energy is lower than the barrier height, instead of inverting the motion, the trajectory is continued

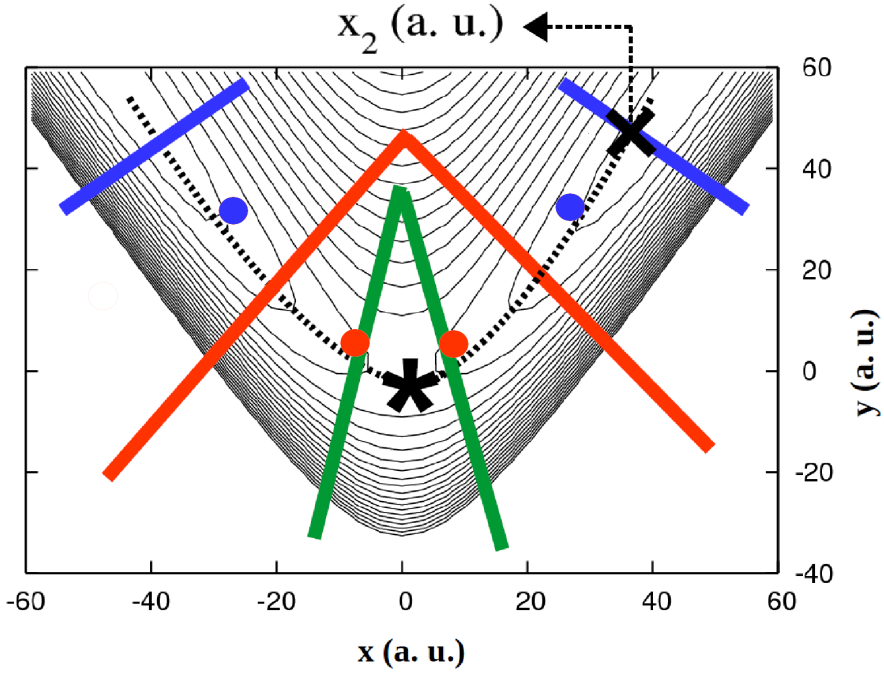

Figure 6.6: The DSs location for the LSTH potential energy surface plotted in the mass scaled normal mode coordinates for the H + H_2 system. The black star represents the position of the transition state. The potential is symmetric with respect to the transition state. The colored lines represent three possible positions (blue (150K), red (300K) and green (600K)) for the two DSs at different temperatures but always perpendicular to the MEP, which is represented by the black dashed curve. The blue and the red dots are the positions of the turning points of the Semiclassical Instanton (SCI) trajectory respectively at 150K (blue) and 300K (red).[214] The black cross indicates that the position of the DS is provided by the value of the abscissa along the MEP.

150K		300K		600K		1000K	
x_2	%Err	x_2	%Err	x_2	%Err	x_2	%Err
52	-1.8	26	-8.8	17.8	+0.6	7.5	+7.7
55	-0.1	31.2	-8.0	21.4	-0.4	9	+1.3
58.5	+1.1	36.4	-8.1	24.9	-2.2	10.5	+6.3
61.5	+1.6	41.6	-8.6	28.5	-7.9	13.5	+19.2
64.6	+1.9	46.8	-9.0	33.8	-5.5	16.5	+8.8
67.7	+2.6	52	-8.4	42.75	-6.9	18	+9.2

Table 6.8: The same as in Table (6.7) but for the collinear D + H_2 reaction.

by the instanton periodic trajectory oscillating from one turning point to the other, before continuing as a real time trajectory on the other side of the barrier into the products valley. The instanton trajectories are representative of a pure tunneling process and they can be obtained as the periodic trajectories on the inverted potential.[140] One of us has calculated these periodic trajectories at several temperatures also for the collinear H + H_2 reaction and compared them with a classical TST approach.[214] The turning points of the instanton periodic trajectories are reported in Fig.(6.6) as colored dots. As expected from the idea reported in Fig.(6.1), and according to the derivation that generates Eq.(6.13), a certain amount of real-time dynamics is calculated from the DSs to the instanton turning points. The distances along the MEP between the DSs and the same colored dot in Fig.(6.6) allow us to estimate the amount of real-time dynamics that the model foresees. Clearly already at T=600K, the instanton trajectories are not present since the rate is determined by real-time quantum dynamics, which includes quantum reflection contributions.

Finally, Table (6.9) compares the performance of the present approach to other approximate methods that have been applied to the H+H_2 collinear reaction. For instance, the Quantum Transition State Theory from Liao and Pollak (QTST),[215] and the Mixed Quantum Classical Rate Theory approach (MQCLT)[216] are very precise at high temperature, but less at low temperature. The QI approximation in its two DSs variant is very accurate, provided that a free-particle correction at high temperatures is employed. Our approximation retains a good accuracy (even if worse than the QI one) over the whole temperature range, but without any *ad hoc* correction. In conclusion, the main advantage of the present method is its simplicity and flexibility, because it does not need a precise position of the

T (K)	QTST[215]	MQCLT[216]	QI[121]	Eq.(6.10)
150K	-	-	+10	+6.1
200K	+270	+270	-4.2	-15.3
300K	+91	+29.5	+9.8	-10.3
1000K	+6	+3.6	+3	-10.9

Table 6.9: Percentage error (%Err=100$\times \left(k^{approx} - k^{exact}\right)/k^{exact}$) comparison of the thermal rate constant obtained with the present method (Eq.(6.13)) for the H + H_2 collinear reaction (all with LSTH PES) and other different approximate approaches. The values for the Qantum Instanton (QI) are obtained with two DSs. The percentage error reported for our method is for the worst case scenario we found. (The acronyms meanings are Quantum Transition State Therory (QTST), Mixed Quantum Classical rate Theory (MQCLT))

two DSs along the MEP to get accurate results that could be quite cumbersome for complex reactions. On the contrary, other methods require a preliminary optimization of the DS position.

Appendix 4.A: Derivation of the Flux Autocorrelation Function for Two Dividing Surfaces: The Parabolic Barrier and Free Particle Cases

Here we derive the expression of the flux correlation function for the parabolic barrier with two distinct dividing surfaces and that one of Eq.(6.22) by taking the limit $\omega \to 0$. We recall the matrix elements of the parabolic barrier propagator

$$\begin{aligned}\left\langle x_1 \left| e^{-i\hat{H}t_c/\hbar} \right| x_2 \right\rangle =& \sqrt{\frac{m\omega}{2\pi i\hbar \sinh\omega t_c}} \times \\ & \exp\left\{ \frac{im\omega}{2\hbar \sinh\omega t_c} \left[\left(x_1^2 + x_2^2\right) \cosh\omega t_c - 2x_1 x_2 \right] \right\}\end{aligned} \tag{6.33}$$

where $\hat{H}$ is given by Eq.(6.48), x_1 and x_2 are the dividing surface positions and $t_c = t - i\hbar\beta/2$.[42] In the following derivation we will employ the relations

$$\begin{aligned}\sinh\omega t_c &= \sinh\omega t \cos\left(u/2\right) - i\cosh\omega t \sin\left(u/2\right) \\ \cosh\omega t_c &= \cosh\omega t \cos\left(u/2\right) - i\sinh\omega t \sin\left(u/2\right)\end{aligned} \tag{6.34}$$

where $u = \hbar\omega\beta$. We start from the following expression of the flux-flux correlation function

$$\begin{aligned}C_{ff}(t) = \left(\frac{\hbar}{2m}\right)^2 \Big(& \left\langle x_2 \left| e^{-i\hat{H}t_c^*/\hbar} \right| x_1 \right\rangle \left\langle x_1 \left| e^{-i\hat{H}t_c/\hbar} \right| x_2 \right\rangle \\ & + \left\langle x_2 \left| e^{-i\hat{H}t_c^*/\hbar} \right| x_1 \right\rangle \left\langle x_1 \left| e^{-i\hat{H}t_c/\hbar} \right| x_2 \right\rangle \\ & - \left\langle x_2 \left| e^{-i\hat{H}t_c^*/\hbar} \right| x_1 \right\rangle \left\langle x_1 \left| e^{-i\hat{H}t_c/\hbar} \right| x_2 \right\rangle \\ & - \left\langle x_2 \left| e^{-i\hat{H}t_c^*/\hbar} \right| x_1 \right\rangle \left\langle x_1 \left| e^{-i\hat{H}t_c/\hbar} \right| x_2 \right\rangle \Big)\end{aligned} \tag{6.35}$$

where for example $\grave{}\left\langle x_1 \left| e^{-i\hat{H}t_c^*/\hbar} \right| x_2 \right\rangle = \partial \left\langle x_2 \left| e^{-i\hat{H}t_c^*/\hbar} \right| x_1 \right\rangle / \partial x_1$. Using Eq.(6.33), the members of Eq.(6.35) are

$$\grave{}\left\langle x_1 \left| e^{-i\hat{H}t_c/\hbar} \right| x_2 \right\rangle = \sqrt{\frac{m\omega}{2\pi i\hbar \sinh\omega t_c}} \left[\frac{im\omega}{\hbar \sinh\omega t_c} \left(x_1 \cosh\omega t_c - x_2 \right) \right] \times \exp\left(\frac{im\omega}{2\hbar \sinh\omega t_c} \left[\left(x_1^2 + x_2^2 \right) \cosh\omega t_c - 2x_1 x_2 \right] \right) \tag{6.36}$$

$$\left\langle x_1 \left| e^{-i\hat{H}t_c/\hbar} \right| x_2 \right\rangle \acute{} = \sqrt{\frac{m\omega}{2\pi i\hbar \sinh\omega t_c}} \left[\frac{im\omega}{\hbar \sinh\omega t_c} \left(x_2 \cosh\omega t_c - x_1 \right) \right] \times \exp\left(\frac{im\omega}{2\hbar \sinh\omega t_c} \left[\left(x_1^2 + x_2^2 \right) \cosh\omega t_c - 2x_1 x_2 \right] \right) \tag{6.37}$$

$$\grave{}\left\langle x_1 \left| e^{-i\hat{H}t_c/\hbar} \right| x_2 \right\rangle \acute{} = \sqrt{\frac{m\omega}{2\pi i\hbar \sinh\omega t_c}} \exp\left\{ \frac{im\omega}{2\hbar \sinh\omega t_c} \left[\left(x_1^2 + x_2^2 \right) \cosh\omega t_c - 2x_1 x_2 \right] \right\} \times \left[-\frac{im\omega}{\hbar \sinh\omega t_c} - \frac{m^2\omega^2}{\hbar^2 \left(\sinh\omega t_c \right)^2} \left(x_2 \cosh\omega t_c - x_1 \right) \left(x_1 \cosh\omega t_c - x_2 \right) \right] \tag{6.38}$$

$$\left\langle x_2 \left| e^{-i\hat{H}t_c^*/\hbar} \right| x_1 \right\rangle = \sqrt{\frac{m\omega}{-2\pi i\hbar \sinh\omega t_c^*}} \exp\left\{ -\frac{im\omega}{2\hbar \sinh\omega t_c^*} \left[\left(x_1^2 + x_2^2 \right) \cosh\omega t_c^* - 2x_1 x_2 \right] \right\} \tag{6.39}$$

$$\grave{}\left\langle x_2 \left| e^{-i\hat{H}t_c^*/\hbar} \right| x_1 \right\rangle = \sqrt{\frac{m\omega}{-2\pi i\hbar \sinh\omega t_c^*}} \left[-\frac{im\omega}{\hbar \sinh\omega t_c^*} \left(x_2 \cosh\omega t_c^* - x_1 \right) \right] \times \exp\left\{ -\frac{im\omega}{2\hbar \sinh\omega t_c^*} \left[\left(x_1^2 + x_2^2 \right) \cosh\omega t_c^* - 2x_1 x_2 \right] \right\} \tag{6.40}$$

$$\left\langle x_2 \left| e^{-i\hat{H}t_c^*/\hbar} \right| x_1 \right\rangle \acute{} = \sqrt{\frac{m\omega}{-2\pi i\hbar \sinh\omega t_c^*}} \left[-\frac{im\omega}{\hbar \sinh\omega t_c^*} \left(x_1 \cosh\omega t_c^* - x_2 \right) \right] \times \exp\left\{ -\frac{im\omega}{2\hbar \sinh\omega t_c^*} \left[\left(x_1^2 + x_2^2 \right) \cosh\omega t_c^* - 2x_1 x_2 \right] \right\} \tag{6.41}$$

$$\grave{}\left\langle x_2 \left| e^{-i\hat{H}t_c^*/\hbar} \right| x_1 \right\rangle \acute{} = \sqrt{\frac{m\omega}{-2\pi i\hbar \sinh\omega t_c^*}} \exp\left\{ \frac{im\omega}{2\hbar \sinh\omega t_c^*} \left[\left(x_1^2 + x_2^2 \right) \cosh\omega t_c - 2x_1 x_2 \right] \right\} \times \left[\frac{im\omega}{\hbar \sinh\omega t_c^*} - \frac{m^2\omega^2}{\hbar^2 \left(\sinh\omega t_c^* \right)^2} \left(x_1 \cosh\omega t_c^* - x_2 \right) \left(x_2 \cosh\omega t_c^* - x_1 \right) \right] \tag{6.42}$$

By inserting the expressions (6.33), (6.36), (6.37), (6.38), (6.39), (6.40), (6.41), and (6.42) into Eq. (6.35), we obtain

$$
\begin{aligned}
C_{ff}(t)_{pb} = & \left(\frac{\hbar}{2m}\right)^2 \frac{m\omega}{2\pi\hbar\left|\sinh\omega t_c\right|} \\
& \times \exp\left\{\frac{im\omega}{2\hbar\left|\sinh\omega t_c\right|^2}\right. \\
& \times \left[\left(x_1^2+x_2^2\right)\left(\cosh\omega t_c \sinh\omega t_c^* - \cosh\omega t_c^* \sinh\omega t_c\right)\right. && (6.43) \\
& \left.\left. +2x_1x_2\left(\sinh\omega t_c - \sinh\omega t_c^*\right)\right]\right\} && (6.44) \\
& \times \left[\frac{im\omega}{\hbar\sinh\omega t_c^*} - \frac{m^2\omega^2}{\hbar^2\left(\sinh\omega t_c^*\right)^2}\left(x_1\cosh\omega t_c^* - x_2\right)\left(x_2\cosh\omega t_c^* - x_1\right)\right. \\
& - \frac{im\omega}{\hbar\sinh\omega t_c} - \frac{m^2\omega^2}{\hbar^2\left(\sinh\omega t_c\right)^2}\left(x_2\cosh\omega t_c - x_1\right)\left(x_1\cosh\omega t_c - x_2\right) \\
& - \frac{m^2\omega^2}{\hbar^2\left|\sinh\omega t_c\right|}\left(x_1\cosh\omega t_c^* - x_2\right)\left(x_2\cosh\omega t_c - x_1\right) && (6.45) \\
& \left. - \frac{m^2\omega^2}{\hbar^2\left|\sinh\omega t_c\right|}\left(x_2\cosh\omega t_c^* - x_1\right)\left(x_1\cosh\omega t_c - x_2\right)\right] && (6.46)
\end{aligned}
$$

and using the relations Eq.(6.34), we obtain the flux-flux correlation function for the parabolic barrier

$$
\begin{aligned}
C_{ff}(t)_{pb} = & \frac{k_BT}{h}\frac{u/2}{\sin(u/2)}\frac{\omega\sin^2(u/2)\cosh\omega t}{\left(\sinh^2\omega t + \sin^2(u/2)\right)^{3/2}} \times \\
& \exp\left\{\frac{m\omega\sin(u/2)\left[2x_1x_2\cosh(\omega t) - \left(x_1^2+x_2^2\right)\cos(u/2)\right]}{2\hbar\left(\sinh^2\omega t + \sin^2(u/2)\right)}\right\} \times \\
& \left\{1 + \left(\frac{2m}{\hbar}\right)^2 \frac{\hbar}{2m\omega\cosh\omega t\sin(u/2)} \frac{\omega^2\sinh^2\omega t}{\left(\sinh^2\omega t + \sin^2(u/2)\right)} \times\right. \\
& \left.\left[\left(x_1^2+x_2^2\right)\cosh\omega t\cos(u/2) - x_1x_2\left(\cosh^2\omega t + \cos^2(u/2)\right)\right]\right\}
\end{aligned} \tag{6.47}
$$

By taking the limit of $\omega \to 0$, one obtains Eq.(6.22) for the free particle flux autocorrelation function for arbitrary dividing surface positions.

Appendix 4.B: An Analytical Case: The Parabolic Barrier

To further investigate the features of the proposed method, it is useful to consider the analytically solvable model of the one-dimensional parabolic barrier. The Hamiltonian for this system is

$$\hat{H} = \frac{\hat{p}^2}{2m} - \frac{1}{2}m\omega^2\hat{x}^2 \tag{6.48}$$

To compute the rate constant with the approximation in Eq. (6.13), one has to evaluate the expressions (6.4), (6.10) and (6.7). The matrix elements involved in these calculations are

$$\left\langle x_1 \left| e^{-\frac{\beta\hat{H}}{2}-\frac{i\hat{H}t}{\hbar}} \right| x_2 \right\rangle \tag{6.49}$$

$$\left\langle x_1 \left| \hat{H}e^{-\frac{\beta\hat{H}}{2}-\frac{i\hat{H}t}{\hbar}} \right| x_2 \right\rangle \tag{6.50}$$

$$\left\langle x_1 \left| \hat{H}^2e^{-\frac{\beta\hat{H}}{2}-\frac{i\hat{H}t}{\hbar}} \right| x_2 \right\rangle \tag{6.51}$$

By defining the complex time $\beta_c=\frac{\beta}{2}+\frac{it}{\hbar}$, the required matrix elements (6.49), (6.50), and (6.51) can be conveniently expressed in terms of β_c as partial derivatives

$$\left\langle x_1 \left| e^{-\beta_c\hat{H}} \right| x_2 \right\rangle \tag{6.52}$$

$$\left\langle x_1 \left| \hat{H}e^{-\beta_c\hat{H}} \right| x_2 \right\rangle = -\frac{\partial}{\partial\beta_c}\left\langle x_1 \left| e^{-\beta_C\hat{H}} \right| x_2 \right\rangle \tag{6.53}$$

$$\left\langle x_1 \left| \hat{H}^2e^{-\beta_c\hat{H}} \right| x_2 \right\rangle = \frac{\partial^2}{\partial\beta_c^2}\left\langle x_1 \left| e^{-\beta_C\hat{H}} \right| x_2 \right\rangle \tag{6.54}$$

In the parabolic barrier case the explicit expression for the matrix elements of the complex time propagator are known.[42] Following the definition of β_c

$$\begin{aligned}\left\langle x_1 \left| e^{-\beta_c\hat{H}} \right| x_2 \right\rangle_{pb} =& \sqrt{\frac{m\omega}{2\pi\hbar\sin(\hbar\omega\beta_c)}}\times \\ & \exp\left\{-\frac{m\omega\left[(x_2^2+x_1^2)\cos(\hbar\omega\beta_c)-2x_2x_1\right]}{2\hbar\sin(\hbar\omega\beta_c)}\right\}\end{aligned} \tag{6.55}$$

the partial derivatives in Eqs.(6.53) and (6.54) can be evaluated analytically.

$$\begin{aligned}\left\langle x_1 \left| \hat{H} e^{-\beta_c \hat{H}} \right| x_2 \right\rangle_{pb} =& \frac{\omega}{4\sin^2(\hbar\beta_c\omega)} \sqrt{\frac{m\omega}{2\pi\hbar\sin(\hbar\beta_c\omega)}} \times \\ & \left[-2m\omega\left(x_2^2 + x_1^2\right)\right. \\ & + 4m\omega x_1 x_2 \cos(\hbar\beta_c\omega) \\ & \left. +\hbar\sin(2\hbar\beta_c\omega)\right] \times \\ & \exp\left\{-\frac{m\omega}{2\hbar}\left[\left(x_2^2 + x_1^2\right)\frac{\cos(\hbar\beta_c\omega)}{\sin(\hbar\beta_c\omega)} - \frac{2x_1x_2}{\sin(\hbar\beta_c\omega)}\right]\right\}\end{aligned} \tag{6.56}$$

$$\begin{aligned}\left\langle x_1 \left| \hat{H}^2 e^{-\beta_c \hat{H}} \right| x_2 \right\rangle_{pb} =& \frac{\omega^2}{32\sin^4(\hbar\beta_c\omega)} \sqrt{\frac{m\omega}{2\pi\hbar\sin(\hbar\beta_c\omega)}} \times \\ & \left[-8\cos(2\beta_c\hbar\omega)\left(\hbar^2 - 2m^2\omega^2 x_1^2 x_2^2\right) - \hbar^2\cos(4\beta_c\hbar\omega)\right. \\ & - 32m^2\omega^2 x_1 x_2\left(x_1^2 + x_2^2\right)\cos(\beta_c\hbar\omega) \\ & - 24\hbar m\omega\left(x_1^2 + x_2^2\right)\sin(2\beta_c\hbar\omega) \\ & + 48\hbar m\omega x_1 x_2 \sin(\beta_c\hbar\omega) + 16\hbar m\omega x_1 x_2 \sin(3\beta_c\hbar\omega) \\ & \left. +9\hbar^2 + 8m^2\omega^2\left(x_1^4 + x_2^4\right) + 32m^2\omega^2 x_1^2 x_2^2\right] \times \\ & \exp\left\{-\frac{m\omega}{2\hbar}\left[\left(x_2^2 + x_1^2\right)\frac{\cos(\hbar\beta_c\omega)}{\sin(\hbar\beta_c\omega)} - \frac{2x_1x_2}{\sin(\hbar\beta_c\omega)}\right]\right\}\end{aligned} \tag{6.57}$$

In addition, the exact expression for the flux-flux correlation function for an arbitrary position of the two DSs has been derived in Eq.(6.47) of Appendix A

and by inserting it into the rate expression of Eq.(6.13), we obtain

$$
\begin{aligned}
k\left(T\right)Q_{r}\left(T\right)_{pb}^{approx} = & \frac{\hbar\sqrt{\pi}}{\sqrt{Re\Delta H^{2}\left(\beta,t_{s}\right)}}\times \\
& \exp\left\{\frac{m\omega\sin\left(\frac{\hbar\omega\beta}{2}\right)}{\hbar\left[\sinh^{2}\left(\omega t_{s}\right)+\sin^{2}\left(\frac{\hbar\omega\beta}{2}\right)\right]}\times\right. \\
& \left.\left[2x_{1}x_{2}\cosh\left(\omega t_{s}\right)-\left(x_{1}+x_{2}\right)^{2}\cos\left(\frac{\hbar\omega\beta}{2}\right)\right]\right\}\times \\
& \left\{\cosh\left(\omega t_{s}\right)\sin\left(\frac{\hbar\omega\beta}{2}\right)-\frac{2m\omega\sinh^{2}\left(t_{s}\omega\right)}{\hbar\left[\sinh^{2}\left(\omega t_{s}\right)+\sin^{2}\left(\frac{\hbar\omega\beta}{2}\right)\right]}\times\right. \\
& \left\{x_{1}x_{2}\left[\cosh^{2}\left(\omega t_{s}\right)+\cos^{2}\left(\frac{\hbar\omega\beta}{2}\right)\right]\right. \\
& \left.\left.-\left(x_{1}^{2}+x_{2}^{2}\right)\cosh\left(\omega t_{s}\right)\cos\left(\frac{\hbar\omega\beta}{2}\right)\right\}\right\}\times \\
& \frac{\omega^{2}}{4\pi\left[\sinh^{2}\left(\omega t_{s}\right)+\sin^{2}\left(\frac{\hbar\omega\beta}{2}\right)\right]^{\frac{3}{2}}}
\end{aligned}
\tag{6.58}
$$

where ΔH^{2} can also be analytically evaluated in terms of the partial derivatives (6.53), (6.54) of (6.55). Its form after writing explicitly the complex time β_{c} according to its definition is

$$
\begin{aligned}
\Delta H_{pb}^{2} = & \frac{8\hbar\omega^{2}\sin^{4}\left(\frac{\omega\beta\hbar}{2}-it\omega\right)\sin\left(\frac{\omega\beta\hbar}{2}+it\omega\right)}{\left[\cos\left(\beta\hbar\omega\right)-\cosh\left(2t\omega\right)\right]^{4}}\times \\
& \left[-2m\omega\left(x_{1}^{2}+x_{2}^{2}\right)\cos\left(\frac{\omega\beta\hbar}{2}+it\omega\right)+3m\omega x_{1}x_{2}\right. \\
& \left.+m\omega x_{1}x_{2}\cos\left(\omega\beta\hbar+i2t\omega\right)+\hbar\sin\left(\frac{\omega\beta\hbar}{2}+it\omega\right)\right]
\end{aligned}
\tag{6.59}
$$

Formula (6.58) requires to evaluate all the quantities at the stationary time t_{s}. In this case the analytical solution of Eq.(6.4) can be obtained. To accomplish this task, first we introduce three constants b, c, and d

$$
b = 4m\omega x_{1}x_{2}\sin\left(\frac{\hbar\beta\omega}{2}\right) \tag{6.60}
$$

$$c = 2 + \cos(\hbar\beta\omega) \tag{6.61}$$

$$d = \hbar - 2\hbar\cos(\hbar\beta\omega) - 4m\omega\left(x_2^2 + x_1^2\right)\sin(\hbar\beta\omega) \tag{6.62}$$

Then, Eq.(6.4) becomes

$$\begin{aligned} &-\frac{\omega\sinh(t\omega)}{4\left[\cos(\hbar\beta\omega) - \cosh(2t\omega)\right]} \times \\ &\left\{\hbar\cosh(3t\omega) + b\left[c + \cosh(2t\omega)\right] + d\cosh(t\omega)\right\} = 0 \end{aligned} \tag{6.63}$$

The solution of the Eq.(6.63) provides the time t_s for the parabolic barrier potential. A first group of solutions, independent of the position of the two DSs x_1 and x_2, arises from the first factor in Eq.(6.63)

$$\sin(\omega t_s) = 0 \Rightarrow t_s = 0 + \frac{k\pi}{\omega}, \quad k \in \mathbb{N} \tag{6.64}$$

From the second factor, after some algebra and by defining the auxiliary variable $z = \cosh(t\omega)$, we obtain a cubic equation in z

$$4\hbar z^3 + 2bz^2 + (d - 3\hbar)z - b + bc = 0 \tag{6.65}$$

Its unique real solution is

$$z = -\frac{b}{6\hbar} + \frac{\sqrt[3]{2}\left[b^2 - 3\hbar(d - 3\hbar)\right]}{6f} + \frac{\sqrt[3]{4}}{12\hbar}f \tag{6.66}$$

where the constant f is defined as

$$\begin{aligned} f = \Big\{ &-2b^3 + 9bd\hbar + 27b\hbar^2 - 54bc\hbar^2 \\ &+ \sqrt{-4\left[b^2 - 3\hbar(d - 3\hbar)\right]^3 + b^2\left[2b^2 + 9\hbar(-d - 3\hbar + 6c\hbar)\right]^2}\Big\}^{\frac{1}{3}} \end{aligned} \tag{6.67}$$

Eventually the time t_s is equal to

$$t_s = \frac{1}{\omega}\operatorname{arcosh}\left(-\frac{b}{6\hbar} + \frac{\sqrt[3]{2}\left[b^2 - 3\hbar(d - 3\hbar)\right]}{6f} + \frac{\sqrt[3]{4}}{12\hbar}f\right) \tag{6.68}$$

It is important to point out that to compute Eq.(6.71) one has to take into account the limits of applicability for the definition of the rate, i.e. that the rate must be always positive, which translates to the following relation between β

and the frequency ω

$$0 < \frac{\hbar\omega\beta}{2} < \pi \quad \Rightarrow \quad 0 < \beta < \frac{2\pi}{\hbar\omega} \tag{6.69}$$

Starting from the exact parabolic barrier rate value obtained by time integration of the flux-flux correlation function

$$k\left(T\right) Q_r\left(T\right)_{pb}^{ex} = \frac{k_B T}{h} \frac{\hbar\omega\beta}{2\sin\left(\frac{\hbar\omega\beta}{2}\right)} \tag{6.70}$$

we look at the ratio between the approximated rate of Eq.(6.58) and the exact one of Eq.(6.70)

$$\begin{aligned}
\frac{k\left(T\right) Q_r\left(T\right)_{pb}^{approx}}{k\left(T\right) Q_r\left(T\right)_{pb}^{ex}} = & \frac{\hbar\sqrt{\pi}}{\sqrt{Re\Delta H^2\left(\beta, t_s\right)}} \times \\
& \exp\left\{ \frac{m\omega\sin\left(\frac{\hbar\omega\beta}{2}\right)}{\hbar\left[\sinh^2\left(\omega t_s\right) + \sin^2\left(\frac{\hbar\omega\beta}{2}\right)\right]} \times \right. \\
& \left. \left[2x_1x_2\cosh\left(\omega t_s\right) - \left(x_1^2 + x_2^2\right)\cos\left(\frac{\hbar\omega\beta}{2}\right)\right] \right\} \times \\
& \left\{ \cosh\left(\omega t_s\right)\sin\left(\frac{\hbar\omega\beta}{2}\right) - \frac{2m\omega\sinh^2\left(t_s\omega\right)}{\hbar\left[\sinh^2\left(\omega t_s\right) + \sin^2\left(\frac{\hbar\omega\beta}{2}\right)\right]} \times \right. \\
& \left\{ x_1x_2\left[\cosh^2\left(\omega t_s\right) + \cos^2\left(\frac{\hbar\omega\beta}{2}\right)\right] \times \right. \\
& \left. \left. - \left(x_1^2 + x_2^2\right)\cosh\left(\omega t_s\right)\cos\left(\frac{\hbar\omega\beta}{2}\right) \right\} \right\} \times \\
& \frac{\omega\sin\left(\frac{\hbar\omega\beta}{2}\right)}{\left[\sinh^2\left(\omega t_s\right) + \sin^2\left(\frac{\hbar\omega\beta}{2}\right)\right]^{\frac{3}{2}}}
\end{aligned} \tag{6.71}$$

The evaluation of this ratio, as well as the calculation of the time t_s have been carried out analytically by solving Eq.(6.4).

To test the present approximation we choose the potential parameters so that the inverted parabola has a (downward) curvature which corresponds to the frequency of the H_2 molecule vibration. The mass m = 918 a.u. is equal to

T (K)	Δx^{min}(a.u.)
1300	0.44
1500	0.33
2000	0.22
2500	0.19

Table 6.10: Minimum distance between the two DSs that gives a rate constant estimate within 10% of the exact result. The two DSs are set symmetrically with respect to the top of the barrier.

the reduced mass of the H_2, and the frequency is ω=0.020056988 a.u. With these parameters the range of validity of the rate expression according to the condition (6.69) is $0 < \beta <$313.27a.u. This means we can estimate rate constants only for temperatures higher than 1007K, that is the threshold temperature when studying this model. We have investigated the outcomes of Eq.(6.71) from 1300K up to 2500K as a representative range of temperatures. When the temperature is high, the two DSs have to be set close to each other to find an acceptable value of t_s, while when decreasing the temperature the distance between the surfaces becomes larger, as summarized in Table (6.10). The approximation that we have introduced is not exact for the parabolic barrier. However, at all temperatures we have found that increasing the distance between the two DSs, the rate estimates gradually decrease until a limit to the precision of the approximate rate is reached, as depicted in Fig. (6.7).

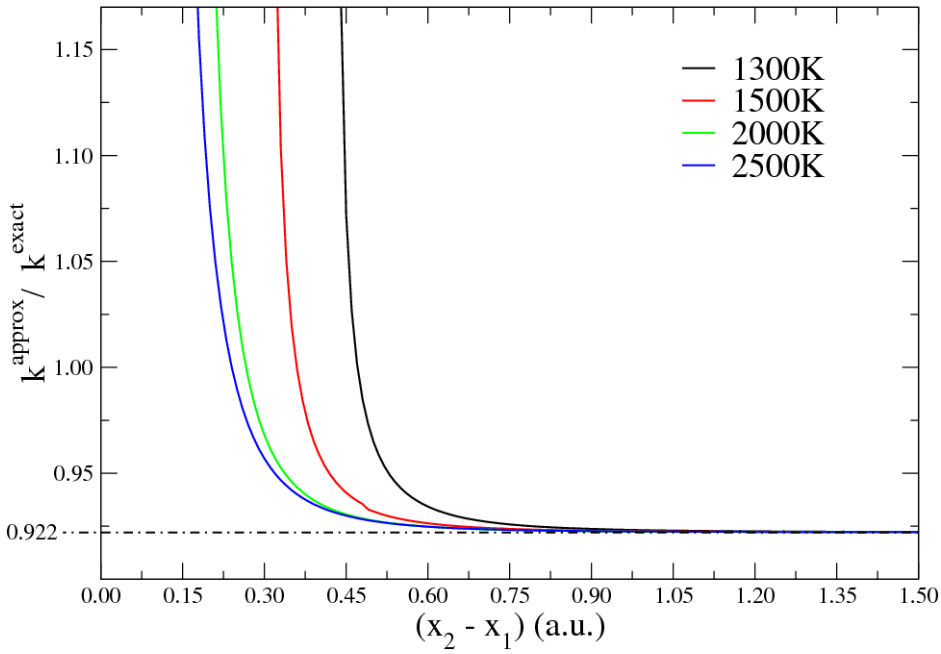

Figure 6.7: Ratio of the approximate rate constant value and the exact one for the parabolic barrier as a function of the distance between the two DSs. For all temperatures the same limit value of precision is reached.

Appendix 4.C: Discrete Variable Representation

The Discrete Variable Representation (DVR) is a pseudospectral method to compute the matrix elements of the Hamiltonian operator. In this representation the basis functions are localized around a set of points in the coordinate space. This kind of representation is not unique, but it depends on the specific form of the basis functions. According to this, there exist different kinds of DVR, such as the Gaussian quadrature DVR, Lobatto DVR,[217] and Sinc DVR[178].

The general idea is to choose a finite basis of N functions of the coordinates $\{\phi_i(\boldsymbol{q})\}_N$, and to expand the wave function $\Psi(\boldsymbol{q})$ as a linear combination of this basis functions

$$\Psi(\boldsymbol{q}) = \sum_{i=1}^{N} c_i \phi_i(\boldsymbol{q}) \tag{6.72}$$

Using this basis one can evaluate the integral that solves the time independent Schrödinger equation

$$\int_{-\infty}^{+\infty} \Psi^*(\boldsymbol{q}) \hat{H} \Psi(\boldsymbol{q}) dq = E \tag{6.73}$$

that result in finding the coefficients c_i in the expansion 6.72. These coefficients can the be employed to represent any operator, with the advantage that the representation of the Hamiltonian and of all the operators that are a function of the Hamiltonian are diagonal. It is important to select a convenient basis set that makes simple the evaluation of the integral 6.73.

More specifically, to build a DVR basis it is necessary to transform a non local orthonormal basis into another basis in which the basis functions are localized in some specific points in the coordinate space. This set of points are distributed along a chosen interval in the coordinate space and are called grid points. An early attempt to introduce these methods in quantum chemistry was done by Harris et al. in 1965,[218]. In the first one of these works, the authors developed a method to compute the matrix elements of the Hamiltonian with non trivial potential functions. The important intuition is that it is convenient to exploit the matrix representation of quantum mechanics, and using the transformation theory the following procedure can be set:

- Diagonalize the N×N matrix X that is the matrix representation of the position operator $\hat{x}$ with the unitary transformation $\boldsymbol{x} = \boldsymbol{T}^{-1}\boldsymbol{X}\boldsymbol{T}$, where $(\boldsymbol{x})_{i,j} = x_i\delta_{ij}$.
- Compute the potential $V(\boldsymbol{x})$. Since $\mathbf{x}$ is diagonal, the potential matrix is diagonal too, and it is simply built by direct evaluation of the potential at grid points, as $V(\boldsymbol{x})_{i,j} = V(x_i)\,\delta_{ij}$. This feature is really interesting, because it points out that the potential cannot be known analytically, but only as a set of discrete points.

In their paper of 1968,[219] Dickinson and Certain demonstrates that the method just described is equivalent to Gaussian quadrature when the basis is made by orthogonal polynomials, for instance Hermitte, Laguerre or Legendre polynomials. For this reason the DVR technique is indeed a quadrature method to solve numerically differential equations. Later on, in the eighties, the DVR was applied to solve concrete quantum chemistry problems, and a formal definition was given by connecting the method to variational (VBR). In the nineties, DVR techniques was largely implemented and some variations were proposed.

Sinc DVR

In this thesis we have employed the Sinc DVR, proposed for the first time by Colbert and Miller.[178] The peculiarity of this approach is the form of the basis

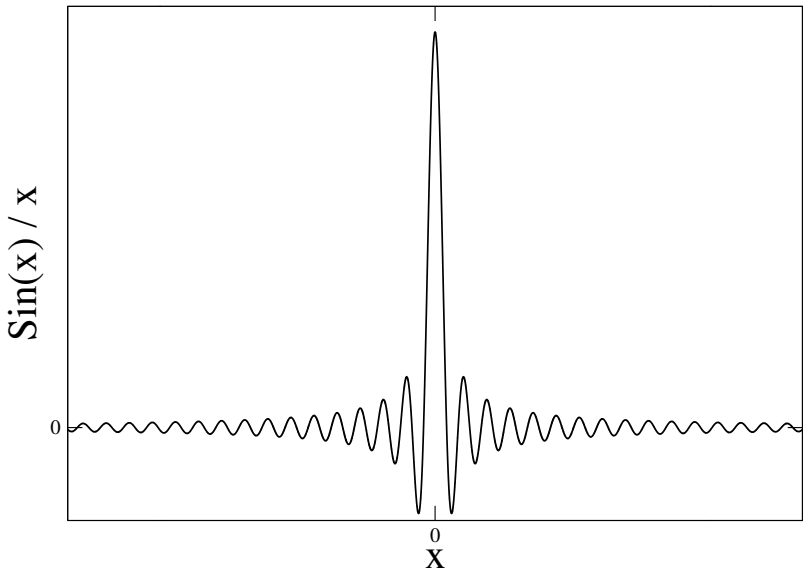

Figure 6.8: Shape of the Sinc function centered around zero. All the units are arbitrary.

functions, that are of the form

$$\text{Sinc}\,(x) = \frac{\sin\,(x)}{x} \tag{6.74}$$

The grid points are uniformly distributed along the coordinate range of interest and each one of the basis function is highly localized around a grid point, as shown in figure 6.8. Choosing this form for the basis functions gives the advantage that the kinetic energy operator can be computed analytically in a simple way.

Representation of Differential Operators

The first step is to set a grid over the coordinate region of interest. In this section we take into account a one dimensional case, but the procedure can be generalized to any dimension. The coordinate interval of our interest is $[x_{min}; x_{max}]$, and we divide it into N - 1 intervals by setting N uniformly distributed points. The j point of the grid is localized in the position

$$x_j = x_{min} + \Delta x\,(j-1) \tag{6.75}$$

where the grid interval Δx was defined as

$$\Delta x = \frac{x_{max} - x_{min}}{n-1} \tag{6.76}$$

so that the central grid point is coincident with the origin. The jth basis function $\phi_j(x)$ is defined as a Sinc function centered in the jth grid point, and it is normalized with respect to the grid interval as

$$\phi_j(x) = \frac{1}{\sqrt{\Delta x}} \frac{\sin\left[\pi\left(x - x_j\right)/\Delta x\right]}{\pi\left(x - x_j\right)/\Delta x} = \frac{1}{\sqrt{\Delta x}} \text{Sinc}\left[\pi\left(x - x_j\right)/\Delta x\right] \tag{6.77}$$

There are as many basis functions as many grid points.

This basis set can be written in Fourier representation, in fact, using the Euler's formula

$$\begin{aligned}
\phi_j(x) =& \frac{1}{\sqrt{\Delta x}} \frac{\sin\left[\pi\left(x - x_j\right)/\Delta x\right]}{\pi\left(x - x_j\right)/\Delta x} \\
=& \frac{\sqrt{\Delta x}}{2i\pi\left(x - x_j\right)} \left[e^{i\pi\left(x - x_j\right)/\Delta x} - e^{-i\pi\left(x - x_j\right)/\Delta x}\right] \\
=& \frac{\sqrt{\Delta x}}{2i\pi\left(x - x_j\right)} \int_{-\pi/\Delta x}^{\pi/\Delta x} i\left(x - x_j\right) e^{ik\left(x - x_j\right)} dk = \\
=& \frac{\sqrt{\Delta x}}{2\pi} \int_{-\pi/\Delta x}^{\pi/\Delta x} e^{ik\left(x - x_j\right)} dk
\end{aligned} \tag{6.78}$$

When the grid is set, the value of the basis function in the position x_i depends on the point where the jth basis function i centered, in fact the basis function turns out to be null at each grid points, but in the one in which it is centered

$$\phi_j(x_i) = \frac{1}{\sqrt{\Delta x}} \frac{\sin\left[\pi\left(k - j\right)\right]}{\pi\left(k - j\right)} = \frac{\delta_{kj}}{\sqrt{\Delta x}} \tag{6.79}$$

Moreover, this basis function is orthonormal. This can be shown by using the

Fourier representation of the Sinc function and equation 6.79

$$\begin{aligned}
&\int_{-\infty}^{+\infty} \phi_i^* (x)\, \phi_j (x)\, dx = \\
=&\frac{\Delta x}{(2\pi)^2} \int_{-\infty}^{+\infty} dx \int_{-\pi/\Delta x}^{\pi/\Delta x} e^{ik\left(x-x_j\right)} dk \int_{-\pi/\Delta x}^{\pi/\Delta x} e^{-ik'(x-x_i)} dk' \\
=&\frac{\Delta x}{(2\pi)^2} \int_{-\pi/\Delta x}^{\pi/\Delta x} dk \int_{-\pi/\Delta x}^{\pi/\Delta x} \left(e^{-ikx_j+ik'x_i}\right) dk' \int_{-\infty}^{+\infty} e^{ix(k-k')} dx \\
=&\frac{\Delta x}{(2\pi)^2} \int_{-\pi/\Delta x}^{\pi/\Delta x} dk \int_{-\pi/\Delta x}^{\pi/\Delta x} \left(e^{-ikx_j+ik'x_i}\right) dk' 2\pi\delta\left(k-k'\right) \\
=&\frac{\Delta x}{(2\pi)^2} \int_{-\pi/\Delta x}^{\pi/\Delta x} e^{-ik\left(x_i-x_j\right)} dk \\
=&\mathrm{Sinc}\frac{\pi\left(x_i-x_j\right)}{\Delta x} \\
=&\delta_{ij}
\end{aligned} \tag{6.80}$$

The general form of a differential operator $\frac{d^n}{dx^n}$ expressed in the Sinc basis is

$$\begin{aligned}
&\int_{-\infty}^{+\infty} \phi_i^* (x)\, \frac{d^n}{dx^n} \phi_j (x)\, dx = \\
=&\frac{\Delta x}{(2\pi)^2} \int_{-\infty}^{+\infty} dx \int_{-\pi/\Delta x}^{\pi/\Delta x} e^{-ik(x-x_i)} dk \int_{-\pi/\Delta x}^{\pi/\Delta x} \frac{d^n}{dx^n} e^{ik'\left(x-x_j\right)} dk' \\
=&\frac{\Delta x}{(2\pi)^2} \int_{-\pi/\Delta x}^{\pi/\Delta x} \int_{-\pi/\Delta x}^{\pi/\Delta x} \left(ik'\right)^n e^{ikx_i} e^{-ik'x_j} dk dk' \int_{-\infty}^{+\infty} e^{ix(k'-k)} dx \\
=&\frac{\Delta x}{2\pi} \int_{-\pi/\Delta x}^{\pi/\Delta x} e^{ikx_i} dk \int_{-\pi/\Delta x}^{\pi/\Delta x} \left(ik'\right)^n e^{-ik'x_j} \delta\left(k-k'\right) dk' \\
=&\frac{\Delta x}{2\pi} \int_{-\pi/\Delta x}^{\pi/\Delta x} e^{ik\left(x_i-x_j\right)} \left(ik'\right)^n dk \\
=&\frac{\Delta x}{2\pi} \int_{-\pi/\Delta x}^{\pi/\Delta x} \frac{d^n}{dx_i^n} e^{ik\left(x_i-x_j\right)} dk \\
=&\frac{d^n}{dx_i^n} \mathrm{Sinc}\frac{\pi\left(x_i-x_j\right)}{\Delta x}
\end{aligned} \tag{6.81}$$

In particular, when n = 1

$$\frac{d}{dx_i}\frac{\sin\left[\pi\left(x_i-x_j\right)/\Delta x\right]}{\pi\left(x_i-x_j\right)/\Delta x}=\frac{\cos\left[\pi\left(x_i-x_j\right)/\Delta x\right]}{\left(x_i-x_j\right)}-\frac{\sin\left[\pi\left(x_i-x_j\right)/\Delta x\right]}{\pi\left(x_i-x_j\right)^2/\Delta x} \tag{6.82}$$

A more compact form can be obtained distinguishing between element on the diagonal, and elements out of the diagonal. When i $\neq$ j

$$\int_{-\infty}^{+\infty}\phi_i^*(x)\frac{d}{dx}\phi_j(x)\,dx=\frac{(-1)^{i-j}}{\Delta x\,(i-j)}\qquad(i\neq j) \tag{6.83}$$

To evaluate the elements on the diagonal, one has to compute the limit of the function $\mathrm{Sinc}\frac{\pi\left(x_i-x_j\right)}{\Delta x}$ when $x_i \to x_j$. Expanding in Taylor series around x_j

$$\begin{aligned}\mathrm{Sinc}\frac{\pi\left(x_i-x_j\right)}{\Delta x}\approx&\frac{\Delta x}{\pi\left(x_i-x_j\right)}\left[\frac{\pi\left(x_i-x_j\right)}{\Delta x}-\frac{1}{3!}\frac{\pi^3\left(x_i-x_j\right)^3}{\Delta x^3}+\ldots\right]\\=&1-\frac{1}{6}\frac{\pi^2\left(x_i-x_j\right)^2}{\Delta x^2}\end{aligned} \tag{6.84}$$

and taking the derivative with respect to x_j the matrix elements out of the diagonal are

$$\int_{-\infty}^{+\infty}\phi_i^*(x)\frac{d}{dx}\phi_j(x)\,dx=-\frac{1}{3}\frac{\pi^2\left(x_i-x_j\right)}{\Delta x^2}=-\frac{1}{3}\frac{\pi^2(i-j)}{\Delta x}\qquad(i=j) \tag{6.85}$$

It is interesting to find explicitly the representation of the operator $\frac{d^2}{dx^2}$, because it appears in the kinetic part of the Hamiltonian operator. Selecting n=2, one finds

$$\begin{aligned}\frac{d^2}{dx^2}\frac{\sin\left[\pi\left(x_i-x_j\right)/\Delta x\right]}{\pi\left(x_i-x_j\right)/\Delta x}=&-\pi\frac{\sin\left[\pi\left(x_i-x_j\right)/\Delta x\right]}{\left(x_i-x_j\right)/\Delta x}\\&-2\frac{\cos\left[\pi\left(x_i-x_j\right)/\Delta x\right]}{\left(x_i-x_j\right)^2}\\&+2\frac{\sin\left[\pi\left(x_i-x_j\right)/\Delta x\right]}{\pi\left(x_i-x_j\right)^3/\Delta x}\end{aligned} \tag{6.86}$$

In this case the matrix representation is defined as

$$\begin{cases} \int_{-\infty}^{+\infty} \phi_i^*(x) \frac{d^2}{dx^2} \phi_j(x) dx = -2\frac{(-1)^{i-j}}{\Delta x(i-j)} & i \neq j \\ \int_{-\infty}^{+\infty} \phi_i^*(x) \frac{d^2}{dx^2} \phi_j(x) dx = -2\frac{(-1)^{i-j}}{\Delta x(i-j)} & i = j \end{cases} \tag{6.87}$$

Hamiltonian Operator Representation

The Hamiltonian operator is the sum of the kinetic energy operator $\hat{T}$ and of the potential operator $\hat{V}$, once the representation of these operators are known, the Hamiltonian is built as a sum of their matrix elements.

In the DVR representation the potential operator has a diagonal representation, because the position operator is diagonal.

$$\begin{aligned} \left\langle x_i \mid \hat{x} \mid x_j \right\rangle &= \int_{-\infty}^{+\infty} \left\langle x_i \mid x \right\rangle x \left\langle x \mid x_j \right\rangle dx \\ &= \int_{-\infty}^{+\infty} dx \int_{-\pi/\Delta x}^{\pi/\Delta x} \frac{\sqrt{\Delta x}}{2\pi} e^{-ik(x-x_i)} dk \int_{-\pi/\Delta x}^{\pi/\Delta x} \frac{\sqrt{\Delta x}}{2\pi} x e^{ik'\left(x-x_j\right)} dk' \\ &= \frac{\Delta x}{(2\pi)^2} \int_{-\infty}^{\infty} \int_{-\pi/\Delta x}^{\pi/\Delta x} \int_{-\pi/\Delta x}^{\pi/\Delta x} x e^{-ikx} e^{ikx_i} e^{ik'x} e^{-ik'x_j} dk dk' dx \\ &= \frac{\Delta x}{(2\pi)^2} \int_{-\pi/\Delta x}^{\pi/\Delta x} \int_{-\pi/\Delta x}^{\pi/\Delta x} e^{ikx_i} e^{-ik'x_j} dk dk' \int_{-\infty}^{\infty} x e^{ix(k'-k)} dx \\ &= \frac{\Delta x}{(2\pi)^2} \int_{-\pi/\Delta x}^{\pi/\Delta x} \int_{-\pi/\Delta x}^{\pi/\Delta x} e^{ikx_i} e^{-ik'x_j} dk dk' \frac{d}{d(ik')} \delta\left(k'-k\right) \\ &= \frac{\Delta x}{(2\pi)^2} \int_{-\pi/\Delta x}^{\pi/\Delta x} e^{-ik'x_j} dk' \frac{d}{d(ik')} \int_{-\pi/\Delta x}^{\pi/\Delta x} e^{ikx_i} \delta\left(k'-k\right) dk \\ &= \frac{\Delta x}{(2\pi)^2} x_i \int_{-\pi/\Delta x}^{\pi/\Delta x} e^{-ik'\left(x_i-x_j\right)} dk' \\ &= x_i \mathrm{Sinc}\left[\pi\left(x_i-x_j\right)/\Delta x\right] \\ &= x_i \delta_{ij} \end{aligned} \tag{6.88}$$

Finally the potential operator matrix elements are simply

$$\int_{-\infty}^{\infty} \phi_i^*(x) V(x) \phi_j(x) dx = V(x_i) \delta_{ij} \tag{6.89}$$

The kinetic energy operator matrix elements are easily found, on the basis of

equations 6.87

$$T_{ij} = \frac{\hbar^2 (-1)^{i-j}}{2m\Delta x^2} \begin{Bmatrix} \frac{\pi^2}{3} & i = j \\ \frac{2}{(i-j)^2} & i \neq j \end{Bmatrix} \tag{6.90}$$

Representation of a Generic Operator

At this stage it is possible to solve the eigenvalue equation for the eigenstates of the Hamiltonian by diagonalizing the matrix representation of the Hamiltonian operator obtained so far. The diagonalization provides the N eigenvalues and the N×N matrix of the coefficients of the eigenvector, in the sense that the ith column is the set of coefficients for the jth basis function, whose linear combination gives the ith Hamiltonian eigenfunction $\Psi_i(x) = \sum_{j=1}^{n} C_{ji}\phi_j(x)$. It is possible to compute the value of the ith eigenfunctions at each of the l points of the grid as

$$\Psi_i(x_l) = \sum_j C_{ji}\phi_j(x_l) = \sum_j C_{ji}\frac{\delta_{ij}}{\sqrt{\Delta x}} = \frac{C_{li}}{\sqrt{\Delta x}} \tag{6.91}$$

The coordinate representation of a generic operator $\hat{A}$ in the Sinc DVR representation becomes

$$\begin{aligned} \left\langle x_i \left| \hat{A} \right| x_j \right\rangle &= \sum_{kl} \left\langle x_i \left| \phi_k \right\rangle A_{kl} \left\langle \phi_l \right| x_j \right\rangle \\ &= \sum_{kl} \phi_k(x_i)\, \phi_l^*(x_j)\, A_{kl} \\ &= \frac{1}{\Delta x} \sum_{kl} C_{ik} C_{jl}^* A_{kl} \end{aligned} \tag{6.92}$$

In particular, the representation of the Boltzmann operator is even simpler, in fact its eigenvectors are also eigenvectors of the Hamiltonian operator, thus

$$\left\langle x_i \left| e^{-\beta\hat{H}} \right| x_j \right\rangle = \frac{1}{\Delta x} \sum_k C_{ik} C_{jk} e^{-\beta E_k} \tag{6.93}$$

7 Conclusions and Future Perspectives

In this thesis two open problems in reaction rate theory have been addressed. The first one is how to extend to high dimensional systems the inclusion of quantum effects and anharmonicities in rate constant computations. The aim of this project was to look for a practical method that assure enhanced accuracy with respect to standard TST method, while maintaining low computational overhead. A method with this characteristics can be useful for practical applications such as kinetic modeling in combustion chemistry, atmospheric chemistry and even synthetic organic chemistry. In contrast, the second issue faced concerns very accurate rate constants calculations. The goal of this work have been to elaborate a quantum rate expression that goes beyond the TST approximation. This expression includes in a convenient way the contribution of real time dynamics to the rate.

Dealing with the first issue, we chose to adopt the Miller's Semicalssical Transition State Theory (SCTST) approach,[38, 39] because its implementation based on VPT2 was promising for extending its applicability to high dimensional systems, provided a smart implementation was designed. To start with, chapter 4 have introduced a computational approach for the calculation of the vibrational density of states of molecular systems. To exploit the possibility of calculations on parallel architectures and open up the possibility to calculate the density of states and the partition function of high dimensional systems, we have adapted a WL algorithm parallelization strategy.[171] After describing in details the implementation of the algorithm (see 4.3) that we call ParADenSum, we have tested it on a common ground with other codes and assessed its accuracy. We have then applied the new code to real molecules and examined its computational speed-up and efficiency. We have found ParADenSum able to exhibit almost ideal efficiency and to be significantly advantageous with respect to other codes commonly employed to deal with high dimensional systems. Remarkably, in the case of naphtalene, ParADenSum exhibits a super-scalability trend. Furthermore, we have also shown that the same algorithm can be exploited to compute semiclassical reaction rate constants. For this purpose, starting from ParADenSum implementation, we have developed the code ParSCTST. To prove that our parallel implementation can actually deal with high dimensional systems, we

are applying the ParADenSum and the ParSCTST programs to compute the SCTST rate constant of the isomerization of the the 2,4,6-tri-tert-butylphenyl to 3,5-di-tert-butyleneophyl. This problem is challenging for two reasons. First the system includes 135 fully coupled vibrational degrees of freedom. Secondly, this isomerization reaction is a proton transfer reaction and tunneling is known to play a crucial role. In conclusion, we believe that the method described in chapter 4 is an important and useful tool for the physical chemists community. The ParADenSum code alone provides the fully coupled anharmonic vibrational density of states that is ubiquitous and of paramount importance in physical chemistry applications. Moreover, the same code in combination with ParSCTST program provides a robust and computationally optimized implementation of SCTST. To foster widespread diffusion and application of ParADenSum, the code is freely available upon request to the authors[220] and it is officially distributed along with the MultiWell suite of codes since 2016 version.[204, 120] The same is foreseen also for ParSCTST program.

The description of how we have addressed the second problem of providing a rate constant expression that goes beyond TST is the topic of chapter 6. To achieve this goal the quantum propagator has to be evaluated at both real and imaginary times, and one of the principal challenges was to find a method that allows for a single time evaluation of the propagator, instead of a complete time evolution. This task is difficult considering that the reaction flux widely oscillates between positive and negative values that almost cancel out. Using the formalism of the flux-flux correlation function for the exact quantum rate formulation, we performed a stationary phase approximation to the time integration after extrapolating the rapidly changing part of the integrand. In this way, we have obtained the rate expression (6.13), which is the central result of this work.[221] Furthermore, the goal was also to get to a formulation able to provide accurate estimates without need for a preliminary optimization of the DSs positions. We have demonstrated that Eq.(6.13) includes this feature by applying this single time approximation to well-known one- and bi-dimensional systems, both symmetric and asymmetric, where the substantial quantum effects are mainly responsible for the thermal rate constant behavior. We found that the new formula of equation (6.13) is quite accurate over the entire range of temperatures tested, despite the fact that we do not introduce any *ad hoc* correction. We verified that the method accounts well for the "corner cutting" observed in the collinear hydrogen exchange reaction at low temperatures. Furthermore, for all systems presented, the accuracy of the results are smoothly dependent on the DSs locations. This is important when dealing with complex (high dimensional) systems, since it is not known *a priori* where the DSs can be more conveniently placed. The high

accuracy of the methods holds as long as the DSs are set sufficiently far apart so that the flux-flux correlation function is zero at time zero. This is a necessary condition for applying the stationary phase approximation, as explained in paragraph 6.1.1. However, the method presents some limitations. For instance, opposite to classical TST and some semiclassical theories,[48] this approximation is not a strict upper bound to the exact quantum rate, as it is often the case for QTSTs. Also, the better accuracy for the rate calculation respect to QTST methods, is obtained at the cost of performing real-time quantum dynamics. Future developments will include the possibility to avoid the DVR calculation of the propagator and perform the calculation of the real-time part via semiclassical dynamics. This will introduce a further approximation, since the semiclassical propagator is known to be not suitable in the deep tunneling regime. However, it is quite accurate for the calculation of shallow tunneling and quantum reflection contributions to the rate constant. This foreseen implementation will allow to calculate the thermal rate constant directly from classical trajectories and without any preliminary Monte Carlo or variational search for best placement of the DSs. We believe that the present approximation will become very useful when real-time quantum effects are determinant and important for the rate calculation in complex reactions.

Bibliography

[1] Steinfeld, J. I.; Francisco, J. S.; Hase, W. L. *Chemical kinetics and dynamics*, Vol. 3; Prentice Hall Englewood Cliffs (New Jersey), 1989.

[2] Eyring, H. *The Journal of Chemical Physics* **1936**, *4*(4), 283–291.

[3] Malatesta, L.; Cenini, S. In *Principi di chimica generale, con esrcizi;* Casa Editrice Abrosiana (Milano), 1972; pages 94–97.

[4] Tannor, D. J. *Introduction to quantum mechanics: a time-dependent perspective;* University Science Books, 2007.

[5] Miller, W. H. *The Journal of Physical Chemistry A* **1998**, *102*(5), 793–806.

[6] Hartke, B.; Manz, J. *Journal of the American Chemical Society* **1988**, *110*(10), 3063–3068.

[7] Kosloff, R. *The Journal of Physical Chemistry* **1988**, *92*(8), 2087–2100.

[8] Karplus, M.; Porter, R.; Sharma, R. *The Journal of Chemical Physics* **1965**, *43*(9), 3259–3287.

[9] Bowman, J. M.; Schatz, G. C. *Annual review of physical chemistry* **1995**, *46*(1), 169–196.

[10] Miller, W. H. *The Journal of Chemical Physics* **1970**, *53*(9), 3578–3587.

[11] Miller, W. H.; George, T. F. *The Journal of Chemical Physics* **1972**, *56*(11), 5668–5681.

[12] Levit, S.; Smilansky, U. *Annals of Physics* **1977**, *108*(1), 165–197.

[13] Herman, M. F.; Kluk, E. *Chemical Physics* **1984**, *91*(1), 27–34.

[14] Herman, M. F. *The Journal of chemical physics* **1986**, *85*(4), 2069–2076.

[15] Kluk, E.; Herman, M. F.; Davis, H. L. *The Journal of chemical physics* **1986**, *84*(1), 326–334.

[16] Heller, E. J. *The Journal of chemical physics* **1991**, *94*(4), 2723–2729.

[17] Miller, W. H. *The Journal of chemical physics* **1991**, *95*(12), 9428–9430.

[18] Heller, E. *The Journal of Chemical Physics* **1991**, *95*(12), 9431–9432.

[19] Sepúlveda, M.-A.; Tomsovic, S.; Heller, E. *Physical review letters* **1992**, *69*(3), 402.

[20] Kay, K. G. *The Journal of chemical physics* **1994**, *100*(6), 4377–4392.

[21] Kay, K. G. *The Journal of chemical physics* **1994**, *100*(6), 4432–4445.

[22] Kay, K. G. *The Journal of chemical physics* **1994**, *101*(3), 2250–2260.

[23] Sepúlveda, M. A.; Heller, E. J. *The Journal of chemical physics* **1994**, *101*(9), 8004–8015.

[24] Sepúlveda, M. A.; Grossmann, F. *Advances in Chemical Physics, Volume 96* **1996**, pages 191–304.

[25] Herman, M. F. *Chemical physics letters* **1997**, *275*(5-6), 445–452.

[26] Guerin, B. E.; Herman, M. F. *Chemical physics letters* **1998**, *286*(5), 361–368.

[27] Grossmann, F.; Xavier, A. L. *Phys. Lett. A* **1998**, *243*(5), 243–248.

[28] Grossmann, F. *Comments At. Mol. Phys.* **1999**, *34*, 141–160.

[29] Harabati, C.; Rost, J. M.; Grossmann, F. *J. Chem. Phys.* **2004**, *120*, 26–30.

[30] Grossmann, F. *J. Chem. Phys.* **2006**, *125*(1).

[31] Goletz, C.-M.; Grossmann, F. *J. Chem. Phys.* **2009**, *130*(24), 244107.

[32] Buchholz, M.; Goletz, C.-M.; Grossmann, F.; Schmidt, B.; Heyda, J.; Jungwirth, P. *J. Phys. Chem. A* **2012**, *116*(46), 11199–11210.

[33] Arrhenius, S. *Z. Phys. Chem* **1889**, *4*, 226–248.

[34] Polanyi, M.; Wigner, E. *Zeitschrift für Physikalische Chemie* **1928**, *139*(1), 439–452.

[35] Eyring, H. *The Journal of Chemical Physics* **1935**, *3*(2), 107–115.

[36] Bowman, J. M.; Shepler, B. C. *Annual Review of Physical Chemistry* **2011**, *62*(1), 531–553.

[37] Bowman, J. M. *Molecular Physics* **2014**, *112*(19), 2516–2528.

[38] Miller, W. H. *The Journal of Chemical Physics* **1975**, *62*(5), 1899–1906.

[39] Hernandez, R.; Miller, W. H. *Chemical Physics Letters* **1993**, *214*(2), 129–136.

[40] Barker, J. R. *International Journal of Chemical Kinetics* **2001**, *33*(4), 232–245.

[41] Multiwell program suite, version 2014.1 b; university of michigan: Ann arbor, mi, us, 2014. Barker, J.; Ortiz, N.; Preses, J.; Lohr, L.; Maranzana, A.; Stimac, P.; Nguyen, T.; Kumar, T.

[42] Miller, W. H.; Schwartz, S. D.; Tromp, J. W. *The Journal of chemical physics* **1983**, *79*(10), 4889–4898.

[43] Chandler, D. In *Introduction to Modern Statistical Mechanics;* Oxford University Press, 1987; pages 242–243.

[44] Chandler, D. *Classical and Quantum Dynamics in Condensed Phase Simulations* **1998**, *523*.

[45] Chandler, D. *Introduction to Modern Statistical Mechanics;* Oxford University Press, 1987.

[46] Chandler, D. *Journal of Statistical Physics* **1986**, *42*(1), 49–67.

[47] Wigner, E. *The Journal of Chemical Physics* **1937**, *5*(9), 720–725.

[48] Truhlar, D. G.; Garrett, B. C. *Accounts of Chemical Research* **1980**, *13*(12), 440–448.

[49] Welsch, R.; Manthe, U. *The Journal of chemical physics* **2015**, *142*(6), 064309.

[50] Communication: Mode specific quantum dynamics of the f+ chd3â hf+ cd3 reaction. Qi, J.; Song, H.; Yang, M.; Palma, J.; Manthe, U.; Guo, H. **2016**.

[51] Pollak, E.; Talkner, P. *Chaos: An Interdisciplinary Journal of Nonlinear Science* **2005**, *15*(2), 026116.

[52] Miller, W. H. *The Journal of Chemical Physics* **1974**, *61*(5), 1823–1834.

[53] McLafferty, F. J.; Pechukas, P. *Chemical Physics Letters* **1974**, *27*(4), 511–514.

[54] Schiff, L. In *Quantum Mechanics;* McGraw-Hill, 1955; pages 22–24; International series in pure and applied physics.

[55] Meyer, H.-D.; Manthe, U.; Cederbaum, L. S. *Chemical Physics Letters* **1990**, *165*(1), 73–78.

[56] Manthe, U.; Matzkies, F. *Chemical physics letters* **1998**, *282*(5), 442–449.

[57] Matzkies, F.; Manthe, U. *The Journal of chemical physics* **1998**, *108*(12), 4828–4836.

[58] Huarte-Larrañaga, F.; Manthe, U. *The Journal of Physical Chemistry A* **2001**, *105*(12), 2522–2529.

[59] Topaler, M.; Makri, N. *The Journal of chemical physics* **1994**, *101*(9), 7500–7519.

[60] Wright, N. J.; Makri, N. *The Journal of chemical physics* **2003**, *119*(3), 1634–1642.

[61] Topaler, M.; Makri, N. *Chemical physics letters* **1993**, *210*(1), 285–293.

[62] Liu, J.; Miller, W. H. *The Journal of chemical physics* **2007**, *127*(11), 114506.

[63] Thoss, M.; Wang, H.; Miller, W. H. *The Journal of Chemical Physics* **2001**, *115*(7), 2991–3005.

[64] Wang, H.; Thoss, M.; Sorge, K. L.; Gelabert, R.; Giménez, X.; Miller, W. H. *The Journal of Chemical Physics* **2001**, *114*(6), 2562–2571.

[65] Wang, H.; Thoss, M.; Miller, W. H. *The Journal of Chemical Physics* **2000**, *112*(1), 47–55.

[66] Miller III, T. F.; Manolopoulos, D. E. *The Journal of chemical physics* **2005**, *122*(18), 184503.

[67] Pollak, E. *The Journal of chemical physics* **2007**, *127*(7), 074505.

[68] Li, H.; Poulsen, J. A.; Nyman, G. *The Journal of Physical Chemistry A* **2011**, *115*(25), 7338–7345.

[69] Miller, W. H. *Faraday Discussions* **1998**, *110*, 1–21.

[70] Makri, N. *Annual review of physical chemistry* **1999**, *50*(1), 167–191.

[71] Nakayama, A.; Makri, N. *The Journal of chemical physics* **2003**, *119*(16), 8592–8605.

[72] Liu, J.; Miller, W. H. *The Journal of chemical physics* **2007**, *126*(23), 234110.

[73] Ceotto, M.; Yang, S.; Miller, W. H. *The Journal of chemical physics* **2005**, *122*(4), 044109.

[74] Yamamoto, T.; Wang, H.; Miller, W. H. *The Journal of chemical physics* **2002**, *116*(17), 7335–7349.

[75] Tromp, J. W.; Miller, W. H. *Faraday Discussions of the Chemical Society* **1987**, *84*, 441–453.

[76] Sim, E.; Krilov, G.; Berne, B. *The Journal of Physical Chemistry A* **2001**, *105*(12), 2824–2833.

[77] Bonella, S.; Monteferrante, M.; Pierleoni, C.; Ciccotti, G. *The Journal of chemical physics* **2010**, *133*(16), 164104.

[78] Shi, Q.; Geva, E. *The Journal of Physical Chemistry A* **2004**, *108*(29), 6109–6116.

[79] Craig, I. R.; Manolopoulos, D. E. *The Journal of chemical physics* **2005**, *122*(8), 084106.

[80] Pollak, E.; Martin-Fierro, E. *The Journal of chemical physics* **2007**, *126*(16), 164107.

[81] Martin-Fierro, E.; Pollak, E. *The Journal of chemical physics* **2006**, *125*(16), 164104.

[82] Zhu, W.; Zhao, Y. *The Journal of chemical physics* **2008**, *129*(18), 184111.

[83] Bonella, S.; Montemayor, D.; Coker, D. F. *Proceedings of the National Academy of Sciences of the United States of America* **2005**, *102*(19), 6715–6719.

[84] Markovic, N.; Poulsen, J. A. *The Journal of Physical Chemistry A* **2008**, *112*(8), 1701–1711.

[85] Poulsen, J. A.; Nyman, G.; Rossky, P. J. *The Journal of chemical physics* **2003**, *119*(23), 12179–12193.

[86] Poulsen, J. A.; Li, H.; Nyman, G. *The Journal of chemical physics* **2009**, *131*(2), 024117.

[87] Huaqing, L.; Poulsen, J.; Nyman, G. *The Journal of Physical Chemistry Letters* **2013**, *4*(17), 3013–3018.

[88] Kaledin, A. L.; Miller, W. H. *J. Chem. Phys.* **2003**, *118*(16), 7174–7182.

[89] Kaledin, A. L.; Miller, W. H. **2003**, *119*(6), 3078–3084.

[90] Ceotto, M.; Dell'Angelo, D.; Tantardini, G. F. *The Journal of chemical physics* **2010**, *133*(5), 054701.

[91] Conte, R.; Aspuru-Guzik, A.; Ceotto, M. *The journal of physical chemistry letters* **2013**, *4*(20), 3407–3412.

[92] Gabas, F.; Conte, R.; Ceotto, M. *J. Chem. Theory Comput.* **2017**, *13*, 2378.

[93] Ceotto, M.; Di Liberto, G.; Conte, R. *Phys. Rev. Lett.* **2017**, *119*(1), 010401.

[94] Venkataraman, C.; Miller, W. H. *The Journal of chemical physics* **2007**, *126*(9), 094104.

[95] Yamamoto, T.; Miller, W. H. *The Journal of chemical physics* **2004**, *120*(7), 3086–3099.

[96] Miller, W. H. *The Journal of Physical Chemistry A* **1999**, *103*(47), 9384–9387.

[97] Craig, I. R.; Manolopoulos, D. E. *The Journal of chemical physics* **2004**, *121*(8), 3368–3373.

[98] Craig, I. R.; Manolopoulos, D. E. *The Journal of chemical physics* **2005**, *122*(8), 084106.

[99] Richardson, J. O.; Althorpe, S. C. *The Journal of chemical physics* **2009**, *131*(21), 214106.

[100] Hele, T. J.; Althorpe, S. C. *The Journal of chemical physics* **2013**, *138*(8), 084108.

[101] Althorpe, S. C.; Hele, T. J. *The Journal of chemical physics* **2013**, *139*(8), 084115.

[102] Cao, J.; Voth, G. A. *The Journal of chemical physics* **1994**, *100*(7), 5093–5105.

[103] Geva, E.; Shi, Q.; Voth, G. A. *The Journal of Chemical Physics* **2001**, *115*(20), 9209–9222.

[104] Shi, Q.; Geva, E. *The Journal of chemical physics* **2003**, *119*(17), 9030–9046.

[105] Habershon, S.; Manolopoulos, D. E.; Markland, T. E.; III, T. F. M. *Annual Review of Physical Chemistry* **2013**, *64*(1), 387–413.

[106] Yamamoto, T.; Miller, W. H. *The Journal of chemical physics* **2005**, *122*(4), 044106.

[107] Ceperley, D. M. *Reviews of Modern Physics* **1995**, *67*(2), 279.

[108] Mandrà, S.; Schrier, J.; Ceotto, M. *The Journal of Physical Chemistry A* **2014**, *118*(33), 6457–6465.

[109] Mandrà, S.; Valleau, S.; Ceotto, M. *International Journal of Quantum Chemistry* **2013**, *113*(12), 1722–1734.

[110] Tromp, J. W.; Miller, W. H. *Faraday Discussions of the Chemical Society* **1987**, *84*, 441–453.

[111] Gallicchio, E.; Egorov, S.; Berne, B. *The Journal of chemical physics* **1998**, *109*(18), 7745–7755.

[112] Rabani, E.; Krilov, G.; Berne, B. *The Journal of Chemical Physics* **2000**, *112*(6), 2605–2614.

[113] Yamashita, K.; Miller, W. H. *The Journal of chemical physics* **1985**, *82*(12), 5475–5484.

[114] Ankerhold, J.; Grossmann, F.; Tannor, D. J. *Physical Chemistry Chemical Physics* **1999**, *1*(6), 1333–1342.

[115] Marcus, D. M. W. R. *Chemical Physics Letters* **1984**, *110*.

[116] Wadi, H.; Pollak, E. *The Journal of chemical physics* **1999**, *110*(17), 8246–8253.

[117] Miller, W. H. *Journal of the American Chemical Society* **1979**, *101*(23), 6810–6814.

[118] Nguyen, T. L.; Stanton, J. F.; Barker, J. R. *The Journal of Physical Chemistry A* **2011**, *115*(20), 5118–5126.

[119] Greene, S. M.; Shan, X.; Clary, D. C. *The Journal of Physical Chemistry A* **2015**, *119*(50), 12015–12027.

[120] Aieta, C.; Gabas, F.; Ceotto, M. *The Journal of Physical Chemistry A* **2016**, *120*(27), 4853–4862.

[121] Miller, W. H.; Zhao, Y.; Ceotto, M.; Yang, S. *The Journal of chemical physics* **2003**, *119*(3), 1329–1342.

[122] Ceotto, M.; Miller, W. H. *The Journal of chemical physics* **2004**, *120*(14), 6356–6362.

[123] Karandashev, K.; Vaníček, J. *The Journal of chemical physics* **2015**, *143*(19), 194104.

[124] Zhao, Y.; Yamamoto, T.; Miller, W. H. *The Journal of chemical physics* **2004**, *120*(7), 3100–3107.

[125] Buchowiecki, M.; Vaníček, J. *The Journal of chemical physics* **2010**, *132*(19), 194106.

[126] Wang, W.; Zhao, Y. *The Journal of chemical physics* **2010**, *132*(6), 064502.

[127] Wang, W.; Zhao, Y. *The Journal of chemical physics* **2009**, *130*(11), 114708.

[128] Vaníček, J.; Miller, W. H.; Castillo, J. F.; Aoiz, F. J. *The Journal of chemical physics* **2005**, *123*(5), 054108.

[129] Vaníček, J.; Miller, W. H. *The Journal of chemical physics* **2007**, *127*(11), 114309.

[130] Huang, J.; Buchowiecki, M.; Nagy, T.; Vaníček, J.; Meuwly, M. *Physical Chemistry Chemical Physics* **2014**, *16*(1), 204–211.

[131] Zimmermann, T.; Vaníček, J. *The Journal of chemical physics* **2009**, *131*(2), 024111.

[132] Buchowiecki, M.; Vaníček, J. *Chemical Physics Letters* **2013**, *588*, 11–16.

[133] Chandler, D. In *Introduction to Modern Statistical Mechanics;* Oxford University Press, 1987; pages 252–255.

[134] Wigner, E. *Zeitschrift für Physikalische Chemie* **1932**, *19*(1), 203–216.

[135] Eckart, C. *Physical Review* **1930**, *35*(11), 1303.

[136] Schatz, G. C.; Ratner, M. A. *Quantum mechanics in chemistry;* Courier Corporation, 1993.

[137] Bell, R. P. *Transactions of the Faraday Society* **1959**, *55*.

[138] Skodje, R. T.; Truhlar, D. G. *The Journal of Physical Chemistry* **1981**, *85*(6), 624–628.

[139] Miller, W. H. *The Journal of Chemical Physics* **1974**, *61*(5), 1823–1834.

[140] Miller, W. H. *The Journal of chemical physics* **1975**, *62*(5), 1899–1906.

[141] Miller, W. H. *Faraday Discussions of the Chemical Society* **1977**, *62*, 40–46.

[142] Stanton, J. F. *The journal of physical chemistry letters* **2016**, *7*(14), 2708–2713.

[143] Stanton, J.; Gauss, J.; Harding, M.; Szalay, P.; Auer, A.; Bartlett, R.; Benedikt, U.; Berger, C.; Bernholdt, D.; Bomble, Y.; others. *For the current version, see http://www. cfour. de* **2009**.

[144] Barone, V. *The Journal of chemical physics* **2005**, *122*(1), 014108.

[145] Gaussian 09, revision d. 01. Frisch, M.; Trucks, G.; Schlegel, H. B.; Scuseria, G.; Robb, M.; Cheeseman, J.; Scalmani, G.; Barone, V.; Mennucci, B.; Petersson, G.; others. **2009**.

[146] Chapman, S.; Garrett, B. C.; Miller, W. H. *The Journal of Chemical Physics* **1975**, *63*(6), 2710–2716.

[147] Miller, W. H. *Accounts of Chemical Research* **1976**, *9*(8), 306–312.

[148] Nordholm, S.; Freasier, B.; Jolly, D. *Chemical Physics* **1977**, *25*(3), 433–449.

[149] Freasier, B.; Jolly, D.; Nordholm, S. *Chemical Physics* **1978**, *32*(2), 161–168.

[150] Lenzer, T.; Luther, K.; Nilsson, D.; Nordholm, S. *The Journal of Physical Chemistry B* **2005**, *109*(17), 8325–8331.

[151] Houston, P. L.; Conte, R.; Bowman, J. M. *The Journal of Physical Chemistry A* **2014**, *118*(36), 7758–7775.

[152] Houston, P. L.; Conte, R.; Bowman, J. M. *The Journal of Physical Chemistry A* **2015**, *119*(20), 4695–4710.

[153] Beyer, T.; Swinehart, D. *Communications of the ACM* **1973**, *16*(6), 379.

[154] Stein, S. E.; Rabinovitch, B. *The Journal of Chemical Physics* **1973**, *58*(6), 2438–2445.

[155] Hüpper, B.; Pollak, E. *The Journal of chemical physics* **1999**, *110*(23), 11176–11186.

[156] Forst, W. *Theory of unimolecular reactions;* Elsevier, 2012.

[157] Forst, W. *Unimolecular reactions: a concise introduction;* Cambridge University Press, 2003.

[158] Parneix, P.; Van-Oanh, N.-T.; Bréchignac, P. *Chemical physics letters* **2002**, *357*(1), 78–84.

[159] Börjesson, L.; Nordholm, S.; Andersson, L. L. *Chemical physics letters* **1991**, *186*(1), 65–72.

[160] Krems, R.; Nordholm, S. *Zeitschrift für Physikalische Chemie* **2000**, *214*(11/2000), 1467.

[161] Isaacson, A. D.; Truhlar, D. G.; Scanlon, K.; Overend, J. *The Journal of Chemical Physics* **1981**, *75*(6), 3017–3024.

[162] Truhlar, D. G.; Isaacson, A. D. *The Journal of chemical physics* **1991**, *94*(1), 357–359.

[163] Barker, J. R. *Journal of Physical Chemistry* **1987**, *91*(14), 3849–3854.

[164] Toselli, B. M.; Barker, J. R. *Chemical physics letters* **1989**, *159*(5-6), 499–504.

[165] Noid, D.; Koszykowski, M.; Tabor, M.; Marcus, R. *The Journal of Chemical Physics* **1980**, *72*(11), 6169–6175.

[166] Farantos, S.; Murrell, J.; Hajduk, J. *Chemical Physics* **1982**, *68*(1-2), 109–117.

[167] Basire, M.; Parneix, P.; Calvo, F. *The Journal of Chemical Physics* **2008**, *129*(8), 081101.

[168] Nguyen, T. L.; Barker, J. R. *The Journal of Physical Chemistry A* **2010**, *114*(10), 3718–3730.

[169] Wang, F.; Landau, D. *Physical review letters* **2001**, *86*(10), 2050.

[170] Wang, F.; Landau, D. *Physical Review E* **2001**, *64*(5), 056101.

[171] Vogel, T.; Li, Y. W.; Wüst, T.; Landau, D. P. *Physical review letters* **2013**, *110*(21), 210603.

[172] Yin, J.; Landau, D. *Computer Physics Communications* **2012**, *183*(8), 1568–1573.

[173] Poulain, P.; Calvo, F.; Antoine, R.; Broyer, M.; Dugourd, P. *Physical Review E* **2006**, *73*(5), 056704.

[174] Valentim, A.; Rocha, J. C.; Tsai, S.-H.; Li, Y. W.; Eisenbach, M.; Fiore, C. E.; Landau, D. P. In *Journal of Physics: Conference Series*, Vol. 640, page 012006. IOP Publishing, 2015.

[175] Pattanasiri, B.; Li, Y. W.; Wust, T.; Landau, D. P. In *Journal of Physics: Conference Series*, Vol. 640, page 012015. IOP Publishing, 2015.

[176] Shi, G.; Wuest, T.; Li, Y. W.; Landau, D. P. In *Journal of Physics: Conference Series*, Vol. 640, page 012017. IOP Publishing, 2015.

[177] Koh, Y. W.; Sim, A. Y.; Lee, H. K. *Physical Review E* **2015**, *92*(2), 023306.

[178] Colbert, D. T.; Miller, W. H. *The Journal of chemical physics* **1992**, *96*(3), 1982–1991.

[179] Multidimensional quantum dynamics: Mctdh theory and applications. Huarte-Larrañaga, F.; Manthe, U. **2009**.

[180] Manthe, U. *The Journal of chemical physics* **2015**, *142*(24), 244109.

[181] Miller, W. H. *The Journal of Physical Chemistry A* **2001**, *105*(13), 2942–2955.

[182] Miller, W. H. *Proceedings of the National Academy of Sciences of the United States of America* **2005**, *102*(19), 6660–6664.

[183] Conte, R.; Pollak, E. *Physical Review E* **2010**, *81*(3), 036704.

[184] Kay, K. G. *Annu. Rev. Phys. Chem.* **2005**, *56*, 255–280.

[185] Tamascelli, D.; Dambrosio, F. S.; Conte, R.; Ceotto, M. *The Journal of chemical physics* **2014**, *140*(17), 174109.

[186] Zhuang, Y.; Siebert, M. R.; Hase, W. L.; Kay, K. G.; Ceotto, M. *Journal of chemical theory and computation* **2012**, *9*(1), 54–64.

[187] Šulc, M.; Vaníček, J. *Molecular Physics* **2012**, *110*(9-10), 945–955.

[188] Conte, R.; Pollak, E. *The Journal of chemical physics* **2012**, *136*(9), 094101.

[189] Santoro, F.; Cappelli, C.; Barone, V. *Journal of chemical theory and computation* **2011**, *7*(6), 1824–1839.

[190] Zhou, C.; Bhatt, R. *Physical Review E* **2005**, *72*(2), 025701.

[191] Landau, D.; Tsai, S.-H.; Exler, M. *American Journal of Physics* **2004**, *72*(10), 1294–1302.

[192] Nguyen, T. L.; Stanton, J. F.; Barker, J. R. *Chemical Physics Letters* **2010**, *499*(1), 9–15.

[193] Clary, D. C. *The Journal of chemical physics* **1991**, *95*(10), 7298–7310.

[194] Bell, R. P. *The tunnel effect in chemistry;* Springer, 2013.

[195] Brunton, G.; Griller, D.; Barclay, L.; Ingold, K. *Journal of the American Chemical Society* **1976**, *98*(22), 6803–6811.

[196] Meisner, J.; Markmeyer, M. N.; Bohner, M. U.; Kästner, J. *Physical Chemistry Chemical Physics* **2017**, *19*(34), 23085–23094.

[197] Steinfeld, J. I.; Francisco, J. S.; Hase, W. L. In *Chemical kinetics and dynamics;* Prentice Hall Englewood Cliffs (New Jersey), 1989; Vol. 3; pages 94–97.

[198] D'amore, L.; Laccetti, G.; Murli, A. *ACM Transactions on Mathematical Software (TOMS)* **1999**, *25*(3), 306–315.

[199] Holbrook, K. A.; Pilling, M. J.; Robertson, S. H. *Unimolecular reactions;* Wiley, 1996.

[200] Robinson, P. J.; Holbrook, K. A. *Unimolecular reactions;* Wiley-Interscience New York, 1972.

[201] Whitten, G.; Rabinovitch, B. *The Journal of Chemical Physics* **1963**, *38*(10), 2466–2473.

[202] Whitten, G.; Rabinovitch, B. *The Journal of Chemical Physics* **1964**, *41*(6), 1883–1883.

[203] Benedict, W.; Gailar, N.; Plyler, E. K. *The Journal of Chemical Physics* **1956**, *24*(6), 1139–1165.

[204] Multiwell-2017 software suite. J.R. Barker, T.L. Nguyen, J.F. Stanton, C. Aieta, M. Ceotto, F. Gabas, T.J.D. Kumar, C.G.L. Li, L.L. Lohr, A. Maranzana, N.F. Ortiz, J.M. Preses, J.M. Simmie, J.A. Sonk, and P.J. Stimac, University of Michigan, Ann Arbor, Michigan, USA, 2016. http://clasp-research.engin.umich.edu/multiwell/.

[205] Wigner, E. *Transactions of the Faraday Society* **1938**, *34*, 29–41.

[206] Truhlar, D. G.; Garrett, B. C.; Klippenstein, S. J. *The Journal of physical chemistry* **1996**, *100*(31), 12771–12800.

[207] Houston, P.; Kable, S. *Proceedings of the National Academy of Sciences* **2006**, *103*(44), 16079–16082.

[208] Townsend, D.; Lahankar, S.; Lee, S.; Chambreau, S.; Suits, A.; Zhang, X.; Rheinecker, J.; Harding, L.; Bowman, J. *Science* **2004**, *306*(5699), 1158–1161.

[209] Bowman, J. M. *Proceedings of the National Academy of Sciences* **2006**, *103*(44), 16061–16062.

[210] Bao, J. L.; Sripa, P.; Truhlar, D. G. *Phys. Chem. Chem. Phys.* **2016**, *18*, 1032–1041.

[211] Baer, M. *Theory of chemical reaction dynamics*, Vol. 3; CRC, 1985.

[212] Siegbahn, P.; Liu, B. *The Journal of Chemical Physics* **1978**, *68*(5), 2457–2465.

[213] Truhlar, D. G.; Horowitz, C. J. *The Journal of Chemical Physics* **1978**, *68*(5), 2466–2476.

[214] Ceotto, M. *Molecular Physics* **2012**, *110*(9-10), 547–559.

[215] Liao, J.-L.; Pollak, E. *The Journal of Physical Chemistry A* **2000**, *104*(9), 1799–1803.

[216] Zheng, Y.; Pollak, E. *The Journal of Chemical Physics* **2001**, *114*(22), 9741–9746.

[217] Manolopoulos, D.; Wyatt, R. *Chemical physics letters* **1988**, *152*(1), 23–32.

[218] Harris, D. O.; Engerholm, G. G.; Gwinn, W. D. *The Journal of Chemical Physics* **1965**, *43*(5), 1515–1517.

[219] Dickinson, A.; Certain, P. *The Journal of Chemical Physics* **1968**, *49*(9), 4209–4211.

[220] Ceotto group website. `http://users.unimi.it/ceotto/`.

[221] Aieta, C.; Ceotto, M. *The Journal of Chemical Physics* **2017**, *146*(21), 214115.

UNIVERSITÀ DEGLI STUDI DI MILANO
DIPARTIMENTO DI CHIMICA

Ph.D. ACTIVITY REPORT

- ***Ph.D. student:*** Chiara Donatella Aieta
- ***Program:*** Scuola di Dottorato in Chimica
- ***Cycle:*** XXX, ***Program Term:*** 1st November 2014 – 31st October 2017
- ***Tutor:*** Prof. Michele Ceotto

Thesis Title

Quantum and Semiclassical Methods for Rate Constant Calculations

Description of performed research

During my Ph.D. course I have been working mainly on the development of new methods for the calculation of reaction rate constants with inclusion of quantum effects. The research activity I have performed is here summarized. It can be divided in four Projects. In particular, Projects 1-3 are discussed in detail in the thesis.

In the first and second year I have built a parallel robust implementation of W. H. Miller's Semi-classical Transition State Theory (SCTST), which provides reaction rate constants that include nuclear tunneling corrections and anharmonicity effects.[1] The novelty of my new implementation is that it can be employed to study high dimensional systems. SCTST requires the calculation of two quantities. One is the reactant partition function, the other one is the cumulative reaction probability at the transition state. For this reason the work has been organized in two projects. Eventually, my code has been inserted into the MultiWell suite of programs.[2] MultiWell main developer is Prof. J. R. Barker at University of Michigan, who has become a major collaborator.

In **Project 1** I have developed a new parallel implementation of the Wang-Landau algorithm (WL),[3] a special Monte Carlo (MC) procedure to calculate the reactant vibrational density of states, from which the partition function is readily determined. I have successfully applied my code (called ParADenSum) to fully coupled anharmonic systems. The parallelization strategy consisted in dividing the investigated energy range into windows and in performing the calculation of the vibrational density of states for each window on a single processor (Figure 1). This strategy was suggested by the observation that fewer random sampling events and reduced computational effort are needed for the MC convergence in a restricted energy range. I have tested the accuracy of the ParADenSum code on several molecular systems, including some benchmarks for which an exact evaluation of the vibrational density of states is doable by direct counting (Figure 2). ParADenSum can easily handle 150 vibrational degrees of freedom, and a significant computational speedup has been found when applying the code to molecules up to 66 vibrational degrees of freedom (Figure 3). These features make ParADenSum a very promising tool. The results of this first project have been published at the beginning of the second year as a research paper,[4] and presented in June 2016 at the international workshop "Different Routes to Quantum Molecular Dynamics" held at CECAM-HQ, EPFL, Lausanne, Switzerland. The

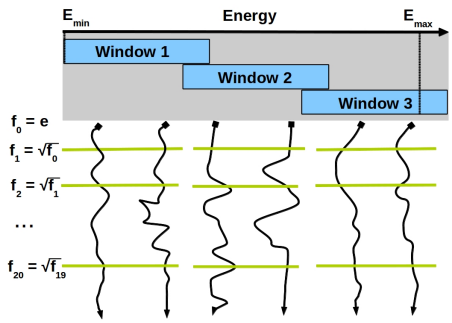

Figure 1: Work-flow of the ParADenSum code. The energy range is divided into windows. Independent random walks (black arrows) are performed in each window and their estimate of the density of states is averaged out after each of the 21 iterations (green lines). Every iteration is halted according to a user-provided parameter called flatness criterion.

ParADenSum code is now freely available upon request and it is implemented in the latest 2016 version of the MultiWell suite of codes and I am now an official developer of the program suite (http://clasp-research.engin.umich.edu/multiwell/index.php).

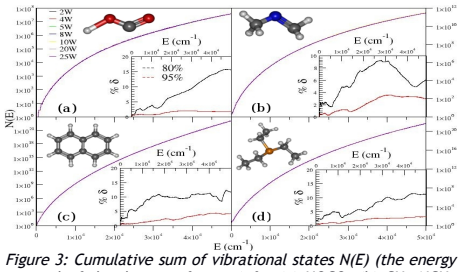

Figure 3: Cumulative sum of vibrational states N(E) (the energy integral of the density of states) for (a) HOCO, (b) CH_2=NCH_3, (c) $C_{10}H_8$, (d) $P(Et)_3$. The curves computed with different number of windows are one over the other. The inset shows the percentage standard deviation over the average of 10 runs changing flatness criterion from 80% (black) to 95% (red).

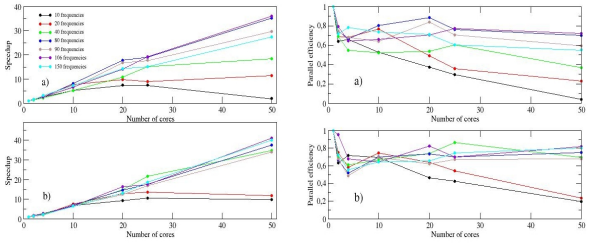

Figure 2: Parallel performance of the ParADenSum codes with system of increasing number of vibrational degrees of freedom. (a) 80% and (b) 95% flatness convergence criterion.

In **Project 2**, which has been mainly developed during the third year, I have further contributed to MultiWell development by extending my parallel implementation to the computation of cumulative reaction probabilities at the transition state, a code I have named parSCTST. Combining the partition function computed with ParADenSum and the cumulative reaction probabilities calculated with ParSCTST, the SCTST rate is readily obtained. Application of the method to calculate the rate constant associated to the isomerization of the Aryl radical is in progress (Figure 4).[5] This problem is challenging because the system includes 135 fully coupled vibrational degrees of freedom, anharmonicity must be taken into account, and tunneling is known to play a crucial role due to the proton transfer mechanism which characterizes the reaction.[6]

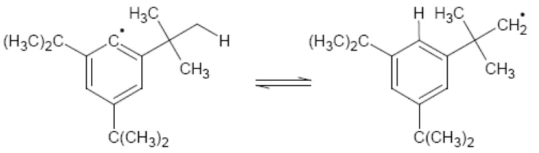

Figure 4: The isomerization reaction of the 2,4,6-tri-tert-butylphenyl to 3,5-di-tert-butyleneophyl is a proton transfer reaction.

A second line of research, that I have addressed during the second and third year, concerns the design and testing of a new method for very accurate quantum rate constants calculations (**Project 3**). An exact formulation for quantum reaction rates is know in principle, but the application of such theory to real system is hampered by the huge computational effort required, and reliable approximate approaches are needed. The new method I have developed is based on the Quantum Instanton theory of W. H. Miller (QI).[7] The QI method has many convenient features. First, it is very accurate from deep tunneling regime up to high temperatures and it works well for both symmetric and asymmetric potentials. Secondly, the only quantity which has to be evaluated is the Boltzmann operator (and its beta derivatives) that can be efficiently calculated by means of well known imaginary time path integral techniques even when dealing with high dimensional systems. Conversely, the QI method has two main drawbacks, i.e. the need for optimizing the position of two dividing surfaces and the fact that it is a purely imaginary time formulation, which means it can be inserted in the group of Transition State Theory (TST) approaches. The aim of my work was to overcome these limitations. In fact, the new rate expression I have derived is very slightly dependent on the position of the two dividing surfaces. Furthermore, it goes beyond the basic TST approximation by including the contribution of real time dynamics.

Computing the exact thermal rate constant requires the evaluation of the flux-flux correlation function integral[8]

$$k\left(T\right)Q_r\left(T\right)=\int_0^\infty dtC_{ff}\left(t\right) \qquad \text{(Equation 1)}$$

where

$$C_{ff}\left(t\right)=Tr\left[\hat{F}_1e^{-\frac{\beta\hat{H}}{2}+\frac{i\hat{H}t}{\hbar}}\hat{F}_2e^{-\frac{\beta\hat{H}}{2}-\frac{i\hat{H}t}{\hbar}}\right] \qquad \text{(Equation 2)}$$

The evaluation of the trace of Equation 2 is computationally demanding for high dimensional systems, and, in addition, one has to compute its value many times to solve numerically the integral. To derive an approximate expression from Equation 1, it is possible to employ a steepest descent approximation. This approximation is based on the observation that the main contribution to an integral of an exponential function, whose exponent is some function f(t), comes from the global minimum f(t_0). In fact, the integral of Equation 1 may be rewritten in the equivalent form

$$k\left(T\right)Q_r\left(T\right)=\frac{1}{2}\int_{-\infty}^{+\infty}dt\frac{C_{ff}\left(t\right)}{\left|\left\langle x_1\left|e^{-\frac{\beta\hat{H}}{2}-\frac{i\hat{H}t}{\hbar}}\right|x_2\right\rangle\right|^2}e^{\ln\left|\left\langle x_1\left|e^{-\frac{\beta\hat{H}}{2}-\frac{i\hat{H}t}{\hbar}}\right|x_2\right\rangle\right|^2} \qquad \text{(Equation 3)}$$

and then the steepest descent approximation is applied. The minimum of the function at the exponent is found by solving the following time-dependent equation

$$\Im\left[\frac{\left\langle x_1\left|\hat{H}e^{-\frac{\beta\hat{H}}{2}-\frac{i\hat{H}t}{\hbar}}\right|x_2\right\rangle}{\left\langle x_1\left|e^{-\frac{\beta\hat{H}}{2}-\frac{i\hat{H}t}{\hbar}}\right|x_2\right\rangle}\right]=0 \qquad \text{(Equation 4)}$$

At the special time t_0 (a solution of the Equation 4) the integral in Equation 3 becomes a Gaussian integral that can be solved analytically giving the new approximate rate expression

$$k\left(T\right)Q_r\left(T\right)=\frac{\hbar\sqrt{\pi}}{\sqrt{\mathrm{Re}\left[\Delta H^2\left(\beta,t_0\right)\right]}}C_{ff}\left(t_0\right) \qquad \text{(Equation 5)}$$

where

$$\Delta H^2\left(\beta,t_0\right)=\frac{\left\langle x_1\left|\hat{H}^2e^{-\frac{\beta\hat{H}}{2}-\frac{i\hat{H}t_0}{\hbar}}\right|x_2\right\rangle}{\left\langle x_1\left|e^{-\frac{\beta\hat{H}}{2}-\frac{i\hat{H}t_0}{\hbar}}\right|x_2\right\rangle}-\left(\frac{\left\langle x_1\left|\hat{H}e^{-\frac{\beta\hat{H}}{2}-\frac{i\hat{H}t_0}{\hbar}}\right|x_2\right\rangle}{\left\langle x_1\left|e^{-\frac{\beta\hat{H}}{2}-\frac{i\hat{H}t_0}{\hbar}}\right|x_2\right\rangle}\right)^2 \qquad \text{(Equation 6)}$$

The main feature of this approximate expression is that it requires just a single evaluation at the special time t_0, and so it is much cheaper to evaluate than the exact formula. The form of the equation is very close to the one of the QI, but here real time dynamics is taken into account too. The derivation has been presented in one dimension for clarity, but it has been generalized to multidimensional systems. I have tested this method against 1D and 2D model systems. These one and two dimensional cases are simpler from the point of view of the numerical effort, but they are challenging because tunneling and recrossing are very significant in these systems. The Eckart barrier is a standard test for rate theories, and the new approximation performance is reported in Figure 5. Selecting some special values of the

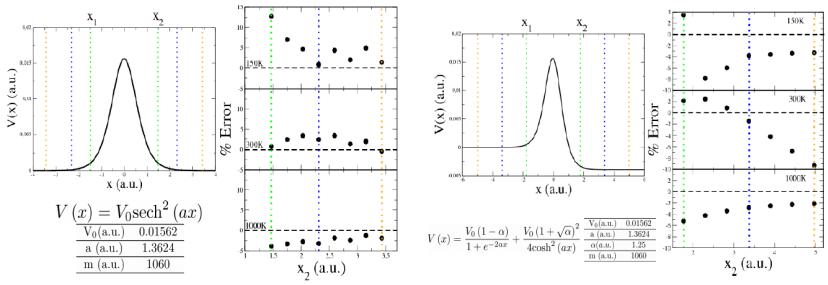

Figure 5: Percentage error of the rate constants obtained with the new method against the exact quantum mechanical results at different temperatures. The results have a small dependence on the position of the dividing surfaces. In the left panel the symmetric Eckart potential is tested, while the asymmetric Eckart potential is reported in the right panel.

parameters the symmetric barrier can model the potential for the H + H_2 collinear reaction (Figure 5, left panel), while the asymmetric one is a model for the D + H_2 reaction (Figure 5, right panel). In both test cases the reaction rate estimates are in excellent agreement with the exact value, with only a 10% range of error at all temperatures. Another important feature is the weak dependence of the accuracy of the result with respect to the position of the two dividing surfaces, which makes this method simpler to apply in the case of reactions for which the position of the transition state is unknown. Furthermore, these results are of comparable accuracy with other well established approximate methods, and they are stable over a wider temperature range, as reported in Table 1.

Sym. Eckart (% Err)	RPMD[8]	QI[6]	New Method
150 K	-	~ 2	≤ 10
300 K	~ 25	~ 20	≤ 5
1000 K	~ 5	~ 20	≤ 5

Table 1: Comparison of percentage errors on the reaction rate with respect to exact quantum mechanical results of the presented new method and other existing approaches for the symmetric Eckart barrier. RPMD stands for Ring Polymer Molecular Dynamics.[5]

As a 2D test case we chose to investigate the LSTH potential energy surface for the collinear H + H_2 reaction and its isotopic analog D + H_2. In this case (Figure 6) we found that rate constant estimates are still within 10% with respect to exact values for both reactive systems. Even in this case the position of the two dividing surfaces has low impact on the accuracy of the results.

The comparison with other methods (Table 2) is very encouraging given the fact that many of them cannot even find a reasonable rate estimate at low temperature, where quantum effects are more important.

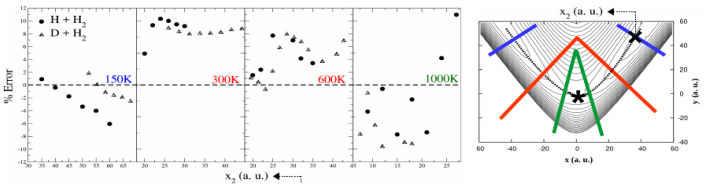

Figure 6: In the left panel the percentage error of the rate constants obtained with the new method is reported against exact quantum mechanical results at different temperatures. Results barely depend on the position of the dividing surfaces. In the right panel the collinear H+H_2 LSTH potential is depicted. The black star represents the saddle point position, while the black dotted line is the minimum energy path. The colored lines indicate the preferred position of the dividing surfaces at different temperature conditions.

The outcomes of project 3 have been published as a research paper.[10] The proceeding and final results have also been presented at four international meetings as poster communication, as well as a contributed talk at the workshop "Different Routes to Quantum Molecular Dynamics", Lausanne, Switzerland, 2016. This work has also been selected for a "lightning presentation" at the Faraday Discussion "Reaction Rate Theory: Faraday Discussion", Cambridge, United Kingdom, 2016.

Collinear H+H_2 (% Err)	QTST[9]	RPMD[8]	QI[6]	New Method
150 K	-	-	~ 1.25	≤ 6.2
300 K	91	19	~ 10	≤ 10.3
1000 K	6	16	~ 3	≤ 10.9

Table 2: Comparison of the percentage error on the reaction rate with respect to exact quantum mechanical results of the presented new method and other existing approaches for the 2D LSTH potential. QTST stands for Quantum Transition State Theory,[11] while RPMD stands for Ring Polymer Molecular Dynamics.[9]

Finally, during the third year, I have spent three months visiting Prof. Gunnar Nyman's group at Göteborg University. The aim of the visit was to learn the Feynman-Kleinert theory (FK) which is used to conveniently approximate the Boltzmann operator.[12] This new knowledge will allow me to include theoretical spectroscopy among my future research interests. In fact, the approximate Boltzmann operator can be used to sample the initial conditions needed by semi-classical simulations of vibrational spectra including environmental and temperature effects. This scheme is more appealing than a rigorous Path Integral (PI) formulation to generate initial conditions. In fact, the full PI approach becomes computationally unmanageable when the dimension of the system increases. The main advantages of the FK approach are that it is computationally cheap and it has been successfully applied to condensed phase systems.[13] During my stay in Sweden, I have built a code to permit the adoption of the FK method in presence of a generic potential energy surface (**Project 4**). The first task I addressed was to write a code that

implements the FK approximation in one dimension, and I have tested it with model potentials, the double well and the Morse potential. For both of them the FK equations can be derived analytically, thus I compared the analytical result with another version of the code, in which integration and derivation are carried out numerically. Then, Prof. Nyman and his collaborator Dr. Poulsen have provided me with the code they used for liquid water simulations.[14] My task was to generalize this multidimensional implementation to the case in which the potential is not parametrized as a force field but it is known as a fitted potential energy surface from ab-initio data. The test case was the water molecule potential. So far, I have successfully tested my implementation against the harmonic and Morse potentials (Figure 7).

The main outcome of project 4 is a general implementation of the FK multidimensional scheme. This is a preliminary step for computing molecular semiclassical spectra without neglecting the role of temperature. In fact, the program I have written can be plugged in into our in-house semi-classical code to get the spectrum of water, including temperature effects due to the coupling with the environment. A paper in which spectra are obtained with this technique is in preparation.[15] From a more general point of view, pursuing this project while visiting the Nyman group has been highly formative. It gave me the possibility to perform my research in an international context. Furthermore, I had the opportunity to give an invited talk for the physical chemistry groups working at the department (Title: A quantum method for thermal rate constant calculations from stationary phase approximation of the thermal flux-flux correlation function integral), and I could join the conference "Swedish Theoretical Chemistry 2017 – Bridging gaps" held in Göteborg, (Sweden) on the 16th-18th August 2017, where I presented a poster communication.

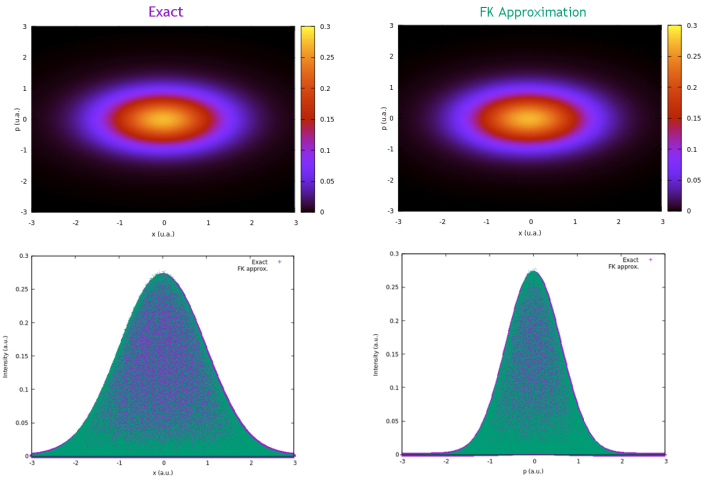

Figura 7: The accuracy of the numerical multidimensional code I have developed is tested against the harmonic potential. The Exact is the analytical Wigner transform of the Boltzmann operator. The FK numerical code gives very accurate results, this proves that the implementation is reliable and can be safely applied to more general cases for which the analytical result is unknown.

References

1 - W.H. Miller *J. Chem. Phys.* **62**, 1899 (1975); R. Hernandez, and W.H. Miller *Chem. Phys. Lett.* **214**, 129 (1993);
2 - J. R. Barker, T. L. Nguyen, J. F. Stanton, **C. Aieta**, M. Ceotto, F. Gabas, T. J. D. Kumar, C. G. L. Li, L. L. Lohr, A. Maranzana, N. F. Ortiz, J. M. Preses, J. M. Simmie, J. A. Sonk, and P. J. Stimac; MultiWell-2017 Software Suite; J. R. Barker, University of Michigan, Ann Arbor, Michigan, USA, 2017; http://clasp-research.engin.umich.edu/multiwell/; John R. Barker, *Int. J. Chem. Kinetics* **33**, 232 (2001); J. R. Barker, *Int. J. Chem. Kinetics* **41**, 748 (2009).
3 - F. Wang, D. P. Landau *Phys. Rev. Lett.* **86**, 2050, (2001); F. Wang, D. P. Landau *Phys. Rev. E: Stat. Phys., Plasmas, Fluids, Relat. Interdiscip. Top.* **64**, 056101, (2001).
4 - **C. Aieta**, F. Gabas, and M. Ceotto *J. Phys. Chem. A* **120**, 4853, (2016).
5 – **C. Aieta**, F. Gabas, and M. Ceotto *in preparation.*
6 – G. Brunton, D. Griller, L. R. C. Barclay, and K. U. Ingold *JACS*, **98**, 6803 (1976).
7 - W.H. Miller, Y. Zhao, M. Ceotto, and S. Yang *J. Chem. Phys.* **119**, 1329 (2003); M. Ceotto, S. Yang, and W.H. Miller *J. Chem. Phys.* **122**, 044109 (2005).
8 - W.H. Miller, S.D. Schwartz, and J.W. Tromp *J. Chem. Phys.* **79**, 4889 (1983); W.H. Miller *J. Phys. Chem. A* **102**, 793 (1998).
9 - I. R. Craig, and D. E. Manolopoulus *J. Chem. Phys.* **122**, 084106 (2005).
10 - **C. Aieta**, and M. Ceotto *J. Chem. Phys.* **146**, (2017).
11 - J. Liao, and E. Pollak *J. Phys. Chem. A* **104**, 1801 (2000).
12 – R. P. Feynman, H. Kleinert *Phys. Rev. A* **34**, 5080 (1986).
13 - J. A. Poulsen, G. Nyman, and P. J. Rossky *J. Chem. Phys.* **119**, 12179 (2003).
14 – J. A. Poulsen, G. Nyman, and P. J. Rossky *J. Chem. Theory Comput.* **2**, 1482 (2006).
15 - H. Li, **C. Aieta,** and M. Ceotto, *in preparation.*

Publications

- **C. Aieta**, and M. Ceotto "A Quantum Method for Thermal Rate Constant Calculations from Stationary Phase Approximation of the Thermal Flux-flux Correlation Function Integral", *J. Chem. Phys.* **146**, (2017).
- **C. Aieta**, F. Gabas, and M. Ceotto "An Efficient Computational Approach for the Calculation of the Vibrational Density of States", *J. Phys. Chem. A* **120**, 4853, (2016).
- F. Spadavecchia, M. Ceotto, L. Lo Presti, **C. Aieta**, I. Biraghi, D. Meroni, S. Ardizzone and G.Cappelletti "Second Generation Nitrogen doping of Titania Nanoparticles: a comprehensiveelectronic and microstructural picture", *Chinese J. of Chem.* **32**, 1195 (2014)
- C. Marchiori, G. Di Liberto, G. Soliveri, L. Loconte, L. Lo Presti, D. Meroni, M. Cappelli, G. Cappelletti, **C. Aieta**, and S. Ardizzone "Unraveling the Cooperative Mechanism of Visible-light Absorption in Bulk N,Nb Codoped TiO_2 Powders of Nanomaterials", *J. Phys. Chem. C* **118**, 24152, (2014).

Code Development

- J.R. Barker, T.L. Nguyen, J.F. Stanton, **C. Aieta**, M. Ceotto, F. Gabas, T.J.D. Kumar, C.G.L. Li, L.L. Lohr, A. Maranzana, N.F. Ortiz, J.M. Preses, J.M. Simmie, J.A. Sonk, and P.J. Stimac; MultiWell-2017 Software Suite; J.R. Barker, University of Michigan, Ann Arbor, Michigan, USA, **2017**; http://clasp-research.engin.umich.edu/multiwell/.

Communications (poster and oral)

- **Oral** communication: "A Quantum Approximate Method for the Calculation of Thermal Reaction Rate Constants" at the workshop "Different Routes to Quantum Molecular Dynamics", CECAM-HQ-EPFL, Lausanne, Switzerland, 6th-10th June 2016.
- **Poster** communication: "A Quantum Approximate Method for the Calculation of Thermal Reaction Rate Constants (Part I)" at the school "Path Integral Quantum Mechanics: Theory, Simulation and Application", CECAM-HQ-EPFL, Lausanne, Switzerland, 13th-17th June 2016.
- **Poster** communication: "A Quantum Approximate Method for the Calculation of Thermal Reaction Rate Constants (Part II)" and selected for a "**lightening presentation**" at the Faraday Discussion "Reaction Rate Theory: Faraday Discussion", Cambridge, United Kingdom, 19th-21st September 2016.
- **Poster** communication: "A Quantum Approximate Method for the Calculation of Thermal Reaction Rate Constants (Part II)" at the workshop "MolSimEng", Milano, Italy, 30th September 2016.
- **Poster** communication: "A Quantum Method for Thermal Rate Constant Calculations from Stationary Phase Approximation of the Thermal Flux-flux Correlation Function Integral" at the conference "Swedish Theoretical Chemistry 2017 – Bridging gaps", Göteborg, Sweden 16th-18th August 2017.

Contributions to Communications presented by others

- Oral Communication: "An Efficient Computational Approach for the Calculation of the Vibrational Density of States" F. Gabas, **C. Aieta** and M. Ceotto at the workshop "Different Routes to Quantum Molecular Dynamics" CECAM-HQ-EPFL, Lausanne, Switzerland, June 2016.
- Oral communication: "Quantum and Semiclassical Methods for Molecular Rate Constants and Vibrational Spectra Calculations" M. Ceotto, **C. Aieta**, F. Gabas, G.D. Liberto, R. Conte, at the "IXIV International Workshop on Quantum Reactive Scattering", Trieste, Italy, June 2017.
- Oral communication: "Semiclassical "Divide-and-Conquer" Method for Spectroscopic Calculations of High Dimensional Molecular Systems" M. Ceotto, R. Conte, G.D. Liberto, F.Gabas, M. Buchholz, **C. Aieta** "D.E. Shaw Research", New York, USA, July 2017.

List of attended courses

First year

- "A voyage into the world of Heterogeneous Photocatalysis", Prof. N. Serpone (1 CFU).
- "Aerosol particulate matter (PM): from the analytical characterization to the protection of environment and cultural heritage (Part I)", Prof. P. Fermo (2 CFU).
- "Aerosol particulate matter (PM): from the analytical characterization to the protection of environment and cultural heritage (Part II)", Prof. I. Salma (1 CFU).
- Spring Litearutre Seminar. Presented Paper: J.P. Layfield, and S. Hammes-Shiffer *Chem. Rev.* **114**, 3466 (2014). (2 CFU).
- "Transmission Electron Microscopy, EDX, EELS", Prof. D. Wang.
- "Simulazione di spettri di assorbimento ottico di molecole organiche mediante il codice QE-TDDFT" (SmartMatLab workshop), Dr. D. Ceresoli.
- "Simulazione di spettri NMR e EPR mediante il codice QE-GIPAW" (SmartMatLab workshop), Dr. D. Ceresoli.

Second year

- "Monitoring and treatment methodologies for drinking waters", visiting professor Prof. C. Brett, Università di Coimbra, Portugal (1 CFU).
- "Food Physical Chemistry", Prof. A. Schiraldi. (2 CFU).
- "Writing to communicate science: a practical workshop for students of chemistry area", lecturer S. Clark. (3 CFU).
- Martin Karplus Nobel lecture, Università Degli Studi di Milano, 8th April 2016. (0.5 CFU).
- Winter Literature Seminar. Presented Paper: I. Szabó, G. Czakó, *Nature Communications,* **6**, 5972 (2015) (CFU 2).
- Spring Literature Seminar. Presented Paper: J.O. Richardson, C. Pérez, S. Lobsiger, A.A. Reid, B. Temelso, G.C. Shields, Z. Kisiel, D.J. Wales, B.H. Pate, S.C. Althorpe, *Science*, **351**, 6279, 310 (2016) (CFU 2).

Third year

- "Corso SODALITAS – Giovani e impresa" (4 CFU).
- "Literature search in chemistry for Physical Chemistry", Prof. R. Martinazzo. (2+2=4 CFU).

Attended Schools, Congresses and Seminars

- "SMART Winter School (Space-time Multiscale Approaches for Research and Technology)", CECAM-IT-SNS, Pisa, Italia, 25th-29th January 2016.
- Workshop "Different Routes to Quantum Molecular Dynamics", CECAM-HQ-EPFL, Lausanne, Switzerland, 6th-10th June 2016.
- School "Path Integral Quantum Mechanics: Theory, Simulation and Application", CECAM-HQ-EPFL, Lausanne, Switzerland, 13th-17th June 2016.
- Faraday Discussion "Reaction Rate Theory: Faraday Discussion", Cambridge, United Kingdom, 19th-21st September 2016.
- Workshop "MolSimEng", Milano, Italy, 30th September 2016.
- Conference "Swedish Theoretical Chemistry 2017 – Bridging gaps", Göteborg, Sweden, 16th-18th August 2017.

Assistance, tutoring

- 2015, 20 hours of teaching at Dipartimento di Chimica, Università degli Studi di Milano, for the course Chimica Fisica I (Prof. S. Ardizzone). The teaching activity was devoted to thermodynamics exercises and data analysis.
- 2015, supervision of a bachelor student (G. Bruno "Effetto dell'anarmonicità della superficie di potenziale in processi di tunneling (Effect of the Potential Surface Anharmonicity on Tunneling Processes.)").
- 2017, co-supervision of a bachelor student (S. Americo "Computation of harmonic spectra of VOC to be compared with FTIR experiments").

Diffusion and promotion of chemistry and industrial chemistry activities within non-academic communities ("Orientamento" activity)

- Elaboration of new questions for the PLS chemistry test addressed to high school students, 2015.
- Redaction of a flyer addressed to high school students titled "Introduzione alla lezione del premio Nobel Martin Karplus", which introduces Martin Karplus and his scientific activity, as a background for attending his Nobel lecture held on 8th April 2016.
- Publication of an article for the broad audience: C. Aieta, G. Di Liberto, F. Gabas, R. Conte, and M. Ceotto "Viaggio a Bordo di un Nanomotore Guidato da Martin Karplus", Nuova Energia **2**, 88, 2016.
- Coordination and supervision of the building of the PLS chemistry test database addressed to high school students, 2016-2017.